

https://dspace.org/

Quantum transport through impurity clusters in carbon nano-materials

McIntosh, Ross William

2014-02-07
http://hdl.handle.net10539/13692

Downloaded from a DSpace repository. https://dspace.org/

Quantum Transport Through Impurity Clusters in Carbon Nano-materials

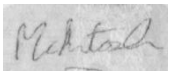
Ross McIntosh

A Dissertation submitted to the Faculty of Science, for the degree of Master of Science University of the Witwatersrand, Johannesburg, in fulfilment of the requirements for the degree of Master of Science

June 2013

DECLARATION

I declare that this thesis is my own, unaided work. It is being submitted for the Degree of Master of Science at the University of the Witwatersrand, Johannesburg. It has not been submitted before for any degree or examination at any other University.



(Signature of candidate)

12th day of June 2013

Abstract

Modified graphene and low dimensional carbon nano-electronic devices have the potential to supersede current technologies in many respects although manufacturing and understanding these materials poses a significant challenge which requires an incremental approach. Doping of graphene, a prerequisite for modifying the electronic properties, is still poorly understood. Band-modulation is therefore difficult to control. Resonant tunneling induced through the incorporation of impurity clusters has not yet been addressed. On the other hand electron-spin correlations in modified graphenes have hardly been studied. In this work we address these issues through a tandem approach of theoretical and experimental studies. This work begins with an *ab-initio* study of the electronic properties of bilayer graphene and the modifications induced through the substitutional incorporation of isolated nitrogen impurities. Nitrogen modification results in a change from a zero-gap semiconductor to a metal as a result of nitrogen incorporation while charge density calculations show the localization of charge in the vicinity of the impurity. This work on isolated impurities was then extended to impurity clusters.

The quantum transport properties of impurity clusters distributed within a high bandgap material were then studied. Different geometrical configurations of the impurity clusters were studied to tune quantum interference to control the carrier lifetime. The effects of randomly distributed clusters were also studied to interpret the effects of disorder. These studies provide insight into the transport properties of naturally grown quantum dot systems such as reduced graphene oxide which consists of low defect density graphene nano-islands randomly distributed in oxygen and free radical functionalized graphene which was studied experimentally. Resistance was recorded as a function of temperature for graphene oxide and reduced graphene oxide two terminal devices. Evidence of mesoscopic resistance fluctuations, charge carrier activation and enhanced elastic scattering was found while the magnetic properties of reduced graphene oxide showed a phase transition from ferromagnetism at low temperatures

to diamagnetism at higher temperatures.

Finally, the Kondo effect was demonstrated in reduced graphene oxide through transport and magnetoresistance measurements which were interpreted within the Fermi liquid description of the Kondo effect. These effects were explained through the microstructure of reduced graphene oxide and illustrate the significance of spin in reduced graphene oxide. These studies will inform the design of functionalized graphene spin-polarized devices and spin valves.

Acknowledgments

First and foremost I thank my principal supervisor Prof. Somnath Bhattacharyya for constant support, guidance, motivation and for answering endless questions. I also thank my co-supervisor Prof. Alexander Quandt for many discussions relating to density functional theory and graphene.

I thank the members of the Nano-scale Transport Physics Laboratory, past and present. My thanks to Dr. Zivayi Chiguvare, a man of great patience, and Dr. Kunjal Shah who helped on the experimental side. Many thanks also to Dr. Dmitry Churochkin who helped in many respects on theoretical aspects. I also thank Dr. Mikhail Katkov for discussions on tight-binding studies. I thank Dr. Messai Mamo for providing graphene oxide and reduced graphene oxide samples. I thank George Chimowa for help with the Cryogenic Free Measurement system and for many discussions. Thanks also to Christopher Coleman, Faris Mohammed and Siphephile Ncube for experimental assistance and discussions along the way. Many thanks to Charles Sandrock for constant experimental support. Many thanks also to Dr. Robert Warmbier for help with *ab-initio* calculations and computational aspects. Thanks also to George Manyali for useful discussions.

I thank the Material Physics Research Institute of the School of Physics, in particular Dr. Daniel Wamwangi for experimental support and guidance, and Dr. Rudolph Erasmus for support through a range of crises. I also thank the workshop team, in particular John Augustine. I also thank Dr. Brice Jamieson and Prof. Saibal Roy for measuring the magnetic properties of graphene oxide and reduced graphene oxide.

I thank the DST/NRF Centre of Excellence in Strong Materials (and in particular Prof. Ted Lowther and Dr. Shane Durbach) for financial support and the National Research Foundation (SA) for granting the Nanotechnology Flagship Programme to perform this work and the University of the Witwatersrand Research Council for financial support towards

research equipment.

I thank my parents and my sister for putting up with my insanity, the madness continues for another three years ...!

Contents

1 Introduction **1**
1.1 Outline 21

2 Electronic properties of Nitrogen Incorporated Bilayer Graphene **23**
2.1 Introduction 24
2.1.1 Introduction to Density Functional Theory 24
2.1.2 Electronic Properties of Bilayer Graphene 36
2.2 Model and Computational Details 40
2.3 Results and Discussion 42
2.4 Conclusion 59

3 Tuning Resonant Transmission Through Geometrical Configurations of Impurity Clusters **61**
3.1 Introduction 62
3.2 Model 64
3.3 Results and Discussion 69
3.4 Conclusion 79

4 Experimental Procedures **82**
4.1 Sample Preparation 82
4.2 Transport Measurements 83

5 Electronic and Magnetic Properties of Reduced Graphene Oxide **87**
5.1 Introduction 88
5.1.1 Mesoscopic Resistance Fluctuations and Carrier Scattering in Graphene 88
5.1.2 Electronic Transport in Reduced Graphene Oxide 90

5.1.3 Magnetic Properties of Reduced Graphene Oxide 91
5.2 Experimental Procedures 92
5.3 Results and Discussion 93
5.4 Conclusion 100

6 The Kondo Effect in Reduced Graphene Oxide 102
6.1 Introduction 103
6.1.1 The Kondo Effect 103
6.1.2 Kondo Correlations in Graphene 111
6.2 Experimental Techniques 115
6.3 Results and Discussion 116
6.4 Conclusion 121

7 Conclusions 123

References 129

List of Figures

1.1 a) A 3D tight-binding band structure plot of graphene. b) The band structure in the region of the K points. Image from [15]. 6

1.2 a) Landau levels represented on the Dirac cone of graphene under an external field. b) Schematic density of states under an applied field. Image from [16]. 6

1.3 a) The band structure of graphene determined through angle-resolved photoemission spectroscopy. b) Constant energy map of at the binding energy of the Dirac point, illustration the Brillouin zone of graphene. Image from [28]. 7

1.4 a) 3D plot of the tight-binding band structure of bilayer graphene in the AB configuration. b) Band structure with misaligned layers. Image from [26]. . . 9

1.5 a) Band structure of bilayer graphene determined through angle-resolved photoemission spectroscopy. b) Band structure close to the K point. c) Comparison of the band structure for monolayer and bilayer graphene close to the K point. Image from [26]. 10

1.6 3D image of the atomic structure of graphene with a vacancy. Image from [53]. In this study the rearrangement of carbon atoms at the edge of the vacancy was imaged in real time with an atomic resolution transmission electron microscope. 16

1.7 Atomic resolution transmission electron microscope image of reduced graphene oxide. The scale bar represents 1 nm. Dark grey regions represent residual functionalized regions and red regions represent individual adatoms. Blue regions represent regions dominated by topographical defects while green regions represent individual topographical defects. Vacancies are shaded yellow. Figure from [63]. 18

2.1 AB configuration for nitrogen incorporated graphene from (a)viewpoint perpendicular to the basal (b) rotated view. Carbon atoms maroon while nitrogen atoms are white. 41
2.2 AA configuration for nitrogen incorporated graphene from (a) viewpoint perpendicular to the basal graphene plane and (b) a rotated view. 42
2.3 Band structure of pristine bilayer graphene in the AB stacking configuration. 44
2.4 Band structure of pristine bilayer graphene in the AA stacking configuration. 45
2.5 Band structure of nitrogen incorporated bilayer graphene in the AB stacking configuration. 48
2.6 Band structure of nitrogen incorporated bilayer graphene in the AA stacking configuration. 50
2.7 Comparison of the band structure of pristine (black) and nitrogen incorporated (red) bilayer graphene in the AB stacking configuration. 51
2.8 Comparison of the band structure of pristine (black) and nitrogen incorporated (red) bilayer graphene in the AA stacking configuration. 52
2.9 Density of states for pristine bilayer graphene (black) and nitrogen incorporated bilayer graphene (red) in the AB stacking configuration. 52
2.10 Density of states for pristine bilayer graphene (black) and nitrogen incorporated bilayer graphene (red) in the AB stacking configuration the nitrogen incorporated DOS shifted. 53
2.11 Density of states of AA stacked bilayer graphene (black) and nitrogen incorporated bilayer graphene (red). 54
2.12 Comparison of density of states of AA stacked bilayer graphene (black) and nitrogen incorporated bilayer graphene (red) with the nitrogen incorporated shifted. 55
2.13 Comparison of the density of states of nitrogen incorporated bilayer graphene in the AA (black) and AB (red) stacking. 55
2.14 Charge density of pristine bilayer graphene in the AB configuration (a) view from above (b) viewed at an angle. 56
2.15 Charge density of nitrogen incorporated bilayer graphene in the AB configuration (a) view from above (b) viewed at an angle. 58
2.16 (a) Charge density of nitrogen incorporated bilayer graphene in the AA configuration. (b) Viewed at an angle 59

3.1 Schematic 3D diagram of the impurity cluster system including the leads and the 2D Gaussian potential. The regions in red indicate the high bandgap matrix while the multicoloured regions indicate the impurity cluster potential. 64
3.2 FWHM for the horizontal configuration with changing inter-cluster separation as a function of the scaling factor d/R defined as the ratio of inter-cluster separation to cluster size. Inset are the corresponding DOS spectra, for inter-cluster separations ranging from 2.5 to 4 nm, as a function of $\epsilon = E_F - E$ (for all figures). 70
3.3 FWHM for the horizontal configuration with changing inter-cluster size, from 2.5 to 4 nm, as a function of the scaling factor d/R. Inset are the corresponding DOS spectra as a function of ϵ. 71
3.4 $I - V$ curves for the horizontal configuration with changing inter-cluster separation, from 2.5 to 4 nm. Inset: the corresponding conductance spectra as a function of ϵ. 72
3.5 Peak to valley ratio of the resonant tunnelling feature as a function of the FWHM of the left (narrow) DOS peak. Inset: The corresponding curve as a function of the right (broad) DOS peak FWHM. 73
3.6 Conductance spectra as the horizontal configuration is rotated to the vertical configuration, each curve corresponds to a different angle measured from the horizontal. Inset is the FWHM of the corresponding DOS spectra as a function of the rotation angle from the horizontal. 74
3.7 DOS spectra in the vertical configuration with changing inter-cluster separation, from 2.5 to 4 nm, as a function of ϵ. Inset are the corresponding conductance spectra as a function of ϵ. 75
3.8 $I-V$ curves for the vertical configuration with increasing vertical inter-cluster separation, from 2.5 to 4 nm. The FWHM of the corresponding DOS spectra as a function of the scaling factor d/R is inset. 76
3.9 Conductance spectra as the central cluster is shifted vertically from the horizontal where each curve corresponds to a different vertical separation of the central cluster measured from the horizontal plane of the outer clusters, ranging from 0 to 2 nm. Inset is the FWHM of the DOS peaks as a function of the angle between the outer clusters and the central cluster. 77

3.10 DOS spectra in the triangular configuration (equilateral) with increasing uniform inter-cluster separation from 2.5 nm to 4 nm. The corresponding conductance spectra are inset. 78
3.11 I-V curves for the triangular configuration (equilateral) with increasing inter-cluster separation, from 2.5 to 4 nm. The FWHM of the corresponding DOS spectra as a function of the scaling factor d/R is inset. 79

4.1 Janis micromanipulated probe station. Upper left inset: Viewed from above. Upper right inset: Agilent B1500A Semiconductor Device Analyser. 84
4.2 Cryogenic free measurement system. 86

5.1 $I - V$ measurements for GO. Inset: Current as a function of temperature for GO and RGO. 94
5.2 Logarithmic conductance of GO as a function of $T^{-1/3}$. Inset: the corresponding plot for RGO. 95
5.3 Resistance as a function of temperature in RGO. The dashed lines are fits to the data with the suggested model e.g. for $b > 0$, $b = 0$ and $b < 0$. Upper inset: Low temperature $I - V$ measurements of RGO. 96
5.4 Magnetization as a function of temperature for GO and RGO. Inset is the magnetization of GO and RGO as a function of applied field at 10 K. 98
5.5 Hysteresis curves of GO at 300 K and 2 K indicating diamagnetism and ferromagnetism respectively. 99
5.6 Hysteresis curves of RGO at 300 K and 8 K indicating diamagnetism and ferromagnetism respectively. 100

6.1 Schematic diagram of the Anderson single impurity model. 106
6.2 Schematic diagram of a conserved tunneling process within the Anderson impurity model. 107
6.3 Resistance versus temperature of RGO. The solid red line is a fit to a quadratic temperature dependence while the green solid line is a fit to a logarithmic temperature dependence. Inset is the low temperature resistance plotted as a function of the temperature squared. 117
6.4 Magneto-resistance of RGO. Inset is the MR scaled with the characteristic temperature. 118
6.5 Hall Coefficient as a function of temperature 119

6.6 Carrier density as a function of temperature 120
6.7 Schematic diagram of local moment formation in RGO. Local moments (red arrows) form at residual free radicals (blue spheres) which are attached to the basal graphene plane and vacancies in the lattice. Extended states may form in unfunctionalized graphene regions. 121

Chapter 1

Introduction

The promise of innovative quantum nano-electronic devices heralding progress beyond the silicon era has spurned the study of low-dimensional carbon nano-materials which in many respects have the capacity for unsurpassable device performance. One of the primary focus areas is the development of ever faster-switching, lower power consumption and smaller devices such as field effect transistors. Of increasing importance are new forms of sensors for medical, environmental and bolometric applications. In parallel, quantum transport devices are actively being pursued. Quantum phenomena, widely accessible with the advent of nanotechnology, afford innovative device applications.

Naturally grown crystals, their growth reliant upon thermal energy and their structure exposed to external influences, as a rule occur as bulk materials. 2D crystals were thought to be too unstable to exist as free standing materials on the basis of thermal fluctuations [1]. With the advent of carbon nanotechnology, 1D and 2D materials can be synthesized and their unique properties studied [2] within a new paradigm in which fundamental physics is concurrent with new device applications. Amid extensive theoretical studies of new phenomena, hitherto inaccessible experimental studies of the fundamental behavior of low-dimensional materials are ongoing. With the relentless advance of nano-scale technologies, ever greater control and freedom to manipulate nano-materials is gained with a view to exploiting their fundamental properties. Regarding electronic transport properties, mesoscopic and quantum phenomena are widely accessible through nano-scale devices.

Graphene has shown promise for unrivalled electrical properties in many respects [2]. Graphene has generated widespread theoretical studies initially motivated by the "relativis-

tic" nature of charge carriers, described as massless Dirac Fermions [3, 2], bringing quantum electrodynamics to the forefront of condensed matter physics. Experimental discoveries drive theoretical studies while ongoing theoretical studies motivate experimental investigations. Graphene has opened the door for research into truly 2D materials but still dominates the field. Experimental condensed matter physics, until the advent of graphene, was reliant upon high quality synthesis methods which are often time-consuming, highly technical and costly. With the relatively simple isolation by mechanical exfoliation, researchers have gained widespread access to a new material without the need for complicated synthesis techniques.

The physics of graphene is of significant interest. Symmetries in real space are conserved in transformations to momentum space. The graphene lattice can be viewed as the superposition of two equivalent sub-lattices. This is reflected in the valley degeneracy within the hexagonal Brillouin zone. The majority of the early studies in graphene focused on the linear dispersion around the Dirac points. This description is valid in the very low energy region surrounding the K points, close to the Fermi energy (E_F). The linear dispersion of graphene is often illustrated using a tight-binding model. $Ab-initio$ calculations of the band structure also show a linear dispersion in the vicinity of the K and K' points, informing the choice of hopping parameters for tight-binding calculations. In turn, subject to algebraic manipulation and first-order approximations, the final form of the Hamiltonian yields insight to the physics of graphene. The physical significance of the linear dispersion is illustrated in the anomalous quantum Hall effect in monolayer and bilayer graphene.

The band structure of graphene is of significant interest and has been widely studied [4, 5, 6]. The general approach begins with the definition of a basis with two atoms in a rhombohedral unit cell. With a tight-binding Hamiltonian, nearest neighbour coupling is assumed. The wavefunction is described as a superposition of Bloch states. The graphene lattice is therefore effectively separated into two sub-lattices, A and B. The effective Hamiltonian is studied near the K points. The tight binding Bloch functions are defined by

$$\Phi_m(\mathbf{k}, \mathbf{r}) = N^{-1/2} \sum_{i=1}^{N} e^{i\mathbf{k}\cdot\mathbf{R}_{m,i}} \phi_m(\mathbf{r} - \mathbf{R}_{m,i}) \tag{1.1}$$

where N is the number of unit cells in the lattice, ϕ_m represents the atomic wavefunction, $(m = 0, 1, \ldots, n)$, $\mathbf{k}$ represents the wavevector and $\mathbf{R}$ represents the atomic position. The electronic wavefunction can then be defined as

$$\Psi_j(\mathbf{k},\mathbf{r}) = \sum_{m=1}^{n} c_{j,m}\Phi_m(\mathbf{k},\mathbf{r}) \tag{1.2}$$

where $c_{j,m}$ are expansion coefficients. The eigenenergies are defined by

$$E_j(\mathbf{k}) = \frac{\langle\Psi_j|\,\mathcal{H}\,|\Psi_j\rangle}{\langle\Psi_j|\Psi_j\rangle}\ . \tag{1.3}$$

Solving for the eigenenergies of Eq. 1.3 proceeds by reformulating the problem by minimizing the expansion coefficients $c_{j,m}$ and finally solving an equation of the form $det(\mathcal{H}_t - E_j S) = 0$. The transfer integral matrix $\mathcal{H}_t$ and overlap matrix S are given by

$$\mathcal{H}_t = \langle\Phi_m|\,\mathcal{H}\,|\Phi_{m'}\rangle \quad S = \langle\Phi_m|\Phi_{m'}\rangle\ . \tag{1.4}$$

Truncating the plane waves to contributions from the same unit cell, the transfer integral matrix elements can be written as

$$\mathcal{H}_{t,AA} \simeq N^{-1}\sum_{i=1}^{N}\langle\phi_A(\mathbf{r}-\mathbf{R}_{A,i})|\,\mathcal{H}\,|\phi_A(\mathbf{r}-\mathbf{R}_{A,i})\rangle$$

which can be considered as the summation over all unit cells of

$$\epsilon_{AA} = \langle\phi_A(\mathbf{r}-\mathbf{R}_{A,i})|\,\mathcal{H}\,|(\phi_A\mathbf{r}-\mathbf{R}_{A,i})\rangle\ .$$

For intrinsic graphene, $\epsilon_{AA} = \epsilon_{BB} = 0$.

Considering the off-diagonal elements, coupling between nearest neighbours must be accounted for through the introduction of the vector δ_l where the index l runs over the nearest neighbour vectors. The off diagonal elements can then be written as

$$\mathcal{H}_{t,AB} \simeq N^{-1}\sum_{i=1}^{N}\sum_{l=1}^{3}\langle\phi_A(\mathbf{r}-\mathbf{R}_{A,i})|\,\mathcal{H}\,|\phi_B(\mathbf{r}-\mathbf{R}_{A,i}-\delta_l)\rangle\ .$$

The transfer matrix can then be described as

$$\mathcal{H}_{t,AB} = \begin{pmatrix} \epsilon_0 & tf_0(k) \\ t_0 f^*(k) & \epsilon_0 \end{pmatrix} \tag{1.5}$$

where t is the transfer integral $t_0 = \langle \phi_A(\mathbf{r} - \mathbf{R}_{A,i}) | \mathcal{H} | \phi_B(\mathbf{r} - \mathbf{R}_{A,i} - \delta_l) \rangle$ and the function $f(k)$ defines the plane waves connecting a C atom to its nearest neighbours.

The region of interest is close to E_F where the π and π^* bands touch so $f(k)$ may be approximated in the region of the K (K') points. A first order Taylor series expansion yields $f(k) = k_x - ik_y$. This effectively yields a Dirac-like Hamiltonian in the vicinity of the K (K') points,

$$\mathcal{H}_t = \hbar v_F \begin{pmatrix} 0 & k_x - ik_y \\ k_x + ik_y & 0 \end{pmatrix} = \hbar v_F \sigma \cdot \mathbf{k} \tag{1.6}$$

where $v_F = 3at/2\hbar$ and σ is a 2D Pauli matrix. Close to the K and K' points the full band structure can be expanded and along with the approximation $|\mathbf{q}| \ll |\mathbf{K}|$, we find a linear dispersion relation,

$$E_{\pm}(\mathbf{q}) \approx \pm v_F |\mathbf{q}| + O[\frac{\mathbf{q}}{\mathbf{K}^2}] \ . \tag{1.7}$$

The dispersion relation, to first order is independent of mass. Many of the unusual properties of graphene stem from this dispersion relation which is illustrated in Figure 1.1 while in Figure 1.2 the Landau levels are represented on the Dirac cone.

The description of charge carriers as relativistic Weyl fermions stems from analysis of graphene within the tight-binding formalism [7]. Neglecting second nearest neighbour coupling, and taking the Fourier transform of the electronic operators and expanding around the K and K' points, it can be shown that close to the K point the wavefunction satisfies the Dirac equation

$$-v_F \sigma \cdot \boldsymbol{\nabla} \psi(\mathbf{r}) = E\psi(\mathbf{r}) \tag{1.8}$$

where v_F is the Fermi velocity (around $10^6\ m.s^{-1}$ in graphene), σ represents Pauli matrices which in this case do not act on spin but the sub-lattice degree of freedom (the so-called "pseudo-spin" of quasi-particles in graphene). It is in fact a consequence of the of the construction of the unit cell with two atoms together with the symmetry of the graphene

lattice which is the combination of two sub-lattices. It is on the indices of these sub-lattices that the Pauli matrices act. Considering momentum around the K point, the wavefunction in in k space is given by the two-component spinor

$$\psi_{\pm,\mathbf{K}}(\mathbf{k}) = \frac{1}{\sqrt{2}} \begin{pmatrix} e^{-i\theta_{\mathbf{k}}/2} \\ \pm e^{i\theta_{\mathbf{k}}/2} \end{pmatrix} \tag{1.9}$$

where $\theta_{\mathbf{k}} = \arctan(k_x/k_y)$. It is evident from (1.9) that the wavefunction undergoes a change of sign if the phase $\theta_{\mathbf{k}}$ changes by 2π. The Hamiltonian in (1.8) has two eigenvalues as $\sigma \cdot \mathbf{p} |\psi\rangle = \pm p |\psi\rangle$ where $\mathbf{p}$ is the momentum operator. Therefore, in an energy eigenstate, the pseudospin σ is either parallel or anti-parallel to the charge carrier momentum. This is the origin of the chirality of quantum states close to the Dirac points. The density of states (DOS) of pristine graphene is zero at E_F while two symmetric van Hove singularities are found at positive and negative energies [2]. In the vicinity of E_F the density of states is linearly proportional to the energy.

Although the propagation of charge carriers is not relativistic in the sense that the Fermi velocity is only a small fraction that of light, charge carriers (treated as quasi-particles) are most effectively described within the Dirac regime. With coherent transport over large distances, quantum effects are expected to play a prominent role in electronic transport in graphene. With its properties closely related to its high symmetry, many-body interactions are also expected to be prominent in graphene generating a new avenue for research of quantum many-body and quasi-particle interactions. Ultra-high frequency analogue transistors have already been developed and will likely supersede current GaAs devices [8].

Shubnikov de Haas oscillations were demonstrated in graphene immediately after its isolation sparking great interest [3]. At high fields, the quantum Hall effect was demonstrated [9, 10]. However, in graphene the quantum Hall effect was found to occur at fractional, instead of integer values for conductivity. This is related to the two sub-lattices which define graphene layers as well as the description of charge carriers as massless relativistic fermions. The two sub-lattices in conjunction with the Dirac framework results in two pseudo-spins which are not related to the intrinsic spin of charge carriers [11, 9]. The energy levels of massless relativistic fermions within a quantized magnetic field are given by $E_N = 2e\hbar c_*^2 B(N + 1/2 \pm 1/2)$ where c_* is the velocity of charge carriers (predicted to be 10^6 $m.s^{-1}$ in graphene) [9]. The lowest Landau level is therefore found when $N = 0$ for fermions

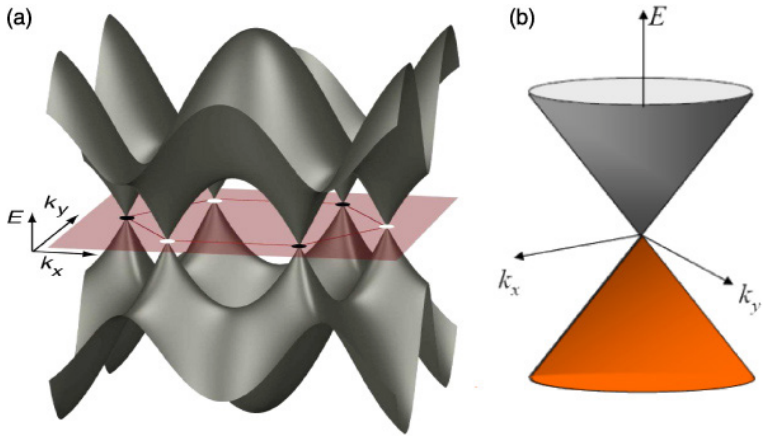


Figure 1.1: a) A 3D tight-binding band structure plot of graphene. b) The band structure in the region of the K points. Image from [15].

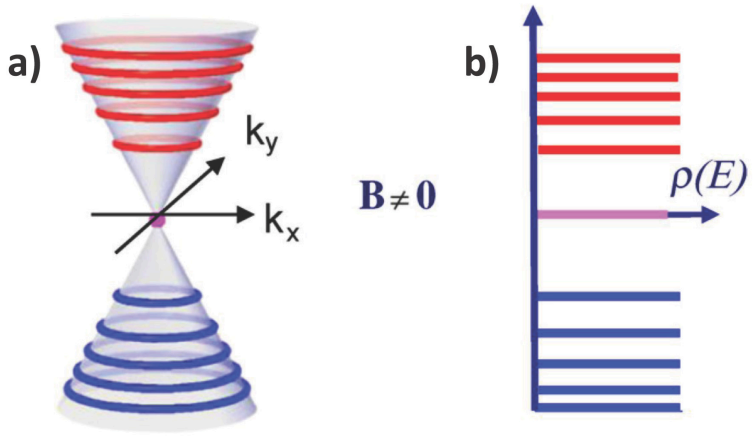


Figure 1.2: a) Landau levels represented on the Dirac cone of graphene under an external field. b) Schematic density of states under an applied field. Image from [16].

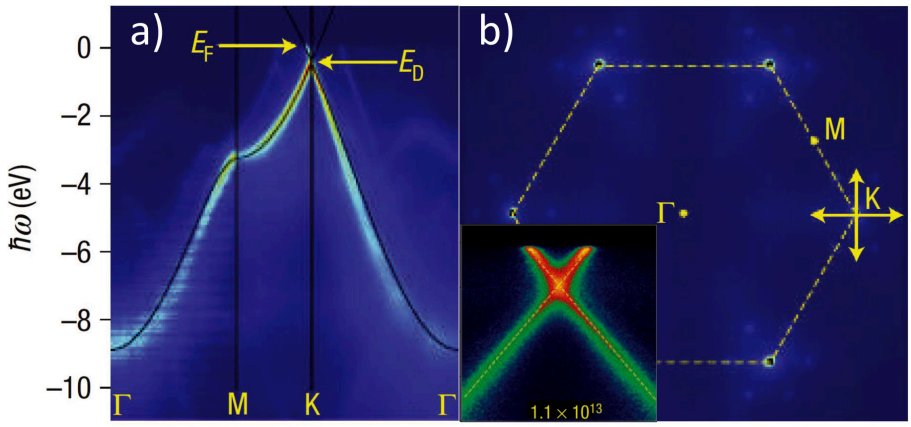


Figure 1.3: a) The band structure of graphene determined through angle-resolved photoemission spectroscopy. b) Constant energy map of at the binding energy of the Dirac point, illustration the Brillouin zone of graphene. Image from [28].

described with a minus sign. The first plateau in σ_{xy} therefore occurs at a half integer value and the subsequent quantized Hall plateaus are all offset by a fractional amount.

This serves as an illustration of the unusual features and rich physics associated with low-dimensional materials, graphene in particular. An additional unusual discovery was the quantum Hall effect at room temperature [12]. This was attributed to large cyclotron gaps, a consequence of the Dirac-like nature of charge carriers in graphene. The cyclotron gaps are much greater than the thermal energy, even at room temperature although the effect was only observed at high fields. Additional studies confirmed the presence of massless Dirac quasi-particles [13, 14]. Furthermore, it was found that only a 2D spatially quantized band was populated at high gate voltages [3]. This intrinsic property of graphene is manifest in a number of phenomena, for example the observation of the quantum Hall effect at room temperature and the relative insensitivity of carrier mobility to temperature. Graphene can therefore also tolerate high current densities.

High quality graphene exhibits ambipolar transport. As the gate voltage is swept from positive to negative, the resistance varies symmetrically about the charge neutrality point [6, 5] changing smoothly from electron to hole transport. This reflects the symmetry of the dispersion relation about the K points, as shown in Fig.1.1 from [15] (Landau levels on the Dirac cone are illustrated in Fig. 1.2 from [16]). In addition as charge carriers behave as massless fermions in graphene there is symmetry between electron conduction and hole conduction [17]. This is not the case in other materials as the effective mass of

electrons and holes is different and therefore each satisfies a different Schrödinger equation [17]. This ambipolar effect is relatively insensitive to temperature. In conventional 2D electron gasses, populating the conduction band drastically reduces carrier mobility. In graphene however high mobilities are maintained even at room temperature as it is a zero bandgap semiconductor (sometimes referred to as a zero-overlap semi-metal) and charge carriers exhibit ballistic transport over sub-micron distances. Therefore impurity scattering presents a severe limitation to mobility in graphene systems.

Additionally, being a single atomic layer thick, interactions between graphene and underlying substrates are significant offering additional scope for tuning the electronic properties. On the other hand, phonon interactions from the substrate can influence charge carriers in graphene with the result that the mobility falls short of its potential [18]. Suspended graphene, however, is free from these limitations. High mobilities, up to 200 000 $cm^2/(V.s)$, have been recorded in suspended graphene [18]. This will have significant implications towards the development of high-speed transistors. However, this was a demonstration on an ideal sample and the major challenge remains in the fabrication of large-scale low-disorder graphene. In contrast, other materials such as $GaAs$ hybrids have exhibited even higher mobility and are more amenable to large-scale production although the mobility decreases dramatically with temperature.

The nature of carrier propagation in graphene has led to widespread theoretical studies of Klein tunnelling. A manifestation of the Klein paradox has been illustrated in monolayer graphene, using a transfer matrix method, where the transmission coefficient was found to be unity, independent of the barrier height and width provided the wavefunction (wavevector) is normally incident upon the barrier [19]. The generally accepted resolution of the Klein paradox is that the electron barrier is an attractive potential for positrons. The virtually perfect transmission is attributed to resonance between the electronic and positronic wavefunctions [20]. Bilayer graphene in contrast has a parabolic dispersion relation about the K and K' points which is mass dependent. The transmission coefficient is sensitive to the well width which determines the energetic position and number of resonant states.

Conventional field effect transistors rely on a bandgap. As such, mono-layer graphene is limited due to its lack of an intrinsic band-gap. Graphene nano-ribbons display a bandgap however at present they are difficult to manufacture and manipulate. Alternatively, a bandgap can be generated in bilayer graphene and could provide a route to the fabrication of field effect transistors [4]. Control over the bandgap through an external field has

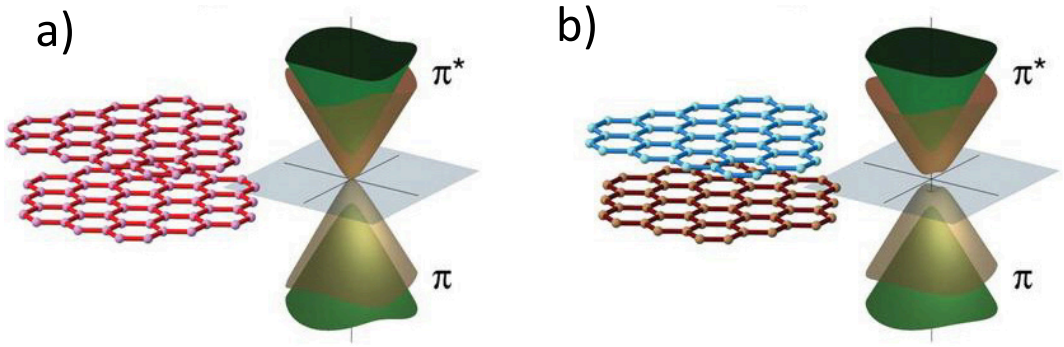


Figure 1.4: a) 3D plot of the tight-binding band structure of bilayer graphene in the AB configuration. b) Band structure with misaligned layers. Image from [26].

been demonstrated and it has been suggested that bilayer graphene is the only known material with a controllable energy gap [21, 22]. Additionally, the electronic properties of bilayer graphene are of significant interest. Furthermore, it has been suggested that bilayer graphene is less sensitive to external influences, making it more robust and therefore suitable for nano-electronic applications [23].

Insights into the physics of bilayer graphene can also be gained through analysis within a tight-binding framework following a similar treatment to monolayer graphene. The transfer integral matrix is constructed in a similar manner to the case for monolayer graphene with four atoms in the unit cell. It is assumed that there is some inter-layer coupling although the hopping term is weak in comparison to the intra-layer hopping terms. The inter-layer coupling is strongest between atoms directly above each other [24]. There is also an intra-layer hopping term between between atoms which are not directly above each other in addition to the inter-layer term. The Hamiltonian is therefore expressed as a 4×4 matrix and the corresponding spinor contains four elements instead of two [24] as is the case for monolayer graphene. This matrix can then be reduced to a 2×2 matrix. The Hamiltonian is again studied in the region of the K points. Hopping between the two furthest atoms in the unit cell is neglected. More details are given in Chapter 2 of this work.

Bilayer graphene also exhibits a form of the quantum Hall effect although it is not the same as the anomalous integer quantum Hall effect of monolayer graphene. In conventional 2D semiconductors, the Hall conductivity displays a distinct plateau where the carrier concentration is zero. This is not the case in monolayer graphene as discussed above. However in bilayer graphene, not only is the conventional plateau at zero absent but the difference in conductance between the first hole and electron plateaus is twice as large as the difference in

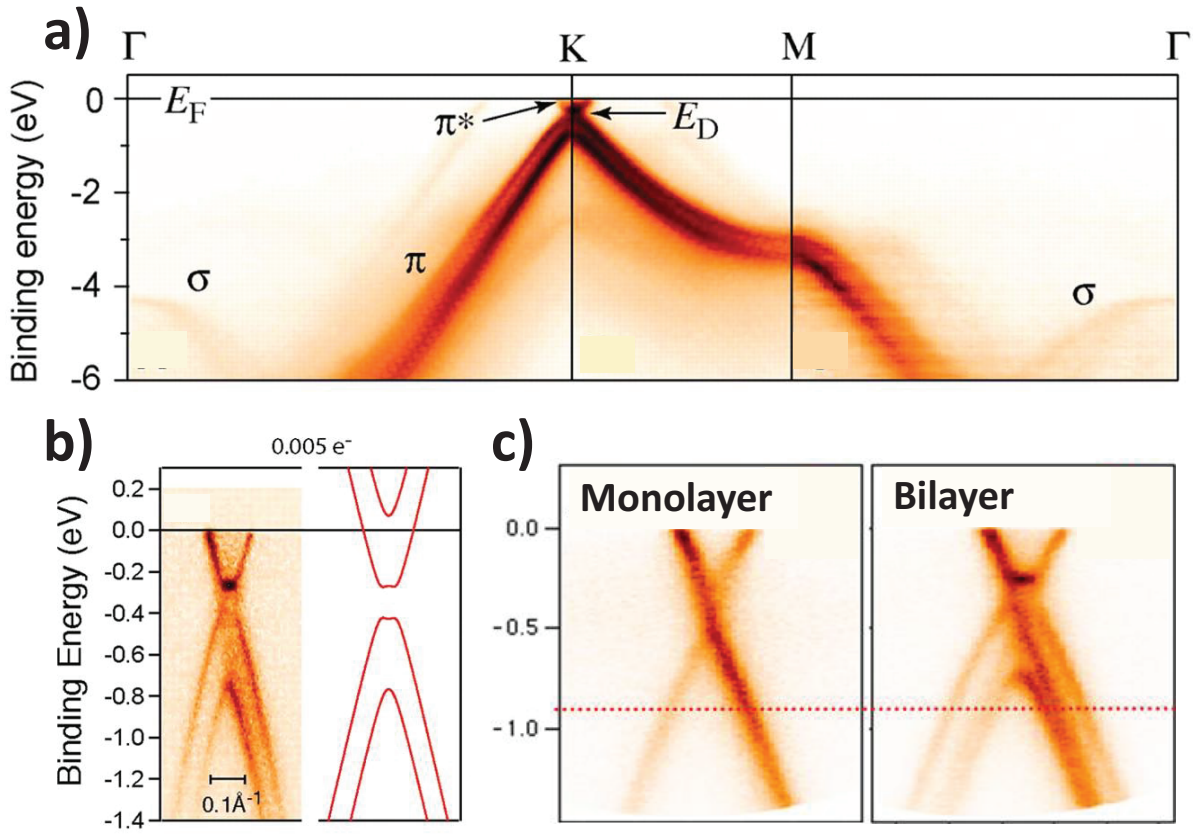


Figure 1.5: a) Band structure of bilayer graphene determined through angle-resolved photo-emission spectroscopy. b) Band structure close to the K point. c) Comparison of the band structure for monolayer and bilayer graphene close to the K point. Image from [26].

conductance between subsequent Hall plateaus [4]. This is related to the double degeneracy of the lowest Landau level. Through a tight-binding treatment, this can be related to the bandstructure of bilayer graphene in the vicinity of the K points.

A generalized Hamiltonian can be developed which can treat both single and multilayer graphene. Contours in momentum space are then related to phase shifts in charge carrier wavefunctions (Berry's phase). This Berry's phase is related to the eigenstates of Landau level functions [4] and as the Berry's phase is 2π the lowest Landau level has two eigenstates. With the additional spin and valley degeneracies, the lowest Landau level is eight-fold degenerate while subsequent Landau levels are four-fold degenerate. This could result in strongly correlated quantum Hall states based on the electron-electron interaction [25]. Another interesting observation which remains unexplained is that the longitudinal conductivity is non-zero even at low temperatures and high magnetic fields, showing no gap in the Landau spectrum.

The bandgap in bilayer graphene was investigated experimentally on the basis of theoretical studies which indicated that a bandgap may form in the absence of perfect symmetry between the two layers as shown in Figure 1.4 [25, 26]. Bilayer graphene on SiC was studied. The interactions of the bilayer and the substrate are crucial in bandgap formation as charge depletion in the substrate (and charge accumulation in the bottom graphene layer) induces asymmetry between the graphene bilayers. The band-structure was probed through angle resolved photo-emission spectroscopy (ARPES) and shows good agreement with tight-binding and $ab-initio$ calculations of the band structure (see Fig. 1.5.). Constant energy maps also showed high symmetry points as expected. In this study, the carrier density was varied through potassium doping and switching applications were suggested subject to the control of the relative potentials of the graphene layers. In a subsequent study, Dirac fermions were also found in graphite using ARPES along with quasi-particles with a parabolic dispersion relation [27]. A further study confirmed the linear dispersion in the region of the Dirac points in mono-layer graphene [28]. Quasi-particle interactions were investigated as the cause of small anomalies in the ARPES measurements. Electron-plasmon interactions were found to be significant while electron-phonon and unusual electron-plasmon and electron hole decay processes were also discussed [28].

The unusual carrier scattering in graphene is of significant interest. The impetus of many of the initial graphene studies was the physical phenomena surrounding the dispersion relation (such as the quantum Hall effect) however more general studies have now been

performed. Inextricably bound to such studies is the problem of understanding the nature of disorder in graphene systems. In this regard, graphene is an ideal test-bed due to its sensitivity to structural as well as topological disorder. From the perspective of electronic transport, disorder is often synonymous with weak localization however magneto-resistance studies in graphene have indicated an unexpected suppression of weak localization [29]. It was pointed out that the behaviour of the magneto-resistance of graphene is significantly different to that of metals in that most graphene devices showed no magneto-resistance while conventional metals would show prominent magneto-resistance under the same conditions. In addition, it was demonstrated that the magneto-resistance of monolayer graphene is very different to that of graphite [29]. However universal conductance fluctuations (UCF) were widely observed at high carrier concentrations.

The suppression of weak localization was attributed to topographical distortions of the graphene lattice which induce a local (random) gauge field that breaks time reversal symmetry, effectively preventing weak localization [29]. UCF's on the other hand were unaffected as the gauge field is randomly distributed. This study motivated additional studies of carrier scattering in graphene. The scaling of resistivity with temperature provides some information about the nature of carrier scattering and has thus been the focus of a number of studies in graphene [30, 31, 32, 33, 34, 35, 36, 37, 38]. There is another factor which contributes to the suppression of weak localization in graphene when considering long-range disorder. For example, scattering from charge puddles, widely studied in graphene, is such a form of long range order. The chirality of charge carriers, a consequence of employing the Dirac Hamiltonian, prevents direct backscattering [38]. This suppression of backscattering has even led to the experimental observation of weak anti-localization [35].

Based on the band structure of graphene, a recent study supported by experimental evidence has suggested that the "valley" quantum state can be read based on measuring mesoscopic conductance fluctuations (MCF's) [35]. This is a dramatic illustration of the symbiosis between the calculated band structure and mesoscopic conductance fluctuations and could even have applications in quantum information technology. Elastic scattering, both inter-valley and intra-valley, is expected to add a quantum contribution to the resistivity [5]. Changes in the carrier density influence the elastic scattering such that it can be tuned through the application of a gate voltage. In turn, changes in the elastic scattering can suppress MCF's.

The low density of states surrounding E_F suggests that little electron screening occurs in

graphene close to the charge neutrality point. Charged impurities therefore also act as long-range electron scatterers [38] . Doping is a prerequisite for tuning the electronic properties for practical implementation. The high mobility of doped graphene has stimulated studies into new high-mobility FET's. However, the nature of scattering in these systems remains unresolved [38]. Moreover, in the regime of nano-electronics, a thorough understanding of the principle scattering mechanisms is more important than in conventional electronics. In addition, the specific details of scattering will influence the performance of unconventional spin valves and spin polarized devices [39].

Studies have demonstrated that pristine graphene is a marginal Fermi liquid as the imaginary part of the self energy as a function of energy is linear [5]. In graphene, the DOS at E_F is zero so there is little electron screening of conduction states close to E_F. However the ratio of the Coulomb energy to the kinetic energy is independent of the carrier density, a feature which is uncommon in Fermi liquids [40]. Close to the charge neutrality point, the prevalence of long range interactions results in a renormalization of the the quasi-particle characteristics which is different to the Fermi liquid behavior for non-zero chemical potential where the finite DOS allows conventional screening. Slight deviations from the conventional Fermi liquid quasi-particle excitations have also been reported experimentally [28]. The decay of a photo-hole through excitation of an electron from below E_F showed that the expected quadratic energy dependence was modified, likely as a result of the linear dispersion close to E_F [28]. Doped graphene, on the other hand is a Fermi liquid as the imaginary part of the self energy (as a function of energy) depends on the product of the energy squared and the logarithm of the energy [41]. In practice, due to unintentional surface-induced doping and impurities it is likely that all graphene devices will be Fermi liquids.

Doping of graphene has been widely studied to tune the electronic properties [42, 43]. While the opening of a bandgap in graphene has been studied extensively additional band modulation is required to realize graphene based electronics including metallic forms of graphene. In addition, band modulation may likely pave the way for quantum transport devices. With the persistence of coherent quantum effects to high temperatures, graphene could play a role in developing superlattice structures for high frequency applications. Nitrogen doping in particular is of interest as it can form a number of different structures when incorporated into graphene. Nitrogen can form pyridinic or nitrilic bonds with carbon which result in vacancies and p-type doping [42, 44, 45]. Nitrogen can be stably substitutionally incorporated in graphene and bilayer graphene [46]. Substitutional N doping induces n-type

conductivity and preserves the hexagonal graphene lattice so the mobility of charge carriers remains high [43]. Angle resolved photo-emission spectroscopy has shown that indeed substitutional N doped graphene is metallic while a band gap opens up due to the loss of intrinsic symmetry [43].

The electronic transport properties of N doped graphene were studied by Wei *et al.* [47]. Transport measurements showed n-type doping while the mobility of N doped devices was 1.5 to 3 times less than the mobility of pure graphene samples. N has thus far been incorporated in graphene grown through chemical vapour deposition (CVD) however CVD graphene is highly disordered, limiting the mobility. Practical realization of high mobility N doped graphene is therefore subject to reductions in the disorder of CVD graphene or N incorporation in pristine graphene, such as mechanically exfoliated graphene, through new synthesis techniques. Nitrogen doping has also been widely studied in carbon nano-tubes where p-type or n-type conductivity has been observed depending on the N complexes which are incorporated during synthesis [47].

The combination of doping as well as controlling the number of layers has recently drawn attention due to the tunable nature of the bandgap in bilayer graphene and the modifications to the electronic properties which can be induced through N incorporation. In Chapter 2 of this work we have therefore studied the electronic properties of substitutional N incorporated bilayer graphene with electronic device applications in mind. While the band structure of pristine bilayer graphene shows a π and π^* band which meet at E_F at the K point, the band structure of N incorporated graphene is metallic with a gap at the K point. We have studied N incorporated bilayer graphene in both the AA and AB configurations. In contrast to pristine bilayer graphene which is sensitive to the orientation of the graphene layers, we find that there is little difference between the band structure of N incorporated bilayer graphene in the AA and AB configurations. Nitrogen localizes charge in the vicinity of the impurity, not only within the basal graphene plane but also perpendicular to the graphene layers. We find that there is little inter-layer coupling even if the nitrogen atoms are arranged one above the other. Nitrogen incorporation changes the nature of carrier scattering although the structure of the graphene lattice is virtually unchanged.

Nitrogen is one of the principle dopants employed in the modification of the electronic properties of carbon materials and nano-materials [48]. The performance of amorphous carbon films can be enhanced through N incorporation. While N incorporation increases the conductivity overall the non-linear increase of conductivity with $N\%$ and eventual saturation

(the conductivity may decrease after attaining a maximum) indicates that N incorporation is unlike conventional doping. Nitrogen can be substitutionally incorporated in both the sp^2 and sp^3 phases of carbon. In addition N complexes can be formed during synthesis which are incorporated into the material. This affords great flexibility in modifying the electronic properties but also complicates the problem of understanding N doping in carbon. One of the outcomes of the present study is a basic understanding of some of the features which are induced in graphitic clusters which are prevalent in amorphous carbon films as a result of N incorporation. Understanding the incorporation of N impurities in bilayer graphene serves as a precursor for future studies in consideration of the transport properties of N incorporated amorphous carbon films. This study will aid in understanding the fundamentals of the electronic properties of carbon modified through single N impurities as well as clusters.

Nitrogen doping has been widely studied towards modifying the electronic properties of nano-crystalline diamond films [49]. Here too N doping enhances the electrical conductivity however there is a non-linear increase in conductivity with the atomic incorporation of N [50]. Strangely, N doping can induce p-type or n-type conductivity [49]. It seems that the influence of N incorporation is strongest within the grain boundaries however a satisfactory explanation for these features has proven elusive. Nitrogen doping is know to modify disorder within the grain boundaries in addition to substitutional incorporation and the incorporation of N complexes [51].

As an extension to single impurities, the electronic properties of impurity clusters in graphene are also of significant interest [52]. The electronic properties of boron impurity clusters on graphene layers and nano-ribbons were studied [52] where wiring of the system would be provided by chains of boron impurities. In this study it was argued that while impurities tend to diffuse in graphene, clusters would not diffuse as easily, an issue already faced in MOSFET devices. In addition the rearrangement of carbon atoms at the edge of a vacancy in graphene has been imaged in real time (Figure 1.6 from [53]). Resonant tunnelling features in current-voltage measurements have been predicted in graphene systems where the impurity arrangement was controlled [54]. Nitrogen doping is also known to promote $sp^2 - C$ clusters in amorphous carbon and nano-crystalline diamond films effectively creating graphitic regions within predominantly $sp^3 - C$ regions. Quantum transport properties through related graphene quantum dots has recently been studied. Beyond interesting quantum phenomena, applications in quantum information technology have driven these studies.

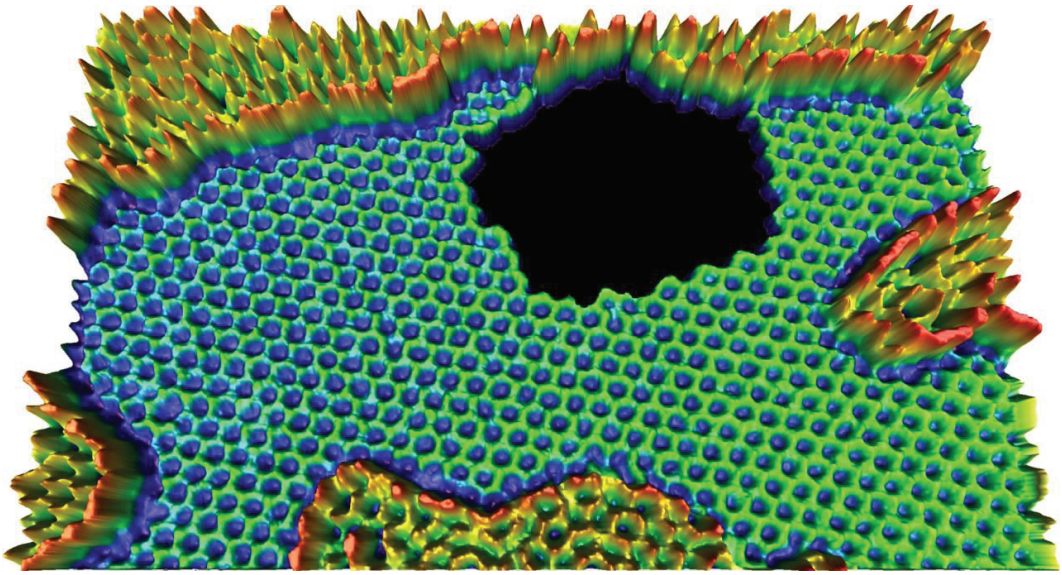


Figure 1.6: 3D image of the atomic structure of graphene with a vacancy. Image from [53]. In this study the rearrangement of carbon atoms at the edge of the vacancy was imaged in real time with an atomic resolution transmission electron microscope.

In the study by Hewageegana and Apalkov, electronic transport through circular graphene quantum dots within some high potential matrix was investigated [55]. In this study the Dirac Hamiltonian was applied to electrons in the graphene quantum dots and coupling through the continuum states was assumed while direct inter-dot coupling was neglected as the energy levels of the graphene quantum dots are degenerate with the leads. The confinement of states based on peaks in the scattering cross section as a result of the lead-dot coupling (in contrast to the confinement in conventional quantum dots) and the electron escape rate were discussed. The relationship between the energy of quasi-localized states and the ratio between the quantum-dot separation and the radius of the quantum dot was briefly discussed. In particular, resonances were described as eigenfunctions with the real part of the complex eigenvalue associated with the resonant energy while the inverse of the imaginary part is related to the lifetime of the decaying quasi-localized state [55]. This approach, although unconventional, is related to previous studies of quantum dot systems where the Dirac Hamiltonian has not been applied. However a realistic quantum-dot interface was lacking in this study. It was assumed that the quantum dot interface with the high potential matrix was perfectly sharp (i.e. the potential is described by a Heaviside function). In real systems, the potential will vary over the interface due to the band mismatch and lattice

mismatch.

Some fundamental studies [56] of quantum dot systems rely in principle on the framework developed by Shahbazyan and Raikh [57]. They developed a treatment of transport through a double impurity (double quantum dot) system which accounts for direct coupling between the dots as well as coupling between the dots and the continuum states of ideal leads. There is therefore indirect coupling between each quantum dot through the leads. They found the formation of two states with different lifetimes, a sub-radiant state and a super-radiant state. In subsequent studies, the formation of Fano resonances in conductance spectra was discussed in terms bonding and anti-bonding states [58, 59, 60, 61]. Using the Hubbard model the spin properties of quantum dot systems have also been studied [62] where an imperfect barrier-well interface was considered. It was demonstrated that the total spin of the many electron system can be controlled through an external magnetic field as a result of Aharonov-Bohm oscillations [62]. However a combined study of potential device characteristics has so far been lacking. In Chapter 3 we therefore study the DOS, conductance and current-voltage characteristics of different geometric arrangements of three impurity clusters in order to interpret and tune quantum interference phenomena. In addition, naturally grown systems have not been considered at all so we also investigated disordered systems through different forms of disorder. We consider an imperfect interface between the impurity and matrix potentials as well as a random distribution of the impurity clusters.

We investigate the optimal conditions for the onset of resonant tunnelling. Of great importance is the development of radio frequency devices which can out-perform current devices. In this regard, low dimensional carbon resonant tunnelling diodes can excel at high frequencies and have shown great promise [50]. Carbon superlattices, with resonant tunnelling features and consequently ultra-high frequency capabilities could be developed from a combination of sp^3 hybridized carbon and sp^2 hybridized graphene. Controlling the graphitic clusters may make new applications available in amorphous carbon and nano-crystalline diamond films. In addition this study may also aid in interpretation of some of the transport features of some naturally grown systems such as reduced graphene oxide (RGO).

A recent study has revealed that the micro-structure of RGO, a chemically derived form of graphene, consists of intact graphene regions surrounded by functionalized regions (see Figure 1.7) [63]. Oxygen-functionalized regions are insulating and RGO can therefore be considered as a disordered, naturally grown quantum dot system. The synthesis of RGO,

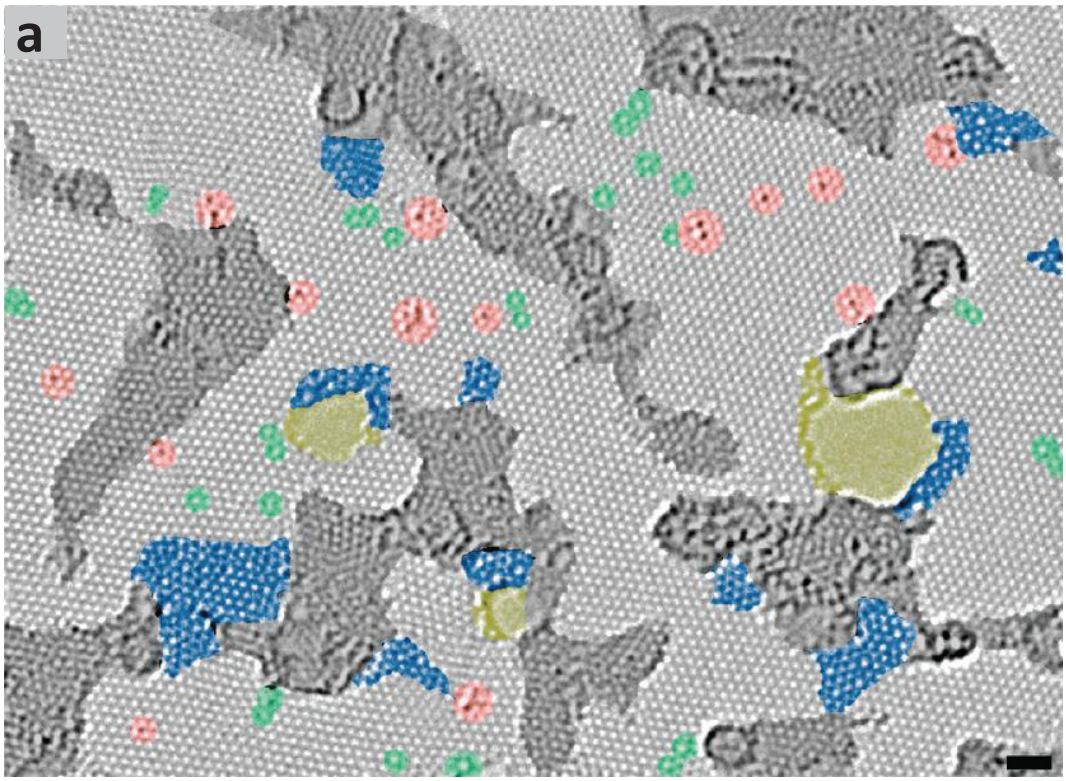


Figure 1.7: Atomic resolution transmission electron microscope image of reduced graphene oxide. The scale bar represents 1 nm. Dark grey regions represent residual functionalized regions and red regions represent individual adatoms. Blue regions represent regions dominated by topographical defects while green regions represent individual topographical defects. Vacancies are shaded yellow. Figure from [63].

being chemically based, is well suited for industrial-scale device preparation. In addition, the solubility of functionalized graphenes facilitates device fabrication [64]. Initially it was hoped that quantum transport features in RGO would be similar to those of pristine graphene providing a route to large-scale production of graphene however the conduction was found to suffer from strong localization. In another study, transport measurements showed Coulomb blockade features [65, 66]. A model was developed in which single electron tunnelling occurred through residual functionalized regions. Subsequent studies showed an improvement in the conductivity with activated charge carriers contributing to conduction [67]. Concurrently the magnetic properties of graphene oxide (GO) and RGO were also studied. The discovery of ferromagnetism in RGO at room temperature was surprising [68]. In parallel, computational studies indicated the formation of local moments as a result of residual functionalized groups, topographical defects and vacancies although many questions remain unanswered, for example the nature of ferromagnetic ordering [68].

In the conventional reduction of GO to form RGO, hydrazine is employed as the reducing agent. In addition to introducing defects and vacancies in the lattice, additional functionalized groups are formed which remain attached to the lattice. Alternative reducing agents were therefore investigated. Ascorbic acid (vitamin C) has been used to successfully reduce GO [69]. Ascorbic acid is better suited to large-scale production as it is not toxic in contrast to hydrazine which poses an environmental risk. The free radicals introduced in the reduction process are not necessarily the same as in hydrazine reduction. However studies of the transport properties of GO reduced in this manner had not yet been undertaken. Hence we have studied the electronic transport and magnetic properties of GO and GO reduced with ascorbic acid (Chapter 5). We find evidence of mesoscopic resistance fluctuations at low temperatures combined with activated carriers and prominent elastic scattering at higher temperatures.

Magnetism in graphene has attracted a great deal of interest in parallel with the interest in the transport properties. In Chapter 5 we have therefore also studied the magnetic properties of GO and RGO in conjunction with the transport properties as recent reports have demonstrated ferromagnetism in RGO [70]. The magnetic properties show a phase change from ferromagnetism at low temperatures to diamagnetism at higher temperatures.

Graphene spintronics is an emerging field driven by theoretical studies. With a relatively long phase coherence length, zero density of states at E_F and a small spin-orbit interaction it has been suggested that graphene may be well suited for specific spintronic applications [71].

Spin valves, spin polarized devices and even spin qubits have been suggested in graphene devices. On the other hand, it is difficult to induce stable magnetic moments due to the small spin-orbit coupling. Some studies of the spin dependent resistance of graphene devices have been carried out in the non-local measurement configuration. In this linear configuration, a current is driven across two ferromagnetic electrodes while the potential is measured in some region where there is no direct current flow [71]. In this way polarized spin currents were demonstrated in graphene devices with a spin relaxation length in the range of 1-2 μm, which is more than sufficient of the development of nano-spintronic devices.

Spintronics in graphene is also synonymous with spintronics of the surface states of 3D topological insulators [72] as low energy quasi-particles are described by the Dirac Hamiltonian in both cases. However the spin-orbit coupling in the two materials is very different. In graphene the spin orbit coupling is small and the spin polarization relaxation time is relatively long while the surface states of topological insulators have a strong spin-orbit coupling and therefore have a short spin relaxation time. The two systems can complement each other as the surface states of topological insulators can generate spin-polarized charge carriers while graphene can allow them to propagate with the spin intact [72]. Interestingly, the spin relaxation time in bilayer graphene is longer than in monolayer graphene possibly as a result of screening [73]. Based on these properties, the formation of spin qubits has been studied in graphene quantum dots [39]. In this study, the limitation of valley degeneracy was overcome by working with graphene nano-ribbons. Quantum dots could then be coupled through the Heisenberg exchange interaction while the coupling between dots was found to be controllable. On the other hand, studies of functionalized graphenes for spintronics applications have so far been limited. One *ab-initio* study however has suggested that spin-filters can be manufactured from zig-zag graphene nano-ribbons functionalized with oxygen on one side and hydrogen on the other [74].

The physics of electron correlations in graphene is being studied intensely. In particular, the interaction of local moments and conduction electrons has drawn significant attention as graphene systems allow access to unusual features which may reveal variations in the Kondo physics of these systems. In Chapter 6 we perform 4 probe transport measurements of RGO at low temperatures and high fields. This study reveals the significance of the interaction of local quantum spins and conduction electrons. We interpret a metal-insulator transition in resistance as a function of temperature within the Fermi liquid description of the Kondo effect. We find that the magnetoresistance scales with a characteristic temperature

which is in fair agreement with the Kondo temperature determined from resistance versus temperature measurements. We develop an interpretation based on the microstructure of RGO where local moments form as a result of free radicals, defects and vacancies while extended states form in low defect density graphene regions.

1.1 Outline

We begin this work with an $ab-initio$ study of the electronic properties of graphene and bilayer graphene chemically modified through the substitutional incorporation of single N impurities in Chapter 2. The band structure, density of states and charge density of bilayer graphene and N incorporated bilayer graphene are studied. We investigate the possibility of magnetism in N incorporated bilayer graphene. The diffusion of N atoms in graphene nano-ribbons is then studied by comparing the total energy of graphene nano-ribbons with N incorporated in the bulk and on the edge of the nano-ribbon.

After studying doping in graphene, in Chapter 3 we study the electronic electronic transport properties of impurity clusters embedded within a high potential matrix where the de Broglie wavelength is significant over the scale of the device. Assuming coupling between the leads and the clusters as well as indirect lead-cluster coupling through the direct inter-cluster coupling, we calculate the density of states, conductance and current-voltage characteristics. We study different geometric configurations in order to interpret quantum interference phenomena. With elemental concepts founded in these theoretical studies we then perform experimental studies on reduced graphene oxide which is effectively a disordered impurity cluster system.

In Chapter 4 we discuss the experimental techniques used for subsequent chapters. In Chapter 5 we present low temperature current-voltage measurements of GO and RGO suspended between micro-electrodes. We discuss resistance versus temperature measurements in detail and develop a model for the temperature dependence of RGO. We also present the magnetic properties of GO and RGO. Temperature dependent magnetization as well as low temperature hysteresis measurements are interpreted.

Extending the work of Chapter 5, in Chapter 6 we present four probe temperature dependent transport measurements on RGO from 2 K. Resistance is studied as a function of temperature and magneto-resistance is studied at different temperatures. The carrier den-

sity and mobility are determined from Hall measurements in the van der Pauw configuration. In Chapter 7 general conclusions with a view towards nano-electronic and spintronic device applications are presented.

Chapter 2

Electronic properties of Nitrogen Incorporated Bilayer Graphene

In this chapter the electronic properties of bilayer graphene and nitrogen nitrogen incorporated graphene and bilayer graphene in both the AA and AB configurations are studied through $ab-initio$ calculations within density functional theory (DFT). A brief introduction to DFT is presented. A more detailed review of theoretical and experimental aspects of nitrogen modification of graphene and bilayer graphene is given, building on the discussion in Chapter 1. The incorporation and subsequent diffusion of nitrogen atoms in monolayer graphene nano-ribbons is discussed based on a comparison of the calculated total energy of graphene nano-ribbons with nitrogen situated in the bulk and on the edge of the nano-ribbon. The band structure, density of states and charge density of bilayer graphene is then discussed and compared with bilayer graphene modified through nitrogen incorporation with a view towards electronic device applications. By stipulating different magnetic configurations and examining the total energy, we also discuss the magnetic properties.

2.1 Introduction

2.1.1 Introduction to Density Functional Theory

Calculation of the electronic properties of a system from $ab-initio$ principles begins with a Hamiltonian describing electrons, nuclei and their interaction as follows

$$H = -\frac{\hbar^2}{2m}\sum_i \boldsymbol{\nabla}_i^2 - \sum_{i,I}\frac{Z_I e^2}{\mathbf{r}_i - \mathbf{R}_I} + \frac{1}{2}\sum_{i\neq j}\frac{e^2}{\mathbf{r}_i - \mathbf{r}_j} - \frac{\hbar^2}{2M}\sum_I \boldsymbol{\nabla}_I^2 + \frac{1}{2}\sum_{I\neq J}\frac{Z_I Z_J e^2}{\mathbf{R}_I - \mathbf{R}_J} \quad (2.1)$$

where m and M are the electronic and nuclear masses, Z is the nuclear charge and capitol and lower case subscripts refer to nuclei and electrons respectively. This Hamiltonian accounts for electron-nucleus, electron-electron and nucleus-nucleus Coulomb interactions as well as the kinetic energy of electrons and nuclei. However when this Hamiltonian is applied within the Schrödinger equation, the resulting many-body problem, consisting of coupled differential equations (due to the two-body Coulomb interaction) of the order of the Hamiltonian, cannot be solved analytically while the computational expense of numerical techniques poses a severe limitation [75, 76]. The problem must therefore be reformulated to render it soluble.

A principle simplification exploits the fact that the nuclear mass is much greater than the electronic mass, allowing nuclei to be treated adiabatically within the Born-Oppenheimer approximation [77]. The Hamiltonian can therefore be separated into an electronic part and a nuclear part. The electronic system then consists of an electronic kinetic energy term, T (first term in the Hamiltonian), an electron-nucleus interaction term, V (second term) and an electron-electron interaction term U(third term). Wave function based methods for solving the electronic part of Eq. 2.1 have been developed to find the ground state however they are computationally expensive [76].

One of these methods is the Hartree-Fock method where the multi-electron wavefunction $\Psi(\mathbf{r}_1, \mathbf{r}_2, \ldots, \mathbf{r}_N)$ is expanded through a Slater determinant of single electron wavefunctions. A set of single electron Schrödinger equations is then solved, using a modified potential. However the Hartree-Fock method neglects correlation energy and therefore does not provide sufficient accuracy for general application of $ab-initio$ calculations. In addition, the computational demands increase rapidly with the system size. Density functional theory

(DFT) provides an alternative route and its use has become widespread as it often produces satisfactory results and is computationally feasible. DFT provides an efficient route to finding the groundstate density and energy of a system.

The ground state of a system can be obtained from a simple variational principle and we therefore restrict our discussion to the ground state. Ground state DFT methods essentially rely on the variational principle of quantum mechanics [78]. Given a wavefunction Φ, the energy of the system with Hamiltonian $\mathcal{H}$ as a functional of Φ is

$$E[\Phi] = \frac{\langle\Phi|\,\mathcal{H}\,|\Phi\rangle}{\langle\Phi|\Phi\rangle}\ . \tag{2.2}$$

Formally, it can be shown that the ground state is given by the minimization of the energy functional $E[\Phi]$. The ground state energy is the lowest possible energy, i.e. $E_i \geqslant E_0 \quad \forall \quad i$. This implies that $E[\Phi] \geqslant E_0$.

Hence, minimization of the functional $E[\Phi]$ yields the ground state energy, i.e.

$$E_0 = \min_{\Phi} E[\Phi]\ . \tag{2.3}$$

DFT exploits the electron density as the basic observable. The electron density operator is defined as

$$\hat{n}(\mathbf{r}) = \sum_{i}^{N} \delta(\mathbf{r} - \mathbf{r}_i) \tag{2.4}$$

so the density may be expressed as

$$\frac{\langle\Psi|\,\hat{n}(\mathbf{r})\,|\Psi\rangle}{\langle\Psi|\Psi\rangle} \tag{2.5}$$

i.e.

$$n(\mathbf{r}) = N \int d^3r_1 \ldots\, d^3r_N \Psi^*(\mathbf{r}_1, \mathbf{r}_2, \ldots \mathbf{r}_N)\delta(\mathbf{r} - \mathbf{r_i})\Psi(\mathbf{r}_1, \mathbf{r}_2 \ldots \mathbf{r}_N) \tag{2.6}$$

where Ψ is some wavefunction (not necessarily the ground state wavefunction). DFT relies on the reformulation of the kinetic energy, external potential and electron-electron interaction terms of Eq. 2.1 in terms of the electron density. We consider valence electrons as an inhomogeneous electron gas (following Hohenberg and Kohn [79]) including mutual Coulomb repulsion (U) and kinetic energy (T), confined to a region under the influence of

an external potential (V_{ext}) i.e. the electron-nuclear interaction is replaced with a collective external potential which acts on electrons. Considering a ground state Ψ, the the ground state energy may be expressed as

$$E = \langle\Psi|\, T + V + U \,|\Psi\rangle = \langle\Psi|\, T \,|\Psi\rangle + \langle\Psi|\, V_{ext} \,|\Psi\rangle + \langle\Psi|\, U \,|\Psi\rangle \ . \tag{2.7}$$

The expectation value for each term may then be expressed in terms of the one and two body density matrices [75] as

$$\langle\Psi|\, T \,|\Psi\rangle = -\frac{\hbar^2}{2m} \int [\boldsymbol{\nabla}^2_{\mathbf{r}} n_1(\mathbf{r}, \mathbf{r\prime})]_{\mathbf{r}=\mathbf{r\prime}}\, d\mathbf{r} \tag{2.8}$$

$$\langle\Psi|\, V_{ext} \,|\Psi\rangle = \langle\Psi|\sum_{i=1}^{N} v_{ext}(\mathbf{r}_i) \,|\Psi\rangle = \int n(\mathbf{r}) v_{ext}(\mathbf{r})\ d\mathbf{r} \ . \tag{2.9}$$

where $v_{ext}(\mathbf{r}_i)$ represents the potential when $n(\mathbf{r})$ is the ground state density of a non-interacting system. The Coulomb part of the electron-electron interaction term, U_C, (i.e. the Hartree contribution), may be expressed as

$$\langle\Psi|\, U_C \,|\Psi\rangle = \frac{1}{2} \iint \frac{n(\mathbf{r}) n(\mathbf{r\prime})}{|\mathbf{r} - \mathbf{r\prime}|}\, d\mathbf{r}\, d\mathbf{r\prime} \ . \tag{2.10}$$

However this only includes the classical part of the electron-electron interaction (as in the Thomas-Fermi model [78]). The total electron-electron interaction, U, also includes exchange-correlation effects.

With the basic elements in place, a brief development of DFT may now be given. The proof by Hohenberg and Kohn (H-K) that the ground state wavefunction of a many body system can be *completely* determined by the electron density forms the basis of density functional theory. The method of H-K allows the correct ground state energy to be determined without directly solving the many-body Schrödinger equation [79]. The charge density is the basic observable in the method of H-K. They proved that the ground state wavefunction $\Psi_0(\mathbf{r}_1, \mathbf{r}_2, ..., \mathbf{r}_N)$ may be calculated if the ground state charge density $n_0(\mathbf{r})$ is known. The electron density is defined as

$$n(\mathbf{r}_1) = N \int d^3 r_2 \int d^3 r_3 \ , \ldots , \int d^3 r_N \Psi^*(\mathbf{r}_1, \mathbf{r}_2, \ldots \mathbf{r}_N) \Psi(\mathbf{r}_1, \mathbf{r}_2 \ldots \mathbf{r}_N) \tag{2.11}$$

where N is the number of electrons in the system and $\Psi(\mathbf{r}_1, \mathbf{r}_2 \ldots \mathbf{r}_N)$ is general wavefunction.

They considered an interacting inhomogeneous electron gas under the influence of an external potential $v(\mathbf{r})$. The Hamiltonian also included kinetic energy terms and an electron-electron interaction term [79]. In the treatment which follows, we use the constrained search formalism as it clearly and concisely illustrates the essential features of the H-K theorems. This formalism, developed by Levy, guarantees the anti-symmetry requirement of the ground state wavefunction through a reformulation of DFT. The energy of the system, as a functional of the density [79, 80, 81] may then be written as

$$E_v[n] = \min_{\Psi \to n} \langle \Psi | \, T + U + V \, | \Psi \rangle \tag{2.12}$$

where the terms T, U and V represent the kinetic energy, the the electron-electron Coulomb interaction and the external potential respectively and Ψ represents the wavefunction corresponding to the density $n(\mathbf{r})$. If $n(\mathbf{r})$ is not the ground state density then application of the variational principle to Eq. 2.12 illustrates that the wavefunction which produces $n(\mathbf{r})$ is not the ground state wavefunction. The variational principle stipulates that the the minimum of $E_v[n] \geq E_{v,0}$ where $E_{v,0}$ is the ground state energy.

The ground state density is therefore the density which minimizes the the energy functional. This minimization may be written as

$$E_{v,0}[n] = \min_{n} [\min_{\Psi \to n} (\langle \Psi | T + U | \Psi \rangle + \int v(\mathbf{r}) n(\mathbf{r}) \, d\mathbf{r})] \; . \tag{2.13}$$

The kinetic energy and electron-electron interaction terms are universal [79, 81, 80] as they are independent of the external potential and their sum can be denoted as a functional of the electron density $F[n(\mathbf{r})]$, following the original notation of H-K. This is often termed the internal energy functional. In DFT calculations the external potential alone is system specific and calculations proceed on the basis of prescribed methods for dealing with the internal energy functional [80]. The ground state may then be represented as the minimum of the functional

$$E_v[n] = \int v(\mathbf{r}) n(\mathbf{r}) \, \mathrm{d}\mathbf{r} + F[n(\mathbf{r})] \tag{2.14}$$

provided that

$$\int n(\mathbf{r})\, d\mathbf{r} = N \ . \tag{2.15}$$

The density functional is associated with an anti-symmetric ground state wavefunction and it is dependent on the external potential. It was shown that the electron density is implicitly itself a functional of $v(\mathbf{r})$ which in turn is a unique functional of $n(\mathbf{r})$. Furthermore, as the system Hamiltonian relies on $v(\mathbf{r})$, the full many particle ground state is a unique functional of $n(\mathbf{r})$ [81]. This is illustrated in the so-called strong form of the H-K theorem which shows that changes in the external potential result in changes in the density. Herein lies the origin of the self-consistency requirements in DFT calculations.

The work of H-K allows the ground state energy to be determined through minimization of the energy functional with three spacial coordinates (non-degenerate case) without directly solving the many-body Schrödinger equation. All ground state observables are in turn functionals of the electron density so all the properties of the system can be uniquely determined from knowledge of the electron density. The H-K theorems can be applied to further simplify many particle systems.

H-K explicitly separated the Coulomb energy from the functional $F[n(\mathbf{r})]$, rewriting the energy functional as

$$E = \int v\left(\mathbf{r}\right) n\left(\mathbf{r}\right) d\mathbf{r} + \frac{1}{2} \int \int \frac{n\left(\mathbf{r}\right) n\left(\mathbf{r}'\right)}{|\mathbf{r} - \mathbf{r}'|} d\mathbf{r} d\mathbf{r}' + G\left[n\right] \ . \tag{2.16}$$

The H-K theorems may be employed in a different approach which reduces the many-body problem of interacting electrons to the problem of non-interacting single particles under the influence of an effective potential. In this approach the energy functional need not be explicitly minimized as in the approach of H-K. This work was pioneered by Kohn and Sham (K-S) [82]. They began with Eq.2.16 as an expression for the energy functional. K-S considered approximations for treating an inhomogeneous system of interacting electrons and developed methods for calculating the ground state of the system using self consistent equations [82].

Physically, the exchange energy must be accounted for as the many-body wavefunction must be anti-symmetric under exchange of electrons. The correlation energy can be interpreted through consideration of the actual wavefunction as a series expansion in which each term in the expansion is a Slater determinant, with each term satisfying the anti-symmetry

requirements [78]. This additional energy is incorporated in DFT through the combined exchange-correlation potential which depends on the one-electron density.

Beginning with Eq.2.16, K-S suggested an expression for $G[n]$ which includes exchange-correlation effects where the functional is separated into a kinetic energy functional and an approximated exchange-correlation functional based on a slowly varying electron density i.e.

$$G[n] \equiv T_s[n] + E_{XC}[n] \tag{2.17}$$

where $T_s[n]$ is the kinetic energy functional and $E_{XC}[n]$ is the exchange correlation energy functional.

Originally, the electron density was approximated as the density of a uniform electron gas in order to neglect local variations of the electron density [83, 76]. This approximation, the local density approximation (LDA), is robust and is still widely used. It simplifies inhomogeneous systems and allows the energy per unit volume to be used to determine the density and external potential [80].

The condition of a slowly varying density allows the exchange-correlation energy functional to be defined as

$$E_{XC}[n] = \int n(\mathbf{r})\epsilon_{XC}(n(\mathbf{r}))\ dr \tag{2.18}$$

where $\epsilon_{XC}(n(\mathbf{r}))$ is the exchange correlation energy *per electron*.

This approximation facilitates the expression of the functional $G[n]$ and the functionals of the kinetic energy and the exchange-correlation energy as a function of the electron density and allows the exchange-correlation energy to be expressed as the integral of the product of the density and the exchange-correlation energy per electron of a uniform electron gas. Finally, minimizing Eq. 2.16 yields

$$\int \delta n(\mathbf{r})[v(\mathbf{r}) + \int \frac{n(\mathbf{r}')}{|\mathbf{r}-\mathbf{r}'|}d\mathbf{r}' + \frac{\delta T_s[n]}{\delta n(\mathbf{r}))} + \frac{d(n\epsilon_{\chi C}(n))}{dn}]d\mathbf{r} = 0\ . \tag{2.19}$$

This equation may be more easily interpreted in terms of the original Hamiltonian consisting of a kinetic energy term, an electron-electron interaction term and an external potential

$$E[n] = T[n] + U[n] + V[n] = T_s[n] + V[n] + U[n] + E_{XC}[n] \tag{2.20}$$

where this equation clearly shows that the exchange-correlation energy can be interpreted as the difference between the real energy of the interacting system and the energy of a non-interacting system.

Provided that the integral over the electron density yields N (Eq. 2.15) we can divide Eq. 2.20 by an infinitesimal change in the the density and minimize yielding

$$\frac{\delta E_n}{\delta n(\mathbf{r})} = \frac{\delta T_s[n]}{\delta n(\mathbf{r})} + \frac{\delta V[n]}{\delta n(\mathbf{r})} + \frac{\delta U[n]}{\delta n(\mathbf{r})} + \frac{\delta E_{XC}[n]}{\delta n(\mathbf{r})} = 0 \tag{2.21}$$

which may be rewritten as

$$\frac{\delta E_n}{\delta n(\mathbf{r})} = \frac{\delta T_s[n]}{\delta n(\mathbf{r})} + v(\mathbf{r}) + v_H(\mathbf{r}) + v_{XC}(\mathbf{r}) = 0 \tag{2.22}$$

where the definition of the potential energy as a functional of the density is $V[n] = \int v(\mathbf{r})n(\mathbf{r})\ d\mathbf{r}$. The variational principle requires that the ground state density satisfies the stationary principle [78] which can be written as

$$\delta\{E_v[n] - \mu[\int n(\mathbf{r})\, d\mathbf{r} - N]\} = 0 \tag{2.23}$$

where μ is the Lagrange multiplier which is invoked to minimize the energy functional $E_v[n]$ subject to the constraint imposed by Eq. 2.15. The charge density for the non-interacting system can be defined as

$$n_s(\mathbf{r}) = \sum_i^N f_i |\phi_i(\mathbf{r})|^2 \tag{2.24}$$

where f_i is the occupation of the i'th K-S orbital and $\phi_i(\mathbf{r})$ is the K-S wavefunction which are required to be orthogonal.

The three potential terms may be replaced with a single potential term $v_s(\mathbf{r})$ for electrons in a non-interacting system. This results in the first of the K-S equations

$$v_s(\mathbf{r}) = v(\mathbf{r}) + v_H(\mathbf{r}) + v_{XC}(\mathbf{r})\ . \tag{2.25}$$

Using Eqs. 2.23 and 2.25 the chemical potential can be written as

$$\mu = v_s(\mathbf{r}) + \frac{\delta T_s[n]}{\delta n(\mathbf{r})}\ . \tag{2.26}$$

Thus the problem of a many-body interacting system has been replaced with a non-interacting system within an external potential $v_s(\mathbf{r})$. This potential may then be used in the Schrödinger equation with the single particle K-S orbitals

$$[-\frac{\hbar^2}{2m}\nabla^2 + v_s(\mathbf{r})]\phi_i(\mathbf{r}) = \epsilon_i\phi_i(\mathbf{r}) \ . \tag{2.27}$$

The explicit form of the non-interacting kinetic energy as a functional of the density is

$$T_s[n] = -\frac{\hbar^2}{2m}\sum_i^N \int d^3r \phi_i^*(\mathbf{r})\boldsymbol{\nabla}^2\phi_i(\mathbf{r}) \ . \tag{2.28}$$

In the approach of K-S the potential $v_s(\mathbf{r})$ is expressed as a functional of the electron density $n_s(\mathbf{r})$. Practical implementation begins with some initial estimate for the density $n_s(\mathbf{r})$. This charge density is then used to calculate the potential in terms of the K-S equations $v_s(\mathbf{r})$ so that the K-S orbitals $\phi_i(\mathbf{r})$ can be calculated. An updated charge density may then be calculated and the process is repeated iteratively.

An exact, general expression for the exchange and correlation energy has not yet been found either in terms of a density functional or the single-particle K-S orbitals. The success of DFT approaches relies on the exchange-correlation energy being considerably smaller than the kinetic energy, electron-electron interaction energy and the external potential (which is effectively the lattice potential). In DFT approaches, the Hartree approximation is employed to reduce the many-body wavefunction to a product of single particle wavefunctions which is a Slater determinant in order to preserve the anti-symmetry requirements. The correlation energy is the difference between the real ground state energy and the energy using one Slater determinant.

An explicit form for the exchange energy is

$$E_x\phi_i[n] = -\frac{q^2}{2}\sum_{j,k}\int d^3r \int d^3r' \frac{\phi_j^*(\mathbf{r})\phi_k^*(\mathbf{r}')\phi_j(\mathbf{r}')\phi_k(\mathbf{r}')}{|(\mathbf{r}) - (\mathbf{r}')|} \ . \tag{2.29}$$

Thus far, only electronic charge has been considered. When considering spin, the density must be divided into spin up and spin down components i.e. the total density is defined by the relation $n(\mathbf{r}) = n_\uparrow(\mathbf{r}) + n_\downarrow(\mathbf{r})$ and the magnetization is defined as $m(\mathbf{r}) = \mu_0(n_\uparrow(\mathbf{r}) - n_\downarrow(\mathbf{r}))$ where μ_0 is the Bohr magnetron. DFT can be generalized to include spin without significant

changes through the spin Hohenberg-Kohn theorem which is similar to the charge only H-K theorem but states that when coupled to an external magnetic field, the ground state wavefunction and consequently all ground state observables are unique functionals of the density (spin up and spin down) and consequently the magnetization. The primary difference is that the exchange-correlation functional is replaced with a modified exchange-correlation functional which accounts for the relative spin up and spin down densities. The LDA is replaced with the local spin density approximation (LSDA). The external potential becomes $v_{s\sigma}(\mathbf{r}) = v(\mathbf{r}) + v_H(\mathbf{r}) + v_{xc,\sigma}(\mathbf{r})$. The exchange-correlation energy may be expressed as a functional of the electron density as

$$E_{XC}^{LSD}[n_\uparrow, n_\downarrow] = \int d^3r n\epsilon_{XC}^{unif}(n_\uparrow, n_\downarrow) \tag{2.30}$$

where ϵ_{XC}^{unif} is the exchange-correlation energy per particle of a uniform electron gas. With charge densities for the spin up and spin down electrons, the K-S equations remain self consistent. It is possible that the K-S equations may converge to a minimum which is not the global minimum but a local minimum. This problem may be resolved by testing a number of different spin configurations. If all configurations converge to the same minimum, this is indeed the global minimum. A DFT approach can then be used to determine the magnetic properties of a system.

More accurate exchange-correlation functionals than the LSDA have been developed. One such functional is the generalized gradient approximation (GGA) of Perdew, Burke and Ernzerhof (PBE) [84]. The GGA differs from the LSDA in that it includes changes in the gradient of the local density as well as the local density itself. It is therefore better suited to non-uniform densities and may be expressed as

$$E_{XC}^{GGA}[n_\uparrow, n_\downarrow] = \int d^3r f(n_\uparrow, n_\downarrow, \boldsymbol{\nabla} n_\uparrow, \boldsymbol{\nabla} n_\downarrow) \ . \tag{2.31}$$

A similar expression for the GGA, without a spin polarized charge density dependence, exists for the spin independent case. A number of different functions $f(n_\uparrow, n_\downarrow, \boldsymbol{\nabla} n_\uparrow, \boldsymbol{\nabla} n_\downarrow)$ have been developed although the method of PBE is one of the simpler GGA's to implement while maintaining accuracy.

To simplify computation of the K-S electronic wavefunctions, they are expanded in a plane wave basis set, effectively treating the wavefunctions within the free electron approxi-

mation. A plane wave basis is ideally suited to periodic boundary conditions and simplifies transformations from real space to reciprocal space by fast Fourier transform. Based on ideal periodicity, Bloch's theorem can be invoked. The eigenstates of the K-S equations may then be represented as a summation of plane waves over reciprocal lattice vectors G

$$\phi_{k,i}(r) = \sum_{G} c_{i,G} e^{i(k+G)r} \tag{2.32}$$

where the wavevector k is inside the first Brillouin zone. It is these eigenstates of the K-S equations that form the band structure which is plotted along different paths in the first Brillouin zone.

However a prohibitively large plane wave basis set is required to expand the wavefunctions of the core electrons as these wavefunctions oscillate rapidly to fulfil the orthogonality requirements of the Pauli exclusion principle [83]. This computational limitation was circumvented through the use of pseudo-potentials which replace the ionic potential by a weaker, smooth pseudo-potential. The inner electrons of an atom are closely bound to the nucleus and therefore participate little in bonding. It is only the outer electrons which partake in bonding and we can therefore approximate the inner electron density and solve (self-consistently) only for the valence electron density while core electrons need only be considered as a pseudo-potential.

This approach is valid as the valence electrons play a more prominent role in the electronic properties than the core electrons (treated as fixed electrons) so the core electronic properties may be approximated with a smooth function provided that phase shifts are accounted for [83]. The Hartree and exchange-correlation potentials can then be calculated using the valence electron density and the external potential is approximated by the pseudo-potential. Using pseudo-potentials the oscillations of the wavefunction in the vicinity of ionic cores (all electron) can be minimized by replacing the wavefunction with a pseudo-wavefunction with the restriction that the norms of the wavefunction and pseudo-wavefunction are the same [85]. The plane wave basis set is therefore drastically reduced as the potential varies smoothly. The entire energy functional of the K-S equations is then modified and calculations are performed using the pseudo-wavefunctions of the pseudo-potential and a pseudo charge density. However fairly extensive computations are required to determine pseudo-potentials [85]. A related frozen core method overcomes these issues.

The projector augmented-wave (PAW) method of Blöchl uses the all electron wavefunctions and potentials [86, 85]. The eigenstates of the K-S equation are referred to as the all-electron (AE) wavefunctions. The real AE wave functions are mapped onto pseudo wavefunctions in a new Hilbert space by a linear transformation [86]. The Hilbert space is effectively separated into a spherical core region (each individual sphere is denoted μ) and an interstitial region. The linear transformation may be represented by

$$|\phi_n\rangle = \mathcal{T}|\tilde{\phi}\rangle = (1 + \sum_{\mu} \mathcal{T}_{\mu})|\tilde{\phi}\rangle \tag{2.33}$$

where $\mathcal{T}$ is a linear operator, the summation runs over the spherical core regions μ and the operator $\mathcal{T}_{\mu}$ acts only inside the sphere. This linear transformation is only effective in the local spherical region surrounding the core and smooths out the oscillations of the real wavefunction in the region of the core while leaving the wavefunction outside the core region (where the real wavefunction is relatively smooth) unchanged. The pseudo-wavefunction can be described by a smooth function, reducing the computational burden. However in using the PAW to reduce the number of plane waves required to describe the strong electron-ion interaction, each energy functional must also be treated within the PAW. Computations (self-consistent in the case of the present study) are then performed using the pseudo wavefunctions, the all electron wavefunctions can subsequently be retrieved using linear transformations.

Considering the local terms $\mathcal{T}_{\mu}$ within the core (augmentation) region, we can expand the AE wavefunctions through a linear combination of partial waves

$$|\phi\rangle = \sum_{i} |\varphi_i\rangle \, c_i \tag{2.34}$$

The pseudo-wavefunctions can be similarly expanded

$$|\tilde{\phi}\rangle = \sum_{i} |\tilde{\varphi}_i\rangle c_i \tag{2.35}$$

where the index i labels the atomic site, quantum numbers and the partial waves for the same site and atomic numbers. We can therefore express the AE wavefunction as

$$|\phi\rangle = |\tilde{\phi}\rangle - \sum_i |\tilde{\varphi}_i\rangle c_i + \sum_i |\varphi_i\rangle\, c_i \tag{2.36}$$

To specify $\mathcal{T}$ as a linear operator, the expansion coefficients c_i must be scalar products of the form

$$c_i = \langle \tilde{p}_i | \tilde{\phi} \rangle \tag{2.37}$$

where $\langle \tilde{p}_i|$ are projectors for the pseudo partial wavefunctions. In the core region, the pseudo-wavefunction must be equal to itself hence

$$|\tilde{\phi}\rangle = \sum_i |\varphi_i\rangle \, \langle \tilde{p}_i | \tilde{\phi} \rangle \tag{2.38}$$

Therefore

$$\sum_i |\varphi_i\rangle \, \langle \tilde{p}_i| = 1$$

which also implies that

$$\langle \tilde{p}_i | \tilde{\varphi}_j \rangle = \delta_{ij} \tag{2.39}$$

Using the expansion coefficients of Eq. 2.37 together with the expression for the pseudo-wavefunction in Eq. 2.38, the final expression for the AE wavefunction is given by

$$|\phi\rangle = |\tilde{\phi}\rangle + \sum_i (|\varphi_i\rangle - |\tilde{\varphi_i}\rangle) \, \langle \tilde{p}_i | \, \tilde{\phi} \rangle \tag{2.40}$$

The pseudo-wavefunctions can then replace the AE wavefunctions in the K-S equations with improved computational efficiency. The total energy becomes a functional of the new charge density of the pseudo-wavefunctions.

In this study we employ self-consistent $ab-initio$ methods for calculating the K-S ground state. Self-consistent methods have long been employed and have shown great reliability. The

calculations in this study were performed within the Vienna $ab-initio$ Simulation Package (VASP). VASP uses two independent, concurrent iterative procedures to determine the K-S ground state. One is the self-consistent determination of the charge density from which the potential can be calculated while the other is the diagonalization of the K-S Hamiltonian (expanded in a plane wave basis set) for a fixed potential whence the eigenfunctions of the K-S ground state can be determined. Both sub-problems are relatively easily solved [87, 88]. Iterations begin with some set of trial wavefunctions consisting of occupied states with additional unoccupied states and a "well informed" charge density. The initial charge density is the combined atomic charge densities of the atomic species. In the iterative minimization of the charge density, the input and output charge densities are mixed while the difference, the residual $R[n]$, is minimized.

The Hellmann-Feynman theorems can then be used to find the ionic forces which can be minimized to find the optimal (relaxed) ionic positions [83]. The Hellmann-Feynman force is the partial derivative of the total free energy of the K-S functional with respect to the positions of the ions [87].

2.1.2 Electronic Properties of Bilayer Graphene

In 2D materials thermal fluctuations are of great significance. Graphene exists as a metastable state mechanically exfoliated from stable 3D graphite, grown on SiC or by chemical vapour deposition, or chemically exfoliated from bulk graphite. It is believed that topological distortions perpendicular to the basal plane provide additional stability [1]. The band structure of bilayer graphene in the Bernal configuration has been widely studied. Tight binding studies assume both inter-layer and intra-layer hopping. Lattice sites directly above each other are referred to as dimer sites as a result of the relatively large overlap of p_z orbitals perpendicular to the graphene planes. Lattice sites which are not directly above each other are referred to as non-dimer sites.

Neglecting second nearest neighbour interactions, the transfer integral matrix is defined as the product of the sum of nearest neighbour plane waves and the nearest neighbour tight-binding matrix elements, following the brief treatment presented in the introduction (Bloch states are defined in Eq. 1.1). Out-of-plane coupling between all 4 atoms in the unit cell is considered. The resulting transfer integral matrix is of the form

$$\mathcal{H}_{t,AB,A'B'} = \begin{pmatrix} \epsilon_A & t_0 f(k) & t_4 f(k) & t_3 f^*(k) \\ t_0 f^*(k) & \epsilon_B & t_1 & t_4 f(k) \\ t_4 f^*(k) & t_1 & \epsilon_{A'} & t_0 f(k) \\ t_3 f(k) & t_4 f^*(k) & t_0 f^*(k) & \epsilon_{B'} \end{pmatrix} \tag{2.41}$$

where the primed indices indicate sites on a different graphene layer and

$$t_0 = \langle \phi_A | \mathcal{H} | \phi_B \rangle = \langle \phi_{A'} | \mathcal{H} | \phi_{B'} \rangle \quad , \quad t_1 = \langle \phi_{A'} | \mathcal{H} | \phi_B \rangle$$
$$t_3 = \langle \phi_A | \mathcal{H} | \phi_{B'} \rangle \quad , \quad t_4 = \langle \phi_A | \mathcal{H} | \phi_{A'} \rangle = \langle \phi_B | \mathcal{H} | \phi_{B'} \rangle$$

Only the small momentum regime is studied as in the description of monolayer graphene in Chapter 1. This facilitates reduction of the transfer integral matrix to the sum of a number of 2×2 matrices which illuminate the physics of bilayer graphene. The band structure in the region of the K points shows two parabolic bands, which mirror each other above and below E_F (see Fig. 1.4). Two bands touch at E_F which are related to non-dimer sites. There is a strong overlap between the p_z orbitals therefore there is an energy gap between the bands associated with dimer sites. Bilayer graphene may be described by 4 sub-lattices, one each atom in each layer.

The electronic structure of sp^2 hybridized carbon films has received significant attention not only towards practical device applications but also as a fundamental problem in the study of amorphous materials [89, 90]. The extreme fast-switching capabilities of carbon films has drawn widespread attention. Nitrogen incorporation has long been employed to enhance the conductivity of such films although the mechanism is not fully understood. With the advent of graphene, it is natural to study nitrogen (N) incorporation to modify the electronic properties. Additionally, studies of graphene systems will provide additional information which may help to interpret some of the features of graphitic systems specifically with regard to substitutional nitrogen incorporation. The incorporation of N in carbon films provides unique opportunities to modify the electronic structure. N may be incorporated as a substitutional dopant in either sp^2 or sp^3 hybridized phases [89]. In $a-C$ films especially, many $C-N$ complexes may form. The potential of N trap sites can therefore be tuned to enhance the electronic properties although further research is required to gain enhanced control of the gas-phase chemistry.

The realization of a bandgap in functionalized and disordered graphenes has motivated numerous studies [91, 92]. Furthermore negative differential resistance features have been

demonstrated in impurity-patterned graphene systems, a precursor to extreme fast-switching capabilities. In conjunction with the realization of localized magnetic moments in disordered and functionalized graphenes [70, 93] spin polarized devices may be developed. Nitrogen doping of graphene may result in a number of device applications including field emission, bio-sensing and possibly in the formation of novel field-effect transistors based on quantum transport phenomena [94].

Nitrogen incorporation through substitution has been achieved through a modified chemical vapour deposition technique (with the addition of NH_3 in the reaction) as well as through exposure of graphene to a radio-frequency nitrogen plasma [94]. It was found that substitutional N incorporation induces spatially localized states in the conduction band. In that study, $ab-initio$ calculations were employed to generate simulated STM images which illustrated depletion of charge above the nitrogen atom while experimental STM studies indicate the preservation of the original atomic configuration of graphene although with localized features appear with a triangular charge distribution [94].

In another study the electronic band dispersion near E_F and hence the transport properties of few layer graphene was shown to depend significantly on the number of layers as well as the stacking geometry of the layers and that ambipolar transport is only possible with Bernal stacking [95]. In addition it was shown that for two or more layers the π bands are split due to bonding/anti-bonding patterns while the σ bands remain largely unaffected. These calculations also show a small pseudo-gap in the vicinity of the K point.

A recent ab-initio study has illustrated the possibility of bandgap engineering in doped bilayer graphene [46]. Charge transfer between the graphene layers was studied through simulated STM images. Nitrogen was substitutionally incorporated in one of the layers with the other layer remaining pristine. Different stacking configurations were considered although the inter-layer stacking distance was not relaxed as van der Waals interactions are known to be a limitation in DFT calculations. The inter-layer separation has only a slight effect on the energy band dispersion although E_F can be shifted as a result of charge transfer from the nitrogen atom to the graphene [46]. Simulated STM images revealed a triangular region of localized charge centred around nitrogen atoms related to the spatial extension of electronic states associated with the nitrogen atom. Furthermore simulated measurements of bilayer graphene with N incorporated only in the bottom layer showed asymmetry in the charge distribution of the top layer, suggesting charge transfer between the layers. However, these results are likely an artefact of the coupling between the STM tip and the graphene

layers which is assumed in the simulations.

In a previous $ab-initio$ study of bilayer graphene the band gap was investigated as a function of the defect concentration (both nitrogen and boron substitutional impurities were considered in a single layer) which showed saturation in both cases [96]. It was also found that the band gap can be tuned through the application of a perpendicular external field as a result of screening effects between the layers. This was extended to include asymmetric substitutional doping through a modified tight-binding model consisting of short range and long range interactions [96]. The short range interaction was considered through a change in the on-site matrix elements at the substitutional site while the long range interaction was accounted for through a homogeneous field effectively incorporated in the on-site energy of all of the atoms in the layer where substitutional doping occurs. It was found that if doping is considered in both layers, the energy gap is smaller than if doping is considered in one layer only and it was noted that the energy gap is related to sub-lattice disorder [96].

Polymeric nitrogen chains situated in between two layers of graphene have also been investigated through $ab-initio$ studies [97]. The composite band structure was found to be a superposition of the band structure of both materials although both were offset as a result of electronegativity. Consequently, there is charge transfer between the graphene sheets and the nitrogen chain while the accumulated charge generates an electrostatic potential which stabilizes the hybrid structure. The transport properties of bilayer graphene suspended between gold electrodes were studied though a non-equilibrium Green's function (Keyldysh formalism) based on $ab-initio$ electronic structure calculations [98]. Interest in the electronic properties of bilayer graphene in the AA stacking configuration is growing amid mounting evidence that it can be realized practically. $Ab-initio$ calculations have demonstrated improved transmission in bilayer AA graphene nano-ribbons (GNRs) [98]. For realistic values of the inter-layer separation in the AA stacking configuration it was found that the coupling between the two layers influences the band gap. The transport properties of bilayer GNRs show higher conductance than monolayer GNRs although the conductance is larger in the AA than in the AB stacking configuration. It was illustrated that the inter-layer interaction has a marked effect on the transport properties which might be related to the overlap between π electrons localized at the edges of the graphene layers and it was found that GNRs may be metallic or semiconducting depending on the geometry of the edges.

The electronic transport of graphene is very sensitive to disorder, both topological and structural. Intuitively, bilayer (few layer) graphene is expected to be more robust to the

effects of disorder although the inter-plane coupling is small. We suspect that through the incorporation of nitrogen impurities the conductivity may be enhanced. We therefore study the effects of nitrogen incorporation through $ab-initio$ calculations. We begin with $ab-initio$ studies of N incorporated monolayer graphene to determine whether the energy is minimized with N incorporated in the bulk or on the edge of graphene nano-ribbons. We then study bilayer graphene and incorporate a nitrogen atom in each layer with AB stacking. We compare the nitrogen incorporated system with the pristine bilayer graphene. Similar analysis is repeated with the AA stacking configuration. We aim to determine if there is enhanced coupling between the layers. In addition we investigate the possibility of local magnetic moment formation.

2.2 Model and Computational Details

Nitrogen incorporation in bilayer graphene was studied through $ab-initio$ DFT calculations performed within the generalized gradient approximation (GGA) of Perdew, Burke and Ernzerhof (PBE) for the exchange-correlation energy. The LDA yields more accurate results than the generalized gradient approximation concerning the interaction between graphene layers in graphite [99]. However the electronic properties are more accurately determined using the GGA. The PAW [85] was used. The Kohn-Sham wavefunctions were expanded in a plane wave basis set with an energy cut-off of 600 eV. This large energy cut-off was used to find convergence despite the large vacuum. A Γ centred Monkhorst-Pack grid of $13 \times 13 \times 3$ was used for the first Brillouin zone to achieve convergence of the total energy with different k points and optimized for performance and accuracy. Electronic minimization was performed to an energy difference of 1×10^{-6} eV between successive iterations. For final band structure and density of states calculations, non-self consistent calculations were performed to keep the charge density fixed.

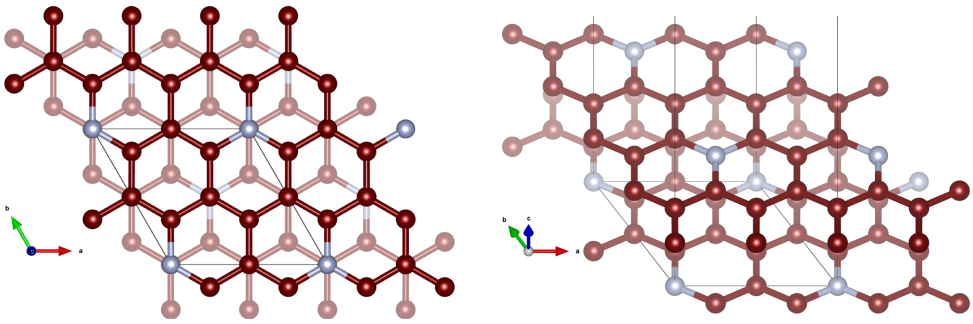
Ion and volume relaxations were performed until the energy difference between successive iterations was less than 3 meV and the external pressure proceeding a final static self-consistent calculation was less the 5 kB. In graphene systems, simultaneous relaxation of both the volume and the ionic positions is not advisable due to the large vacuum. Therefore the ionic positions were relaxed, then the relaxed ionic positions formed the input for volume relaxations, which were in turn used as the input for the next set of ionic relaxations and the process was repeated iteratively. A final static calculation was performed from which

the charge density was determined. Eventually the band structure and the density of states (DOS) could then be determined through non self-consistent calculations.

An initial inter-layer distance of 3.5 $\mathring{A}$ was used based on recent reports. Due to the periodic boundary requirements, repetitive sets of bilayer graphene are required to perform density functional calculations so the inter-layer-distance between the each set of bilayer sheets was assumed to be 10.6 $\mathring{A}$ to avoid any artefacts in the final results. The in plane inter-atomic distance was initially chosen to be 1.42 $\mathring{A}$.

Initially, N incorporation was studied in monolayer graphene nano-ribbons. A sufficiently thick nano-ribbon was used to minimize artificial effects as a result of boundary effects. This was determined by finding the total energy per atom as the width of the graphene strip was increased until sufficient convergence was achieved. The total energy for N incorporated in the bulk and on the edge was then determined after ionic and volume relaxation.

For pristine bilayer graphene, a unit cell with four atoms was used which was repeated indefinitely to form an infinite structure. Ionic relaxations, followed by volume relaxations were performed until the change in free energy was less than 3 meV. The Bernal (AB) and AA stacking configurations were considered.



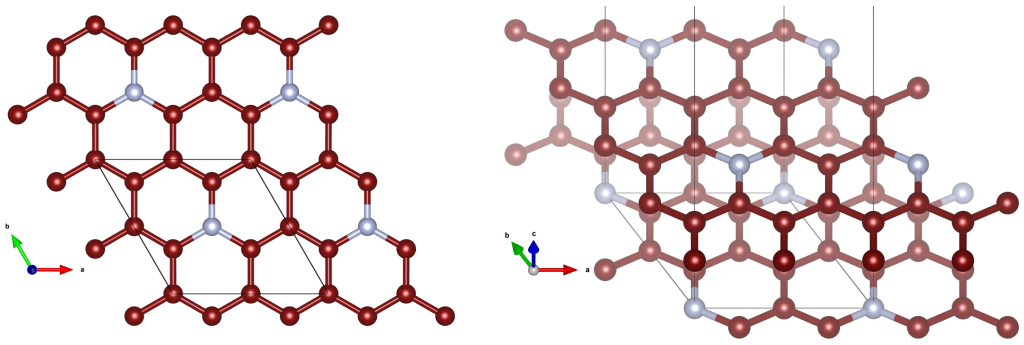
(a) (b)

Figure 2.1: AB configuration for nitrogen incorporated graphene from (a)viewpoint perpendicular to the basal (b) rotated view. Carbon atoms maroon while nitrogen atoms are white.

Figure 2.1(a) shows N incorporated substitutionally in bilayer graphene in the Bernal configuration. In the unit cell, consisting of 16 atoms, there is a single N atom in each graphene layer (Fig. 2.1(a)). The unit cell preserves the symmetry of the 4 atom unit cell of pristine bilayer graphene while the translational lattice vectors are scaled with the size

of the unit cell. In this configuration, we assume that the nitrogen atoms are not directly above each other.

In addition, N incorporated bilayer graphene in the AA configuration was studied to determine if there is enhanced inter-layer coupling (shown in Fig. 2.2(a)). In this case, we therefore assume that the nitrogen atoms are directly above each other. For both configurations (and in the case of pristine bilayer graphene) we begin with an inter-layer separation of 3.5 $\mathring{A}$ and an inter-atomic spacing of 1.42 $\mathring{A}$ before performing ionic and volumetric relaxation.



(a) (b)

Figure 2.2: AA configuration for nitrogen incorporated graphene from (a) viewpoint perpendicular to the basal graphene plane and (b) a rotated view.

Nitrogen incorporated bilayer graphene was subsequently studied considering substitutional N incorporation in both layers. A supercell with 16 atoms (14 C and 2 N, one in each layer) was investigated. The total atomic N percentage is approximately 14%. The inter-layer distance was assumed to be large, 10.6 $\mathring{A}$ with an initial in plane inter-atomic distance of 1.42 $\mathring{A}$ between C atoms and between C and nitrogen atoms. Relaxations were performed as described above. The AB and AA stacking configurations were considered. In the AA configuration, the nitrogen atom in one layer was placed above the nitrogen in the other layer while in the AB configuration the layers were shifted by a single atomic position.

2.3 Results and Discussion

After ionic and volume relaxation, the inter-atomic separation obtained for pristine bilayer graphene in both the AA and AB configurations was 1.42 $\mathring{A}$, which is practically the same

as the $C-C$ bond length found in other studies [44]. Considering N incorporated bilayer graphene in both configurations, the inter-atomic spacing of the $C-N$ bond is 1.41 $\mathring{A}$. This slight change modifies the inter-atomic distances throughout the lattice however this slight shift is within the expected error of the calculations. The inter-atomic distance between two C atoms (where one is bonded to a N atom) is 1.41 $\mathring{A}$ while the inter-atomic distance between C atoms which are bonded to C only is also 1.41 $\mathring{A}$. The inter-layer separation of N incorporated AA bilayer graphene is 3.48 $\mathring{A}$ while that of the AB configuration is 3.49 $\mathring{A}$. An inter-layer separation of 3.5 $\mathring{A}$ has been used in previous studies of bilayer graphene [100, 101, 102]. Substitutional N incorporation only slightly modifies the structure of bilayer graphene and therefore any changes in the electronic properties induced by N incorporation are independent of structural changes.

The band structure of pristine bilayer graphene in the Bernal configuration (determined from the eigenvalues of the Kohn-Sham equations) plotted along the path Γ, M, K, Γ, in the first Brillouin zone is shown in Fig. 2.3. Of primary significance are the four bands close to the K point where the energy bands coalesce near E_F. This is mirrored at the K' point at the corner of the Brillouin zone. At the K point, the valence and conduction bands touch at E_F. This is similar to monolayer graphene although the dispersion relation is parabolic in the region close to the K point. The energy bands only merge at the K and K' points. This similarity with monolayer graphene indicates that some of the symmetries of monolayer graphene are carried over to bilayer graphene.

There are two additional bands which are separated by a small energy gap, also with a parabolic dispersion relation close to the K point. From tight-binding studies, it was shown that the two bands which split are related to dimer sub-lattices while the two bands which touch are related to non-dimer sub-lattices [103, 25, 104]. In the tight-binding studies, the energy gap is approximately the same as the hopping term between the dimer sub-lattices. The hopping term between dimer sites is greater than the hopping term between non-dimer sites so the enhanced tunneling shifts the valence band below E_F. This is mirrored by an increase in the conduction band. It was also found that the in-plane hopping term is about a factor of nine greater than the inter-plane hopping term. The dispersion relation is parabolic only in a small region close to the K point. Further from the K points, the dispersion relation is linear over a small region. The conduction and valence bands are separated throughout the other high symmetry points in the Brillouin zone.

There is no intrinsic bandgap in bilayer graphene. However, the application of an external

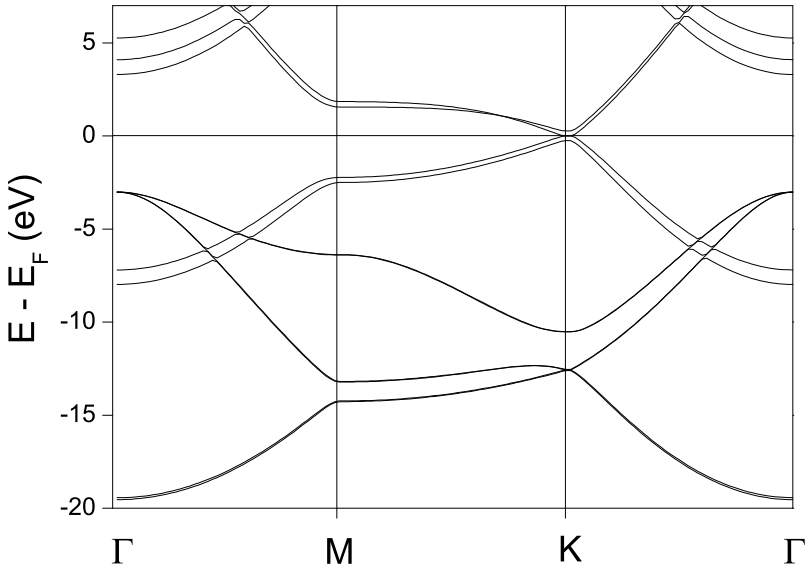


Figure 2.3: Band structure of pristine bilayer graphene in the AB stacking configuration.

potential can open up a controllable gap at the K points. Through a combination of tight binding and $ab-intio$ approaches it was shown (and experimentally verified) that the band-gap is related to the difference in on-site energies of the 4 atoms which make up the unit cell. This difference in the on-site energies is a result of the inter-layer asymmetry between the layers, the difference in energy of dimer and non-dimer sites and the different energy of in-plane sites in the unit cell induced by an external potential [105].

The parabolic dispersion relation of bilayer graphene is indicative of the difference between bilayer and monolayer graphene induced by the weak inter-layer coupling. Charge carriers in monolayer graphene are treated as massless chiral Dirac fermions close to the K points. In contrast, by studying only the region close to the K point (the low energy region) and the dispersion relation of non-dimer sites (i.e. the energy bands which touch at E_F) it can be shown that charge carriers in bilayer graphene can be described as massive chiral Dirac fermions [105]. There is also a difference in the Berry's phase between bilayer and monolayer graphene. The band structure in the AA configuration is significantly different.

The band structure of bilayer graphene in the AA configuration is shown in Figure 2.4. Close to the K point it is significantly different to the band structure of bilayer graphene in the AB configuration. Close to the K point there are still four bands around E_F as there are

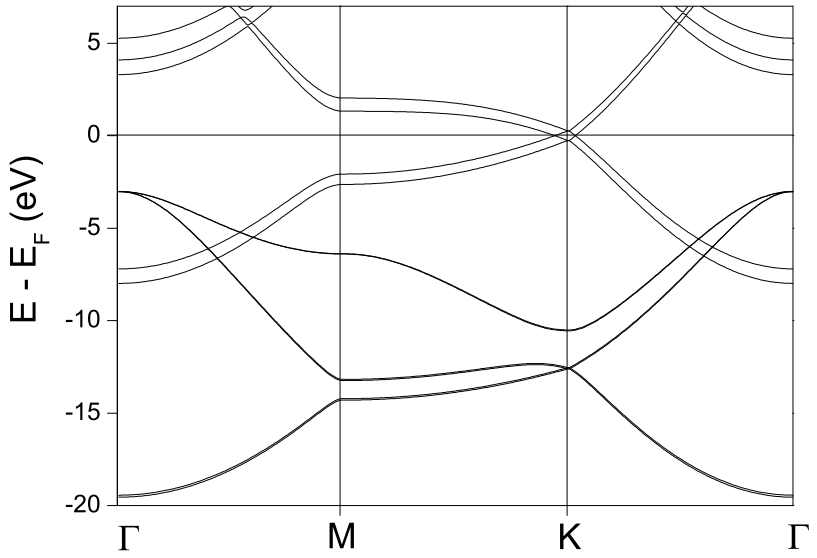


Figure 2.4: Band structure of pristine bilayer graphene in the AA stacking configuration.

four atoms in the unit cell. However, the two conduction and valence bands meet at E_F with a linear dispersion close to E_F. Two sets of triangles are formed which are symmetrically distributed about the K point and E_F. The four energy bands correspond to a pair of π bonding orbitals (valence band) and a pair of π anti-bonding orbitals (conduction band). In contrast to AB stacked bilayer graphene where charge carriers behave as free particles, charge carriers in AA stacked bilayer graphene behave as massless Dirac fermions, close to the K points. This may have implications for the mobility in AA bilayer graphene as direct carrier backscattering is prohibited (and nearly direct backscattering is reduced) in the Dirac regime although the increase in mobility might only be by a factor of two.

Comparing the band structure of the AA and AB configurations yields physical insight into the origins of the unusual electronic properties of bilayer graphene. In the AA configuration, all four sub-lattices are effectively dimers. The on-site energies are therefore the same for each term in the effective Hamiltonian. In the AB configuration the on-site energies are not necessarily the same, with the asymmetry destroying the linear dispersion of pristine graphene. The band structures are otherwise identical. As the inter-layer coupling is relatively small, the in-plane features dominate the band structure for both stacking configurations. In both the AA and AB stacking configurations, the valence (conduction) bands

which meet at E_F originate from π bonding (anti-bonding) bonds while the the other bands are related to to the in-plane sigma bonds [106]. These bands are therefore virtually identical for both configurations.

Subject to the neglect of non-dimer coupling, it has been shown through tight binding studies that the effective Hamiltonian for the AA configuration can be reduced to a 4×4 matrix in which the 2×2 matrices of monolayer graphene are repeated [107]. Each band is symmetrically shifted by the inter-layer coupling energy. Our $ab - initio$ calculations essentially show the same features. Physically, as the coupling between non-dimer sites is small the band structure is essentially composed of the band structure of two monolayers which are shifted from the K point as a result of the symmetry of the inter-layer coupling.

DFT calculations of the band structure of graphite are prone to numerical errors. The origin lies with the large inter-layer separation and the concomitant weak inter-layer interactions which are improperly accounted for in DFT. Long range interactions can be partially accounted for through a modified exchange-correlation term however this modification is not exact and can introduce artefacts. As DFT is not well suited for long range electrostatic interactions, including the van der Waals interaction in calculations for bilayer graphene is not expected to improve the accuracy of calculations of the electronic properties. Additionally, there is only a slight change in the potential with inter-layer separation in the region of 3.5 $\mathring{A}$ so numerical errors are to be expected. Interpretation of DFT calculated band structures of graphitic systems must therefore be checked thoroughly for consistency. In the present study, the band structure calculated for the AA configuration is similar to the band structure calculated using the tight binding method [100, 101, 102]. In those studies, the inter-layer separation was assumed to be in the region of 3.5 $\mathring{A}$.

The inclusion of the van der Waals interaction is expected to play a role in the determining the inter-layer separation as it influences the charge distribution of the layers. The GGA employed in the present study depends predominantly on the local charge density and takes no account of the non-local van der Waals interaction [108] which in this case is the Coulomb interaction between the nuclei and electrons of the two graphene layers. In fact, the inter-layer separation of graphite obtained from calculations using the LDA has been found to be more accurate than the inter-layer separation found using the GGA for the exchange-correlation energy [109]. A complete description of the van der Waals interaction would entail solving the many body problem for long range electron correlations, infeasible for all but the barest systems [76].

Conventional DFT describes accurately covalent interactions but even with modifications to the theory there is still contention surrounding the inclusion of non-covalent interactions. A number of van der Waals functionals have therefore been developed however the reliability of these functionals is not guaranteed. The accuracy of these methods is specifically dependent on the system under investigation so it is difficult to determine the applicability of specific functionals prior to calculation [110]. Where there is some overlap between the charge densities of the two layers, the van der Waals interaction may be included in the semi-local LDA/GGA [109]. However, in bilayer graphene the inter-layer separation even larger than that of graphite so inclusions of the van deer Waals interaction are even more prone to error.

In $ab-initio$ studies of bilayer graphene nano-ribbons, the van der Waals interaction has been included as a modification to atomic orbitals through a non-local potential in the K-S equations, however the accuracy of these results is subject to interpretation and verification using a fully non-local van der Waals density functional [111, 112]. In a subsequent study, a non-local density functional [113] was employed [112]. The binding energies calculated in this study were similar to the experimental values. However, the inclusion of the van der Waals interaction may induce artefacts as a result of the artificial non-local density functional.

The principle effect of including the van der Waals interaction would be to change the inter-layer separation but previous studies have shown that the electronic properties are not highly sensitive to the inter-layer separation, the general features are not significantly effected [114]. For the purposes of the present study, the general features as a proof of concept are more important than the exact electronic properties based on an exact value for the inter-layer separation. In this study we have therefore neglected the van der Waals interaction, opting instead to interpret the results of our calculations using the LDA with the effects of the van der Waals interaction in mind, rather than running the risk of finding artefacts in the electronic properties as a result of the van der Waals functional. Indeed, it is only in the case of pristine bilayer graphene where the calculated inter-layer separation has been unexpected, all other values have been within acceptable range of the experimental values.

In the present study, ionic relaxations were performed in an attempt to determine the correct inter-layer separation with the known limitations of relaxing graphitic systems in mind. This approach was favoured over introducing a van der Waals density functional to eliminate artifacts of this functional as described above. For the AA configuration, we find

that by performing ionic relaxation the inter-layer separation, initially assumed to be 3.50 $\mathring{A}$, relaxes to 4.49 $\mathring{A}$. This is most likely an artefact as the inter-layer separation is quite large so the charge densities of each layer experience a long-range interaction which influences the inter-layer relaxation. In the AA configuration, the charge densities are stacked directly on top of each other and a slight increase in the inter-layer separation might therefore expected although the increase in inter-layer separation seems to be too large as the inter-layer interaction at 3.5 $\mathring{A}$ is already weak. The inter-layer separation in the AA configuration was therefore held fixed at 3.5 $\mathring{A}$.

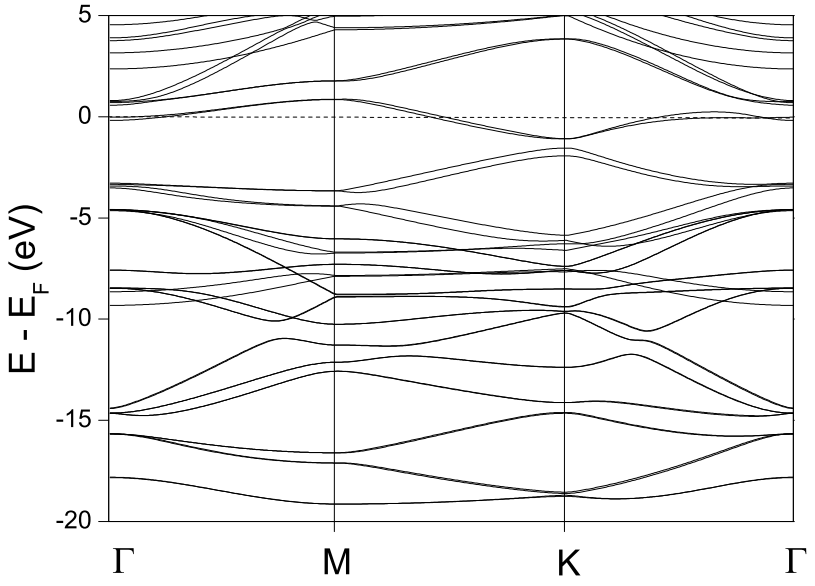


Figure 2.5: Band structure of nitrogen incorporated bilayer graphene in the AB stacking configuration.

When N is incorporated, three of the valence electrons form σ bonds with adjacent carbon atoms. Of the two remaining valence electrons, one occupies a π bonding state while the other occupies a π anti-bonding state [43, 115]. In studies of nitrogen incorporated monolayer graphene, the local DOS was used to affirm that the bands closest to E_F at the K point are π and π^* bands [115]. Figure 2.5 shows the band structure of N incorporated bilayer graphene in the AB configuration. The two pairs of bands closest to E_F at the K point are similar to the π and π^* bands of pristine graphene. The π and π^*-like bands dip below E_F at the K point while both pairs of bands become separated. N incorporated bilayer

graphene is therefore metallic. The bands separate due to modification of the p_z orbitals of the non-dimer sites. The bands are likely pairs of π and π^* bands as in monolayer graphene where the there are two bands instead of one as a result of dimer sub-lattices as discussed earlier. This could be confirmed through future studies of the projected density of states.

The π^*-like bands approach each other close to the K point while the separation of the π-like bands is much greater. A parabolic dispersion around the K point is maintained which is symmetric close to the K point although the gradient is less steep than the gradient of the parabolic dispersion of pristine bilayer graphene. This shows that the mobility is reduced with N incorporation. The reduction in the gradient is related to the loss of symmetry when N is incorporated in the unit cell as the energy levels of C and N are different. There are still four bands at the K point (close to E_F) as a result of the p_z orbitals of dimer and non-dimer sites which still dominate the electronic properties. The σ-like bonding bands are also modified due to the substitutional incorporation of the N as N plays a role in bonding. There are more bands in the band structure plots than for pristine bilayer graphene as a larger unit cell was used to incorporate nitrogen atoms in the graphene planes. The basis vectors are therefore larger in real space, so the Brillouin zone is smaller in reciprocal space. The correct symmetry (hexagonal) was still found in the output of the VASP software.

Substitutional N incorporation in one of the layers of bilayer graphene was studied by Guillaume *et al.* [46]. Structural modifications as a result of the N incorporation were found to be minimal. In that study, the inter-layer separation was not relaxed, the reason being the difficulties of incorporating the van der Waals interaction in DFT calculations. They considered a small concentration of N incorporated in the graphene layer, 0.25%, however N was found to have a substantial effect on the band structure, inducting metallicity (n-type doping). The low concentration, together with the minimal structural change suggest that the change in band structure is principally related to the loss of symmetry in one of the graphene layers. A gap (within the valence band at the K point) was also induced in a study of substitutional nitrogen doping in one layer of a graphene bilayer by Menezes [96]. In these studies, the band structure was not symmetric about the K point as N was incorporated in a single layer only so the symmetry was broken in a single layer only. A comparison of the gap found in the study by Guillaume (using the LDA) and that found by Menezes (using the GGA) shows a 0.1 eV difference indicating there is little difference in the band structure calculated using the two different exchange-correlation functionals although it should be noted that DFT is known to underestimate the band gap, regardless of the

exchange-correlation employed. The principle difference between the present study and the previous studies just mentioned is that N was incorporated in both layers, not only a single layer.

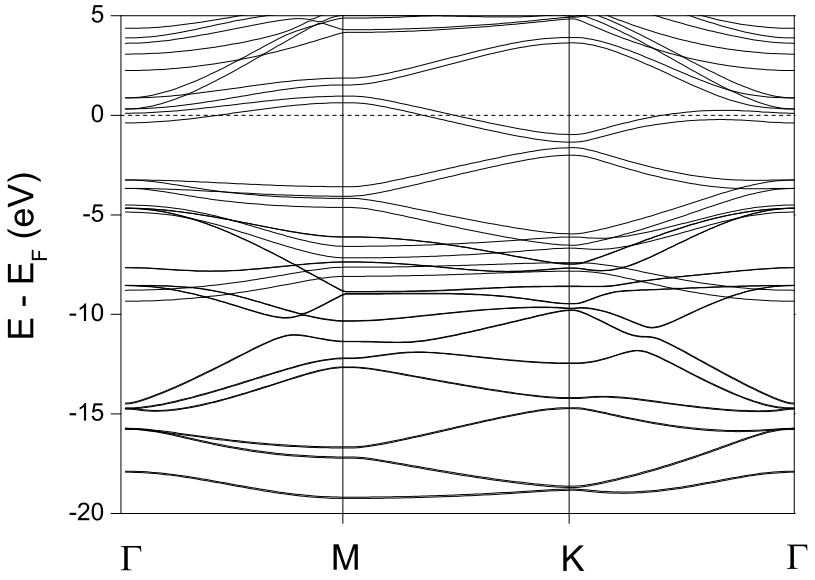


Figure 2.6: Band structure of nitrogen incorporated bilayer graphene in the AA stacking configuration.

Figure 2.6 shows the band structure for N incorporated bilayer graphene in the AA configuration. The most significant change in comparison with pristine AA bilayer graphene is that the linear dispersion close to the K point is lost so the nature of charge carriers changes. The band structure bears significant similarity to the band structure of the N incorporated bilayer graphene in the AB configuration although there are slight differences. The π^*-like bands do not approach each other as in the AB configuration. The separation between the bands is still smallest at the K point while the dispersion relation is also parabolic in this region. However the separation of the π and π^*-like bands, related to the overlap of p_z orbitals of dimer and non-dimer sites, is greater than in the AB configuration. In the AA configuration, there is likely greater overlap of the p_z orbitals so the bands split. The bands remain widely separated across all paths in contrast to the AB configuration where the bands approach each other. Concurrently, the separation between the π and π^*-like bands of non-dimer sites (where the energy bands at the K point almost touch) is

reduced. The changes in the σ-like bands in comparison with the AB configuration are minimal despite the increase in the prevalence of the p_z orbitals.

When N is substitutionally incorporated in the sp^2 hybridized graphene network, a lone pair of electrons is localized in the region of the N atom. This will also reduce the mobility as scattering increases. However n-type doping is advantageous in many applications [116].

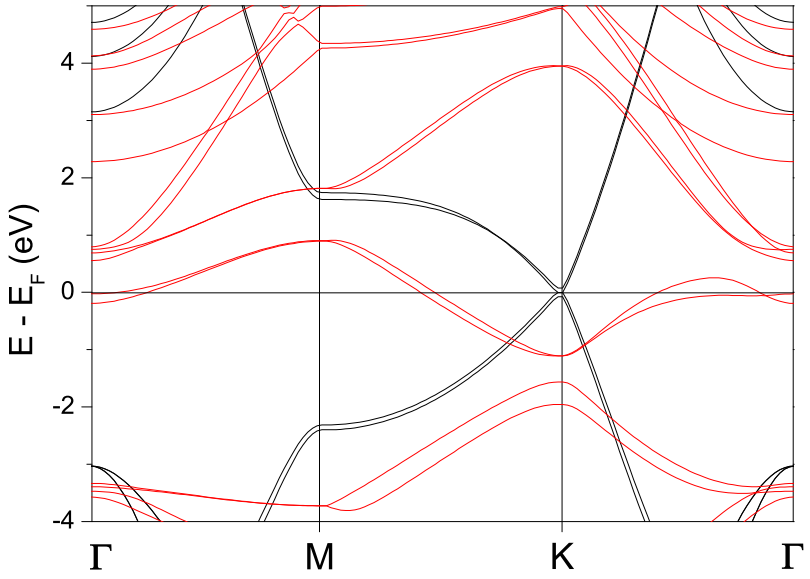


Figure 2.7: Comparison of the band structure of pristine (black) and nitrogen incorporated (red) bilayer graphene in the AB stacking configuration.

Figure 2.7 shows a comparison of the band structure of pristine bilayer graphene (black) and N incorporated bilayer graphene (red). This comparison clearly shows the difference in the gradient close to the K point. In addition, the dispersion along the path from M to Γ (and from K to Γ) is very different, increasing rapidly for pristine bilayer graphene but decreasing for N incorporated bilayer graphene. Similar features are also found in comparing pristine and N incorporated bilayer graphene in the AA configuration (shown in Fig. 2.8).

The density of states (DOS) for pristine bilayer (black) and N incorporated bilayer graphene (red) in the AB configuration is presented in Fig. 2.9. The DOS of pristine bilayer graphene is zero close to E_F, in accord with the band structure where the π and π^* bands touch at the K point. However the DOS is zero over a fairly large range. This

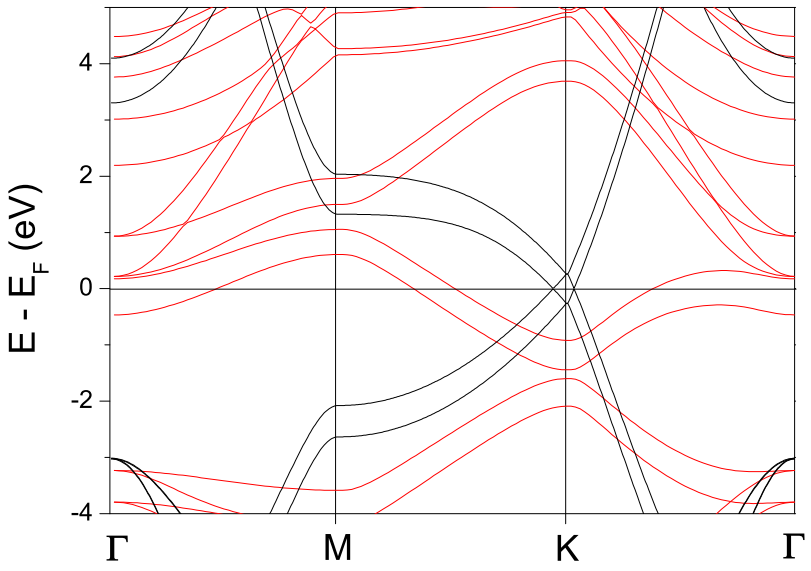


Figure 2.8: Comparison of the band structure of pristine (black) and nitrogen incorporated (red) bilayer graphene in the AA stacking configuration.

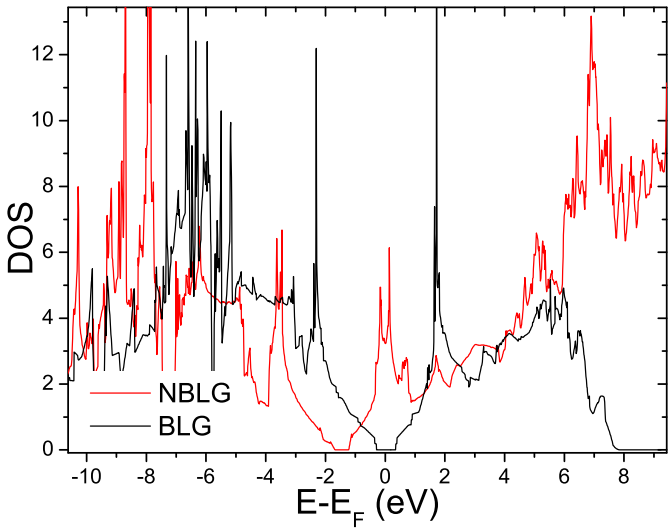


Figure 2.9: Density of states for pristine bilayer graphene (black) and nitrogen incorporated bilayer graphene (red) in the AB stacking configuration.

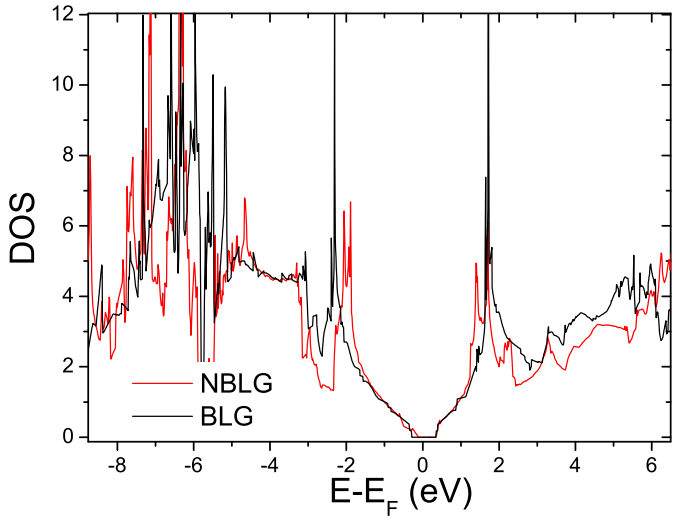


Figure 2.10: Density of states for pristine bilayer graphene (black) and nitrogen incorporated bilayer graphene (red) in the AB stacking configuration the nitrogen incorporated DOS shifted.

unexpected feature may be due to a combination of factors. For a parabolic dispersion (as for bilayer graphene), the density of states is constant. In bilayer graphene, as in monolayer graphene, the density of states is zero at E_F. Therefore for bilayer graphene the DOS is zero over a finite region where the dispersion of the π and π^* bands is parabolic. This is in contrast to monolayer graphene where the DOS is zero only at E_F and non-zero everywhere else [6]. In addition, there may have been too few sampling points in the calculation. Future studies might resolve the discrepancy. In monolayer graphene, the DOS is expected to be linear close to E_F as the dispersion relation is linear. In the present case, there are two sharp peaks in the DOS, one just below $2eV$ and the other just below $-2eV$.

These are van Hove singularities which coincide with the M point in the Brillouin zone where the derivative of the energy dispersion relation is zero. These van Hove singularities are also a feature of monolayer graphene which is to be expected as the band structure of bilayer graphene is similar to the band structure of monolayer graphene except for the region close to the K point. In the present case, two prominent peaks at each of the first van Hove singularities can be resolved. This is related to the first two bands at the M point above and below E_F (in contrast to monolayer graphene where there is only a single band). The DOS in higher (lower) energy regions is similar to the DOS of monolayer graphene as the

higher energy regions are related to σ bands.

The DOS of N incorporated bilayer graphene is shifted to lower energies compared to the DOS of pristine bilayer graphene. This shift in the DOS is related to the electrons added to the system through N incorporation. The DOS is still zero in the vicinity of -1.75 eV indicating that the dispersion relation might be parabolic in that region. The van Hove singularities are still prominent with the secondary peaks (around 0 and -3.5 eV) showing even greater separation than for pristine bilayer graphene. Other features are comparable with pristine bilayer graphene as shown in Fig. 2.10.

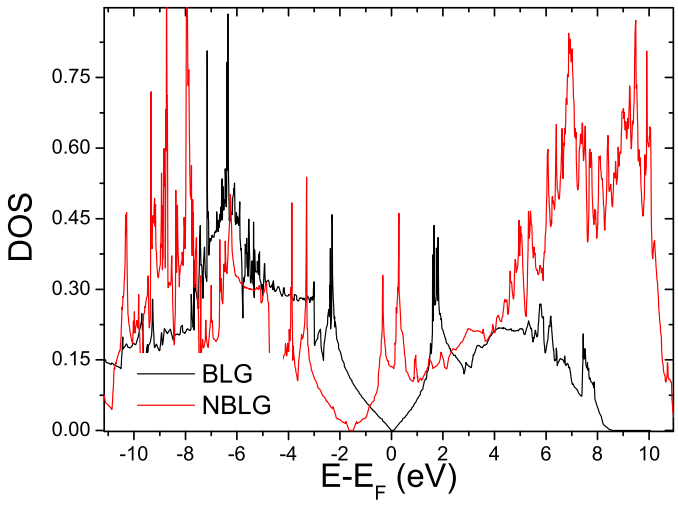


Figure 2.11: Density of states of AA stacked bilayer graphene (black) and nitrogen incorporated bilayer graphene (red).

The DOS of pristine (black) and N incorporated (red) bilayer graphene is shown in Fig. 2.11. The DOS for the pristine case is zero only at E_F as it is for monolayer graphene. Close to E_F there is a small region where the DOS is linearly dependent with energy. Other features, such as the van Hove singularities, are virtually the same as monolayer graphene. In agreement with the AB configuration, the introduction of N effectively shifts the DOS spectrum to negative energy (-1.75 eV). Circa -1.75 eV the DOS is zero as a result of the band gap induced through N incorporation. The secondary peaks in the van Hove singularities are clearly separated as the separation between the energy bands is large. Fig. 2.2(a) shows the DOS with the N incorporated DOS shifted by 1.75 eV so that the features can be compared. The features are practically identical. In Fig. 2.13 the DOS for N incorporated

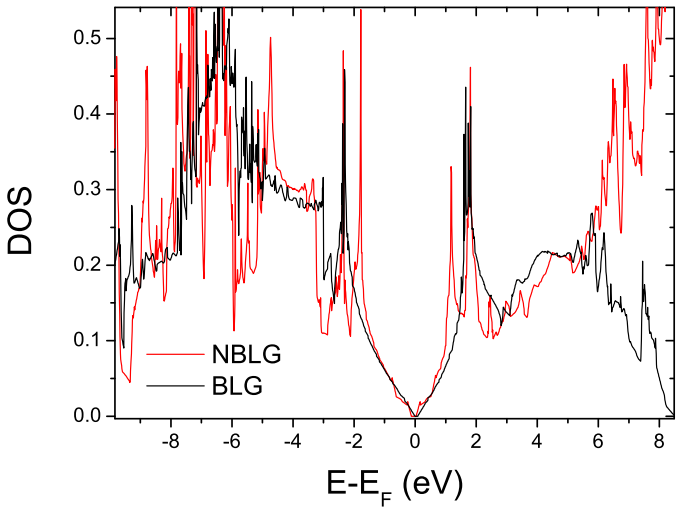


Figure 2.12: Comparison of density of states of AA stacked bilayer graphene (black) and nitrogen incorporated bilayer graphene (red) with the nitrogen incorporated shifted.

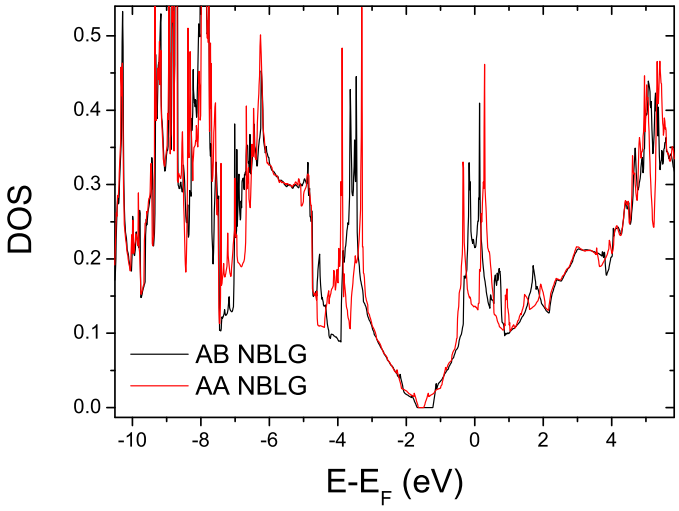


Figure 2.13: Comparison of the density of states of nitrogen incorporated bilayer graphene in the AA (black) and AB (red) stacking.

bilayer graphene for both configurations is shown. The most significant difference is in the region of -1.75 eV where the DOS is zero in the AB configuration over a wider range than

for the AA configuration.

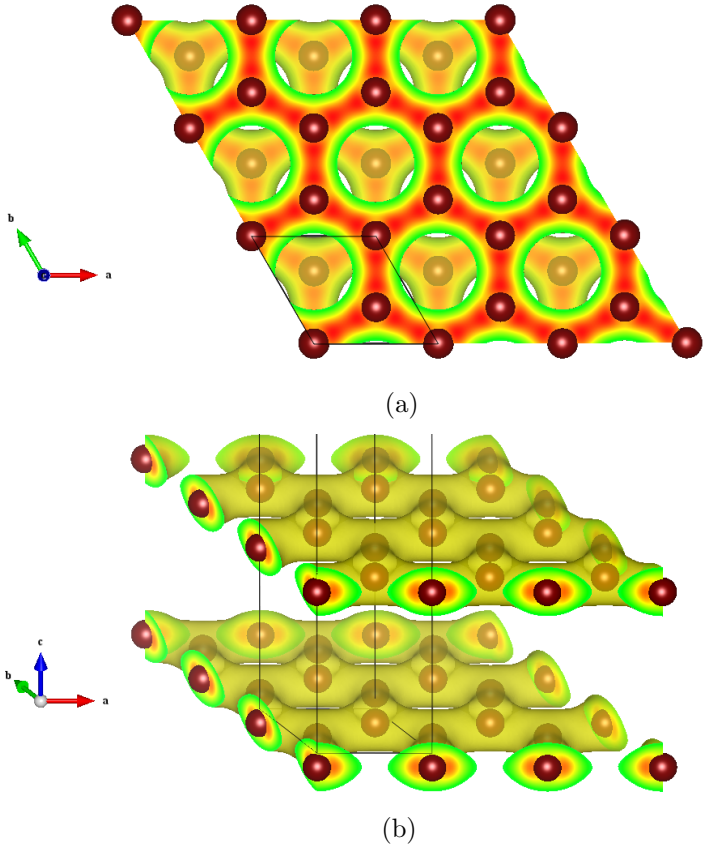


Figure 2.14: Charge density of pristine bilayer graphene in the AB configuration (a) view from above (b) viewed at an angle.

The charge density of pristine AB bilayer graphene is shown in Fig. 2.14(a). Red indicates regions of high charge density while green indicates regions of lower charge density. The charge density is highest along the σ bonds. From a rotated perspective (Fig. 2.14(b)), it can be seen that the charge density is restricted to the graphene planes. The charge density hardly extends out perpendicularly from the graphene planes although the charge density of the p_z orbitals extends slightly out of each atom. In addition, there is no charge between the graphene planes as the inter-layer separation is relatively large, hence the inter-layer coupling is minimal.

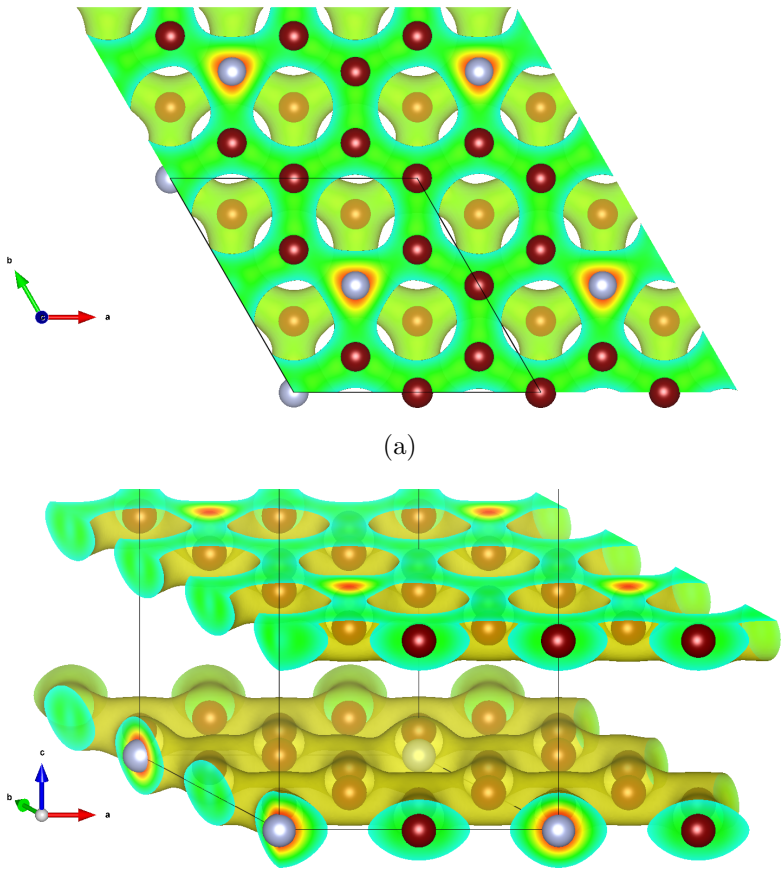
The charge density of N incorporated bilayer graphene is shown in Fig. 2.15(a) (AA configuration) and Fig. 2.16(a) (AB configuration). The inclusion of N results in localized charge density in the vicinity of N impurity. The charge density is highest in a symmetric,

roughly triangular region surrounding the impurity. Substitutional N partakes in sp^2 bonding, hence the charge density is highest in the vicinity of the σ bonds. The two N electrons which are not involved in bonding are localized above (and symmetrically below) the N atom (see the bottom layer). In a region close to the atomic plane but perpendicularly above the plane (the top layer) the charge density above the nitrogen atoms is triangularly distributed. This has also been reported in other studies [46, 94].

The localization of charge, coupled with the reduced gradient of the dispersion relation will be of significance in the carrier transport of N incorporated bilayer graphene. In the AB configuration, the localization of charge will increase scattering while the reduced gradient of the dispersion relation implies reduced mobility. In the AA configuration, the effect of N incorporation is more dramatic. The localization of charge, coupled with the change in the dispersion relation in the vicinity of the K point from linear to almost parabolic implies that carrier transport will be in a different regime. However it is in the induced metallicity that the advantage of N incorporation is realized.

The vast majority of research in graphene has been towards applications in nano-electronics. Driven by the advantages afforded by ever smaller devices, graphene nano-ribbons will likely form the backbone of graphene based nano-electronic devices. However, diffusion of dopants becomes significant in nano-scale devices. To this end we have also studied N doping of (monolayer) graphene nano-ribbons. A graphene nano-ribbon was studied with sufficient width that boundary effects were negligible. Due to the periodic boundary requirements of DFT, the abrupt edge of a nano-ribbon can affect the plane waves used in calculations. However, the width of the nano-ribbon dramatically increases computational time as well. We found that a graphene nano-ribbon about 7.5 $\mathring{A}$ thick was sufficient to preclude artifacts associated with the boundary. We assumed that the nano-ribbon is infinitely long as it is not required to be of finite length to study the diffusion of impurities. Each edge was terminated in the zig-zag configuration.

Identical nano-ribbons, one with N in the bulk and the other with N on the edge were studied. Proceeding ionic relaxation, the total energy was compared when a N impurity was incorporated into the bulk (close to the centre of the nano-ribbon) and incorporated onto the edge of the nano-ribbon. It was found that the total energy is far less when N is incorporated onto the edge. The difference in the total energy of the system was found to be 2.4 eV which is a fairly substantial change considering that the position of a single atom changes. The pristine graphene lattice is stable and in a low energy state. Although N



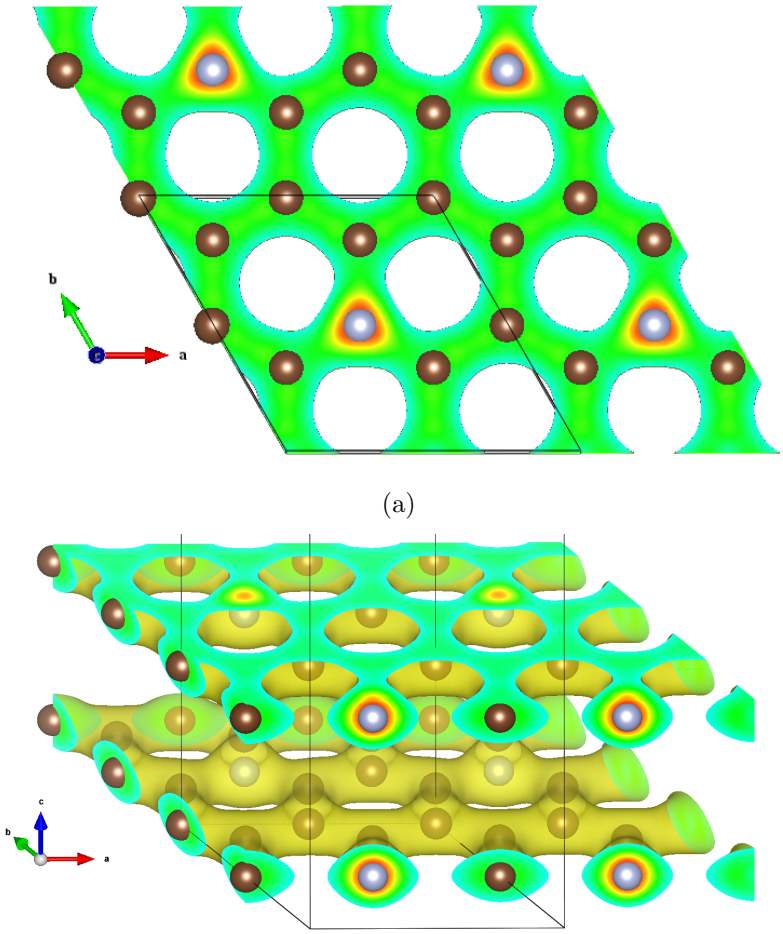
(a)

(b)

Figure 2.15: Charge density of nitrogen incorporated bilayer graphene in the AB configuration (a) view from above (b) viewed at an angle.

can be incorporated substitutionally, the total energy of the system increases. The system responds by attempting to eject the N impurity so the N impurity moves around in the lattice until the edge of the nano-ribbon is reached. The diffusion of the N impurity can be hindered by lattice distortions, vacancies etc. This effect must be borne in mind when considering high levels of N incorporation. As more nitrogen atoms migrate to the edge of the material, recombination to N_2 becomes more likely, therefore the atomic N percentage would saturate at some level. In addition, the effective modification of the edge states of graphene nano-ribbons may be achieved by exploiting the migration of N impurities.

We have also studied the possibility of the formation of local magnetic moments in bilayer



(a)

(b)

Figure 2.16: (a) Charge density of nitrogen incorporated bilayer graphene in the AA configuration. (b) Viewed at an angle

graphene induced through N incorporation based on the lone pair of electrons which are localized in the region of the N impurity. The total energy of the system was compared with two excess net spins (-143.20 eV) and with zero net spin (-143.66 eV). As the energy of the system is less with zero net spin, the system is unlikely to be magnetic.

2.4 Conclusion

N incorporation has little effect on the structure of bilayer graphene, only slightly modifying

the bond length. The charge density shows that excess charge is localized in the vicinity of the N impurities not only in the basal graphene planes but also in the out-of-plane direction. Studying the charge density of the AA configuration with N impurities situated one above the other revealed that there is little inter-layer coupling of the impurities as a result of the large inter-layer separation. A comparative study of the total energy of different possible spin configurations shows that the system is unlikely to display any net magnetization.

Band structure calculations show that the π bonding and anti-bonding bands meet at E_F at the K point for bilayer graphene in the AA and AB configurations. In the AB configuration, the dispersion relation is parabolic while in the AA configuration the dispersion relation is linear close to the K point. Some previous works have studied the band structure of bilayer graphene as the stacking arrangement changes from the AA configuration to the AB configuration. What has as yet been unknown is how the band structure of both configurations differs in chemically modified graphenes. We have studied the electronic properties of bilayer graphene modified through the substitutional incorporation of nitrogen. The band structure of N incorporated bilayer graphene is metallic with the π anti-bonding bands dipping below E_F and is similar in both the AA and AB configurations which indicates that the stacking-alignment of the graphene layer is insignificant in relation to the changes induced through N incorporation.

The reduction in the gradient of the dispersion relation with N incorporation for the AB configuration indicates that the effective mass of charge carriers increases in the vicinity of the K point, implying reduced mobility. For the AA configuration, the nature of the charge carriers changes from Dirac-like to free electron like. The segment of the dispersion relation which is free electron-like is larger for the AB configuration than for the AA configuration implying that the mobility is less in the AA configuration.

The changes in the dispersion relation also suggest that the nature of carrier scattering changes with N incorporation. Carrier scattering from long range potentials has been widely studied in pristine graphene and bilayer graphene however studies of chemically modified graphenes have so far been lacking. The localization of charge in the vicinity of nitrogen impurities indicates the formation of charge puddles. Carrier scattering from charge puddles is being actively studied in graphene and bilayer graphene. In this respect, N incorporated bilayer graphene may provide an ideal system for studying carrier scattering from charge puddles (an active area of research in graphene and bilayer graphene) as nitrogen does not induce significant structural changes.

Chapter 3

Tuning Resonant Transmission Through Geometrical Configurations of Impurity Clusters

In Chapter 2 the changes to the electronic properties induced through the chemical modification of graphene and bilayer graphene by single N impurities were studied. Impurity clusters are more stable in nano-materials and are less likely to drift than single impurities as discussed in Chapter 2. In this chapter we extend the study of Chapter 2 to an investigation of the quantum transport properties of nano-electronic devices composed of impurity clusters within a high bandgap material. Resonant tunnelling features were examined through the inter-play between the size of the clusters and the inter-cluster distance. Constructive interference phenomena were tuned through a systematic study of different geometrical configurations, thereby controlling confinement in quasi-bound states. Gaussian trap potentials have been used to simulate the imperfect barrier-well interface associated with disordered materials. Strongly localized states can be formed successfully despite weak disorder as illustrated by breaking the symmetry in the horizontal configuration. To this end, triangular cluster configurations were investigated under a variety of conditions including various shapes and orientations. The effects of disorder, created effectively by arbitrary configurations, destroy the Fano resonance which is prevalent in conductance spectra and consequently reduce the peak to valley ratio of the resonant peak in current vs. voltage curves. However the formation of two quasi-bound states is demonstrated, suggesting possible applications for disordered naturally grown systems of impurity clusters. This study

addresses the controlled lifetime of quasi-bound states and can inform the design of fast switching devices based on high band gap materials by the astute incorporation of impurity clusters with specific geometrical configurations. This analysis can be extended to carbon-based quantum dot systems and could play a role in the development of innovative quantum transport devices.

3.1 Introduction

The introduction of dopants to high band gap semiconductors to form single and isolated impurity centres is motivated by the promise of electronic transport properties superior to those of conventional devices [117, 118]. In carbon systems this results in the formation of localized clusters [48, 119, 120, 121, 122] which have also demonstrated resonant tunnelling features and related improved electrical transport however a thorough theoretical model has not yet been available to interpret these results [123, 124]. The tunnel electronic properties of $sp^2 - C$ clusters embedded in $sp^3 - C$ regions have been studied considering a quasi-1D system where resonant features can be tuned by N incorporation [125]. Further studies have investigated the tunnelling properties of different N complexes which can be incorporated into sp^2 clusters. For a distribution of N centres and clusters in defective graphene systems, tunable negative differential resistance (NDR) features have been illustrated [54, 126]. Nevertheless these models cannot interpret the effect of the geometry of impurity clusters on device characteristics as effectively as described in the seminal work by Matveev and Larkin [127, 128].

In this model, a low concentration of impurity centres was considered, yielding a small value of inter-coupling constant, which was successfully used by Savchenco and co-workers for two impurity centres in GaAs systems although the effect of geometry of the clusters was not discussed [129, 130]. It was later illustrated that the geometry of the impurity cluster array strongly influences the conductance maxima, the energy of conductance maxima and the lifetime of quasi-bound states formed though quantum interference phenomena [57]. Based on this work, quantum device applications have been suggested in a number of studies however only artificially grown perfectly ordered systems were considered [61, 59, 58, 131, 132, 56, 60]. Here we investigate the possibility for device applications in naturally grown impurity clusters considering their wider spectral tolerance. Hence a detailed understanding of quantum interference phenomena arising from geometrical considerations is essential in

the development of devices.

It has been widely noted that the indirect inter-dot coupling through the leads is more prominent than the direct inter-dot coupling, so the transport properties are dominated by the indirect coupling through the leads [57, 61, 59, 58, 131, 132, 56, 60]. A study of two quantum dots showed conductance spectra described by the superposition of two Lorentzians representing two states. As the lead-dot coupling was changed, the rate of decay of one of the states increased while the rate of decay of the other state decreased correspondingly [57]. This is analogous to the Dicke effect where the interaction of non-degenerate two level molecules with a common radiation field leads to the formation of a "super-radiant" state (at a specific eigenvalue of the system) where the spontaneous radiation rate in the super-radiant state is far greater than in any other state [133]. In graphene quantum dot systems, strongly localized states can be produced with an infinite trapping time [134, 55]. This has motivated the construction of a wave-guide structure using an array of multiple i.e. three quantum dots [58, 131, 132, 56, 60].

Previously some idealized configurations of three dots were studied in the context of quantum interference phenomena under the application of an external magnetic field [58, 131, 132, 56, 60, 134] however a systematic analysis of arbitrary configurations has not yet been carried out. Most importantly, previous theoretical models have not been employed to generate negative differential resistance (NDR) features for an electronic device whose characteristics would suffer from both structural and topological disorder associated with a distribution of impurity clusters. It is well known that quantum interference effects are strongly influenced by the geometry of the quantum dot array. Furthermore the size of the clusters can enhance the direct coupling between the dots [62] revealing that a combination of quantum dot size and inter-dot spacing would be necessary to improve the transport of an inhomogeneous system treated as a superlattice.

Here we study the prominent NDR features for three impurity clusters (quantum dots) of variable size and inter-cluster spacing embedded in a high potential material for different geometrical configurations i.e. horizontal, vertical and triangular. A comprehensive study of these different geometrical as well as rotational configurations can unveil the optimum configurations for observing NDR features which could lead to control of these features in nano-electronic devices. We show that the geometry of the quantum dot configuration can be exploited to control the lifetime of bonding and anti-bonding states as a principle step towards practical implementation of embedded arrays of impurity clusters.

3.2 Model

The conductivity through a quantum dot array can be described within a modified form of the Shahbazyan-Raikh model [57] by extension of their original work on two impurity channels to n impurities. We consider impurity clusters (quantum dots) distributed within a high band-gap material. The device dimensions are of the order the de Broglie wavelength and ideal semi-infinite leads, with a continuum of states, are assumed. In the present study devices up to 16 nm from source to drain were investigated. There is an implicit gate voltage dependence built into the model as well. We consider circular impurity clusters with an imperfect interface between the impurity clusters and the high bandgap matrix. The potential is therefore represented as a two dimensional Gaussian. A schematic diagram is shown in Figure 3.1. In real space, this model allows two-dimensional geometric configurations of the clusters to be considered.

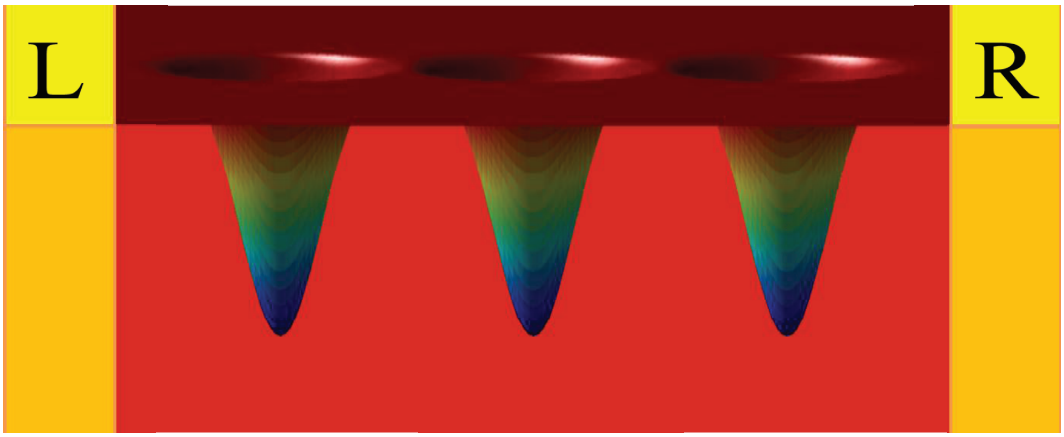


Figure 3.1: Schematic 3D diagram of the impurity cluster system including the leads and the 2D Gaussian potential. The regions in red indicate the high bandgap matrix while the multicoloured regions indicate the impurity cluster potential.

Here we consider direct coupling of each of the impurity clusters to the leads. We also consider direct coupling between the impurity clusters and indirect coupling between the impurity clusters through the continuum states of the leads. The Hamiltonian of the leads and the quantum dot array [57] can be expressed by

$$\mathcal{H} = \sum_v E_v^L a_{Lv}^\dagger a_{Lv} + \sum_v E_v^R a_{Rv}^\dagger a_{Rv} + \sum E_i a_i^\dagger a_i + \sum_{v,i} V_{vi}^L \left(a_{Lv}^\dagger a_i + a_{Lv} a_i^\dagger \right) + \sum_{v,i} V_{vi}^R \left(a_{Rv}^\dagger a_i + a_{Rv} a_i^\dagger \right) + \sum_{i \neq j} V_{ij} a_i^\dagger a_j \tag{3.1}$$

where $E_v^L \left(E_v^R \right)$, $a_{Lv}^\dagger \left(a_{Rv}^\dagger \right)$ and $a_{Lv} \left(a_{Rv} \right)$ are the energy and creation and annihilation operators of the left (right) continuum state respectively. E_i, $a_i^\dagger$, and a_i are the energy, creation and annihilation operators of the i-th impurity state ($i = 1, 2, \ldots, N$) respectively. The term V_{vi}^L (V_{vi}^R) represents the matrix element of the impurity potential between the left (right) continuum state v and the i-th impurity state. V_{ij} is the overlap matrix element between the impurity clusters.

The exact time-dependent wavefucntion is the superposisiton of the continuum wavefucntions of the leads $\left(\Psi_v^L, \Psi_v^R \right)$ and the wavefunctions of the impurity clusters (Ψ_i) i.e.

$$\Psi = \sum_v C_v^L(t) \Psi_v^L + \sum_v C_v^R(t) \Psi_v^R + \sum_i C_i(t) \Psi_i \ . \tag{3.2}$$

The prefactors are determined through the separated Schrödinger equations.

$$\begin{aligned} i\hbar \frac{\partial}{\partial t} C_v^L(t) &= E_v^L C_v^L(t) + \sum_i V_{vi}^L C_i(t) \\ i\hbar \frac{\partial}{\partial t} C_v^R(t) &= E_v^L C_v^R(t) + \sum_i V_{vi}^R C_i(t) \\ i\hbar \frac{\partial}{\partial t} C_i(t) &= E_i C_i(t) + \sum_i V_{iv}^L C_v^L(t) + \sum_i V_{iv}^R C_v^R(t) + \sum_{i \neq j} V_{ij} C_j \ . \end{aligned} \tag{3.3}$$

Initially, the wavefucntion is restricted to the left lead as all other states are as yet unoccupied. We therefore impose the boundary condition

$$C_v^L(0) = \delta_{vv_0} \quad , \quad C_v^R(0) = 0 \quad , \quad C_i(0) = 0 \ . \tag{3.4}$$

The system of differential equations may be solved to find $C^R_{\mu_0}(t)$. The rate of transfer from a state v_0 in the left lead to a state μ_0 in the right contact may then be defined by

$$W\left(Lv_0|R\mu_0\right) = \lim_{t\to\infty}\left[\frac{d}{dt}|C^R_{\mu_0}(t)|^2\right] \ . \tag{3.5}$$

The limit is taken to infinity as the misalignment of the chemical potential (induced when a potential difference is applied across the leads) eventually drives the system to the state μ_0 in the right lead. Using the expression for $C^R_{\mu_0}(t)$, Eq. 3.5 can be reduced to the golden rule form

$$W(Lv|R\mu) = \frac{2\pi}{\hbar}|T_{v\mu}|^2\delta\left(E^L_v - E^R_v\right) \tag{3.6}$$

where $T_{v\mu} = \sum_{ij} V^L_{vi}S_{ij}V^R_{j\mu}$ is amplitude of the transition between the states v and μ. Here, S_{ij} is a propagator matrix which describes all transitions between the impurity and continuum states. The matrix $\hat{S}$ is given by $\hat{S} = \left[E_F - \hat{E} - \hat{V} + \frac{i}{2}\left(\hat{\Gamma^L} + \hat{\Gamma^R}\right)\right]^{-1}$ where

$$\hat{V} = \begin{cases} V_{ij} = V_{ji}, & \text{i} \neq \text{j} \\ 0, & \text{i} = j \end{cases} \qquad i,j = 1,2,\ldots,N$$

and $\hat{E}$ is the diagonal energy matrix. The matrix elements of $\hat{\Gamma}^{L(R)}$ are given by $\hat{\Gamma^L_{ij}} = 2\pi\sum_v V^L_{iv}V^L_{vj}\delta\left(E_F - E^L_v\right)$ and $\hat{\Gamma^R_{ij}} = 2\pi\sum_v V^R_{iv}V^R_{vj}\delta\left(E_F - E^R_v\right)$. These matrices represent the left and right lead coupling constants respectively.

The conductance through the impurity system is given by a summation which runs over all states, from the initial states to the final states at E_F,

$$G\left(E_F\right) = 2e^2\sum_{\mu,v} W(L_v|R_\mu)\delta(E_F - E^L_v) \ . \tag{3.7}$$

Using the golden rule form and the terms defined previously, the conductance can be expressed by

$$G\left(E_F\right) = \frac{e^2}{\pi\hbar}Tr\left(\hat{\Gamma^L}\hat{S}\hat{\Gamma^R}\hat{S^\dagger}\right) \ . \tag{3.8}$$

The matrix elements $V_{ij}^{L(R)}$ are given by

$$V_{iv}^{L(R)} = \int dr\Psi_i(r)V(r)\Psi_i^{L(R)}(r) \approx \Psi_v^{L(R)}(x_i, y_i)\int dr\Psi_i(r)V(r) \ . \tag{3.9}$$

Treating the lead wavefunctions as plane waves (along the y direction) and the wavefunction within the high potential as an evanescent mode (along the x direction) the matrix elements can be represented as

$$V_{iv}^{L(R)} = e^{ik_y y_i - kx_i}\Psi^{L(R)v}(0,0)\int dr\Psi_i(r)V(r) = e^{ik_y y_i - kx_i}\lambda_i^{L(R)} = e^{ik_y y_i}\beta_i^{L(R)} \ . \tag{3.10}$$

Γ is defined by a summation over the lead states, which can be reduced to the averaging over $\mathbf{k}$. For diagonal elements which do not depend on the orientation of $\mathbf{k}$ the model yields $\Gamma_{ii}^{L(R)} = 2\pi g(E_F)(\beta_i^{L(R)})^2$ where $g(E_F)$ is the density of states at E_F. For non-diagonal elements the matrix product $V_{iv}^{L(R)}V_{vi}^{L(R)}$ has an additional prefactor $e^{ik_y(y_i-y_j)}$ and averaging over $\mathbf{k}$ yields $\Gamma_{ij}^{L(R)} = 2\pi g(E_F)\beta_i^{L(R)}\beta_j^{L(R)}J_0(k_s s_{ij})$, where s_{ij} is the distance between the i-th and j-th impurities along the y axis and J_0 is the Bessel function.

Combining these relations we can determine the Γ components

$$\Gamma_{ij}^{L(R)} = \Gamma_{ji}^{L(R)} = \alpha_{ij}\sqrt{\Gamma_{ii}^{L(R)}\Gamma_{jj}^{L(R)}}$$

where $\alpha_{ij} = J_0(k_F s_{ij}) = J_0(2\pi s_{ij}/\lambda_d)$

We now consider the specific case of three impurities. We define the centre of the device (half way between the leads) as the centre of the co-ordinate system,

$$\begin{aligned}\Gamma^{L(R)} &= 2\pi g(E^F)(\beta_i^{L(R)})^2 = 2\pi g(E_F)(e^{-kx_i^{L(R)}}\lambda_i^{L(R)})^2 \\ &= 2\pi g(E_F)\left(e_i^{-k(D+d_i/2)}\lambda_i^{L(R)}\right)^2 = \Gamma^{L(R)}e^{-kd_i}\end{aligned} \tag{3.11}$$

where d_i represents the distance from the centre of the device to the centre of the i-th cluster and D is the centre of the co-ordinate system. We assume that the leads are identical therefore $\lambda_i^L = \lambda_i^R$ and $\Gamma^L = \Gamma^R = \Gamma$. The coupling matrix for the left lead may then be

written as

$$\hat{\Gamma^L} = \Gamma \begin{pmatrix} e^{-kd_1} & \alpha_{12}\sqrt{e^{-kd_1}e^{-kd_2}} & \alpha_{13}\sqrt{e^{-kd_1}e^{-kd_3}} \\ \alpha_{12}\sqrt{e^{-kd_1}e^{-kd_2}} & e^{-kd_2} & \alpha_{23}\sqrt{e^{-kd_2}e^{-kd_3}} \\ \alpha_{13}\sqrt{e^{-kd_1}e^{-kd_3}} & \alpha_{23}\sqrt{e^{-kd_2}e^{-kd_3}} & e^{-kd_3} \end{pmatrix} \tag{3.12}$$

the coupling matrix for the right lead is given by

$$\hat{\Gamma^R} = \Gamma \begin{pmatrix} e^{kd_1} & \alpha_{12}\sqrt{e^{kd_1}e^{kd_2}} & \alpha_{13}\sqrt{e^{kd_1}e^{kd_3}} \\ \alpha_{12}\sqrt{e^{kd_1}e^{kd_2}} & e^{kd_2} & \alpha_{23}\sqrt{e^{kd_2}e^{kd_3}} \\ \alpha_{13}\sqrt{e^{kd_1}e^{kd_3}} & \alpha_{23}\sqrt{e^{kd_2}e^{kd_3}} & e^{kd_3} \end{pmatrix} \tag{3.13}$$

To simulate realistic, imperfect barrier well interfaces we use a Gaussian potential for the impurity clusters. As the impurity clusters are assumed to be circular, in the three dimensional parameter space of the potential the trap potentials look like inverted Mexican hats (see Fig. 3.1). The trap potential is modelled as

$$V(\mathbf{r}) = \sum_{i=1}^{3} V_{i,0} e^{-(\frac{\mathbf{r}-\mathbf{r}_i}{d_i})^2} \tag{3.14}$$

where the constant $V_{i,0}$ represents the magnitude of the i-th impurity potential. The potential was separated into harmonic and non-harmonic parts [62]. We consider low level s-states for the clusters which were approximated as Fock-Darwin states. It was shown that a Gaussian potential can be represented around its centre as a sum of the harmonic potential plus a small an-harmonic potential. The coupling between the clusters due to the direct overlap is evaluated by $V_{ij} = \langle \psi_i | \, V_i(\mathbf{r}) + V_j(\mathbf{r}) \, | \psi_j \rangle$. We considered identical clusters therefore $V_{i,0} = V$ and $R_i = R$ where R is the radius of the impurity. The final expression for the matrix elements t_{ij} of the matrix $\hat{V}$ is

$$t_{ij} = -\frac{VR^2}{a^2 + R^2} \mathrm{Exp}\left[\left(d_{ij}^2\right)/(4a^2) \right) \left((2a^2 + R^2)/(a^2 + R^2) \right) \Big] \tag{3.15}$$

where d_{ij} is the inter-cluster separation and a is given by $a = \left(R\hbar/(2mV)^{1/2} \right)^{1/2}$ (m is the effective mass) [62].

The DOS is calculated from the imaginary part of $\hat{S}$, $g(E) = -Im[Tr \sum \hat{S}]$. The carrier lifetime is related to the inverse of the width of the DOS peaks. Finally the $I - V$ characteristics are calculated using $I = q^{-1} \int dE G(E)(f_L - f_R)$ where $f_{L(R)}$ is the Fermi Dirac

distribution with the appropriate chemical potential for the lead and q is the elementary charge.

3.3 Results and Discussion

Horizontal Configuration

DOS spectra of the horizontal configuration (see Fig. 3.2) show two peaks corresponding to two quasi-bound states: one is broad corresponding to the shorter-lived bonding state while the other is sharper corresponding to the longer-lived anti-bonding state. The full width at half maximum (FWHM) of the DOS peaks was plotted as a function of a scaling factor defined as the ratio of the inter-cluster separation to the cluster size (see Fig. 3.2). As the inter-cluster separation increases in the horizontal direction, the lifetime of the anti-bonding state increases as the sharper peak shifts to lower energies and the FWHM of the peak decreases (while the amplitude increases). The bonding (weakly localized) state becomes less localized as the FWHM increases while the amplitude correspondingly decreases, also shown in Figure 3.2. It is evident that while the localization of one state increases, the localization of the other state decreases.

DOS spectra were also studied under varying cluster size (see Fig. 3.3). The lead-cluster coupling matrices $\Gamma^{L,R}$ are directly related to the inter-cluster distance, as is the direct overlap matrix $\hat{V}$. However, the alteration of the cluster size changes only the direct overlap matrix $\hat{V}$. As the cluster size increases, the FWHM of the narrower peak (corresponding to the anti-bonding state) increases indicating that the lifetime of the anti-bonding state decreases (Fig. 3.3). This is to be expected as increasing the cluster-size increases the overlap and therefore the direct tunnelling between the clusters. However, the bonding state (the broader DOS peak) is insensitive to changes in the cluster size, in contrast to the vertical and triangular configurations. This shows that the bonding state is independent of the direct overlap between the clusters. In the horizontal configuration there is only one conduction channel, therefore the lead-cluster coupling interferes with the direct inter-cluster overlap. For this reason, the broader DOS peak is invariant under increasing cluster size. Changing the cluster size has a significantly smaller effect on the DOS spectra than changing the inter-cluster distance. The origin lies with the positive exponential dependence of the right lead-dot coupling matrix Γ^{R}.

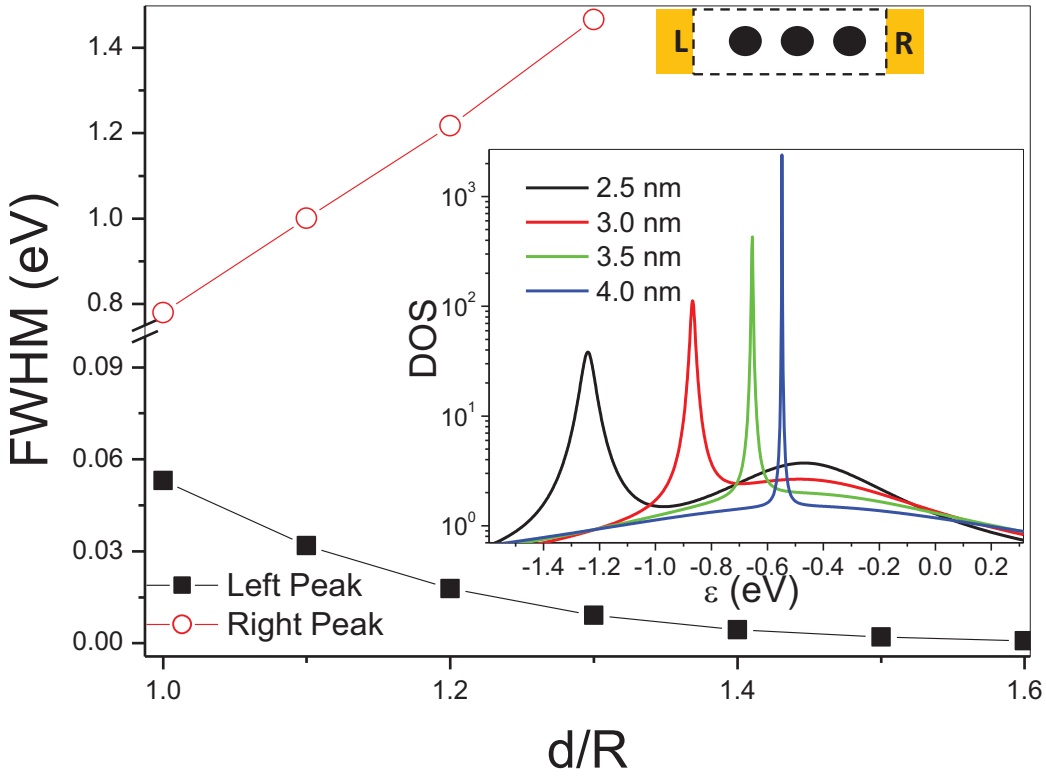


Figure 3.2: FWHM for the horizontal configuration with changing inter-cluster separation as a function of the scaling factor d/R defined as the ratio of inter-cluster separation to cluster size. Inset are the corresponding DOS spectra, for inter-cluster separations ranging from 2.5 to 4 nm, as a function of $\epsilon = E_F - E$ (for all figures).

The wavevector k has a dramatic effect on the DOS peaks. When the wavevector is very small, there is an intense, sharp peak in the DOS at the E_F and a broader peak below the E_F. If k is increased the amplitude (FWHM) of the sharp peak decreases (increases) rapidly indicating that the lifetime of the anti-bonding state decreases while the peak remains close to E_F. A similar but far less rapid decrease is observed with the broader peak although this peak shifts towards the Fermi energy. Physically, k, as the evanescent parameter, influences constructive and destructive interference and therefore variations of k change the degree of localization of a state. The potential V controls the separation between the DOS peaks, the higher the potential the larger the separation.

In the horizontal configuration the single conduction mode maximizes Bragg reflection resulting in the formation of a quasi-bound state inside the continuum (i.e. at energies

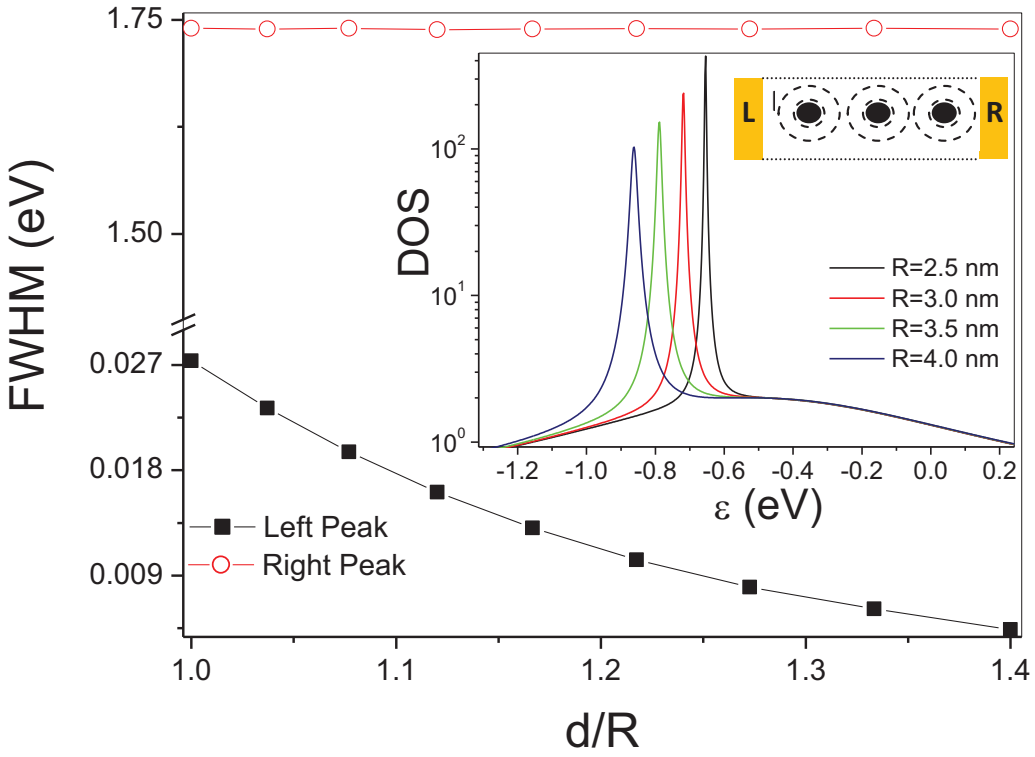


Figure 3.3: FWHM for the horizontal configuration with changing inter-cluster size, from 2.5 to 4 nm, as a function of the scaling factor d/R. Inset are the corresponding DOS spectra as a function of ϵ.

greater than the trap depth). The conductance spectra therefore show a prominent Fano resonance as a result of interference between this longer lived state and the continuum. The energy of the minimum of the Fano resonance coincides with the energy of the maximum of the anti-bonding state of the DOS (see Fig. 3.4). There is another minimum in the conductance spectra which corresponds to the energy of the bonding state. As the inter-cluster separation increases, the Fano resonance peak migrates to lower energies while the amplitude of the maximum (in-between the minima) decreases. This amplitude is closely associated with the prominent NDR observed in the $I-V$ curves shown in Figure 3.4. Secondary features can also be induced depending on the system parameters. Figure 3.5 shows the peak to valley ratio (PVR) of the $I-V$ curves as a function of the FWHM of the left and right DOS peaks. In fact the PVR increases as the inter-cluster separation increases although the amplitude of the current decreases as the feature shifts to lower potential. There is therefore a limit to the maximum possible PVR for practical applications given by

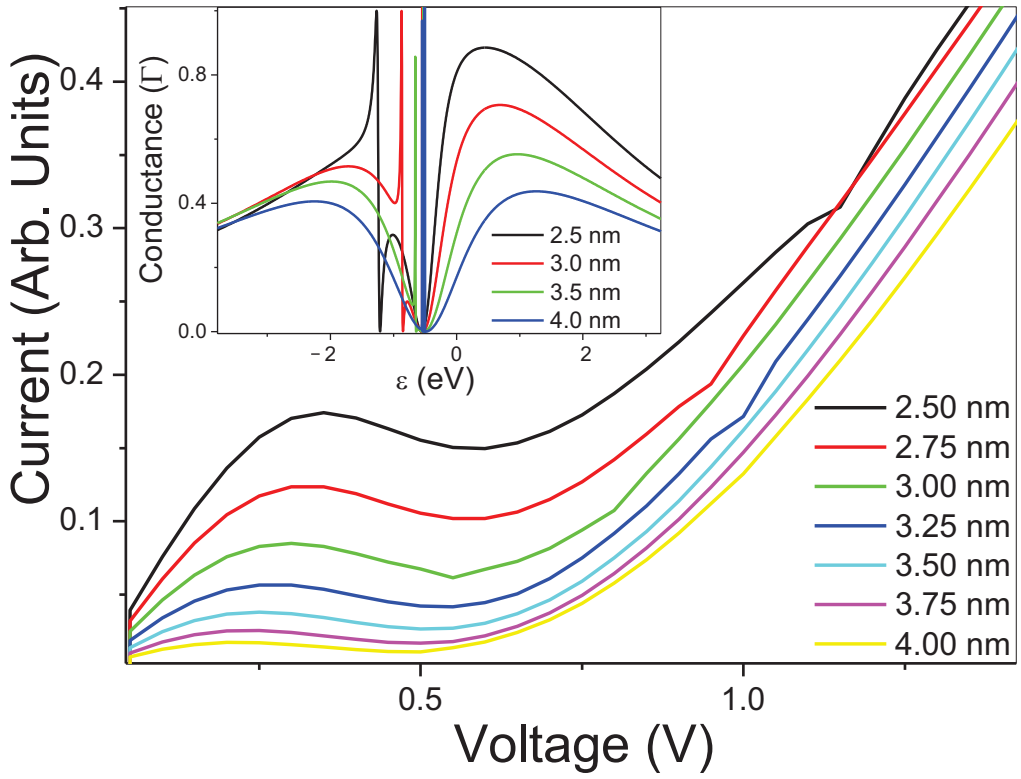


Figure 3.4: $I-V$ curves for the horizontal configuration with changing inter-cluster separation, from 2.5 to 4 nm. Inset: the corresponding conductance spectra as a function of ϵ.

the noise floor of the measurement system.

Vertical Configuration

Under rotation from the horizontal to the vertical configuration, the lifetime of both states increases as constructive interference diminishes as shown in Figure 3.6. The anti-bonding state shows cosine dependence however the dependence of the bonding state is unusual, displaying a maximum at 45 degrees (i.e. maximum non-resonant transmission). As the system rotates towards the vertical the Fano resonance becomes less sharp and shifts to slightly lower energies (see Fig. 3.6).

In the vertical configuration, changes in the wavevector affect the DOS similarly to the horizontal configuration. The DOS spectra for the vertical configuration for the same wavevector

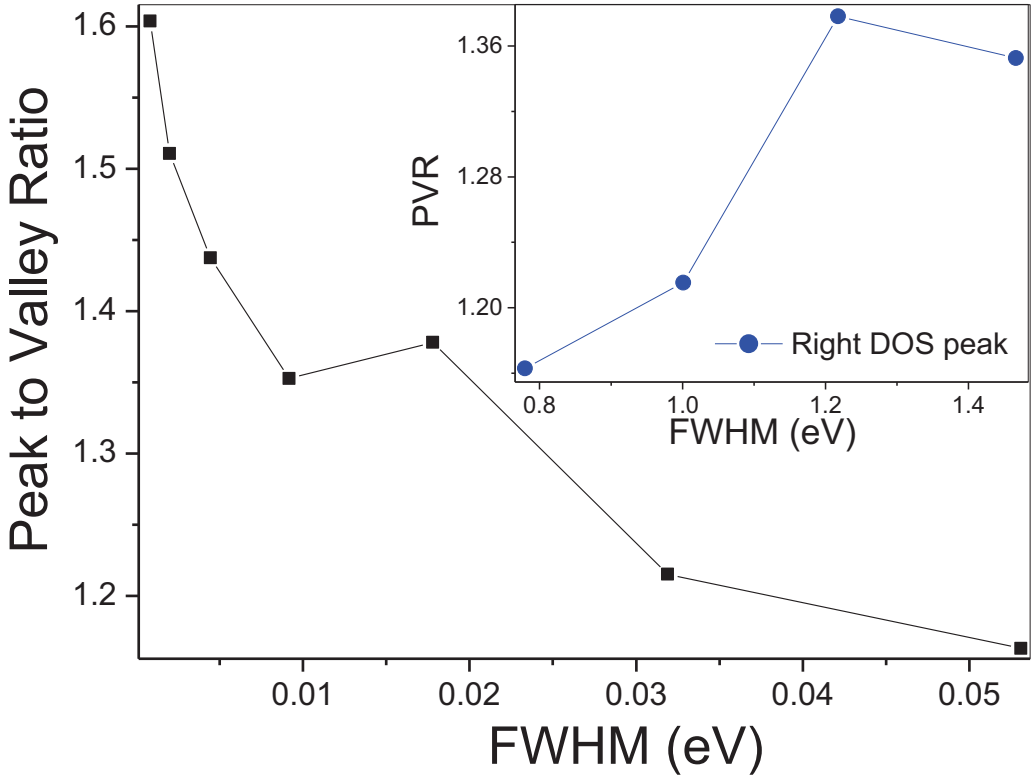


Figure 3.5: Peak to valley ratio of the resonant tunnelling feature as a function of the FWHM of the left (narrow) DOS peak. Inset: The corresponding curve as a function of the right (broad) DOS peak FWHM.

as the horizontal configuration, show two merged peaks which are the superposition of two Lorentzians (see Fig. 3.7). The amplitude of the broader peak in the vertical configuration is slightly less than the corresponding peak in the horizontal configuration. This is the result of the decrease of the coupling factor α as the inter-cluster spacing in the vertical direction is non-zero.

Under the simulated increase of the inter-cluster distance in the vertical direction, the FWHM of the narrow peak increases (the lifetime of the anti-bonding state decreases) while the FWHM of the broad peak decreases as shown in Figure 3.8. In this configuration the FWHM as a function of the geometrical factor d/R undergoes oscillations. This is reflected by the Bessel function dependence of the coupling factor α, which is extremely sensitive to changes in the vertical separation − changes in the vertical separation result in relative phase changes between electrons travelling through the different channels (this also explains the unusual behavior of the FWHM of the bonding state in the transition from

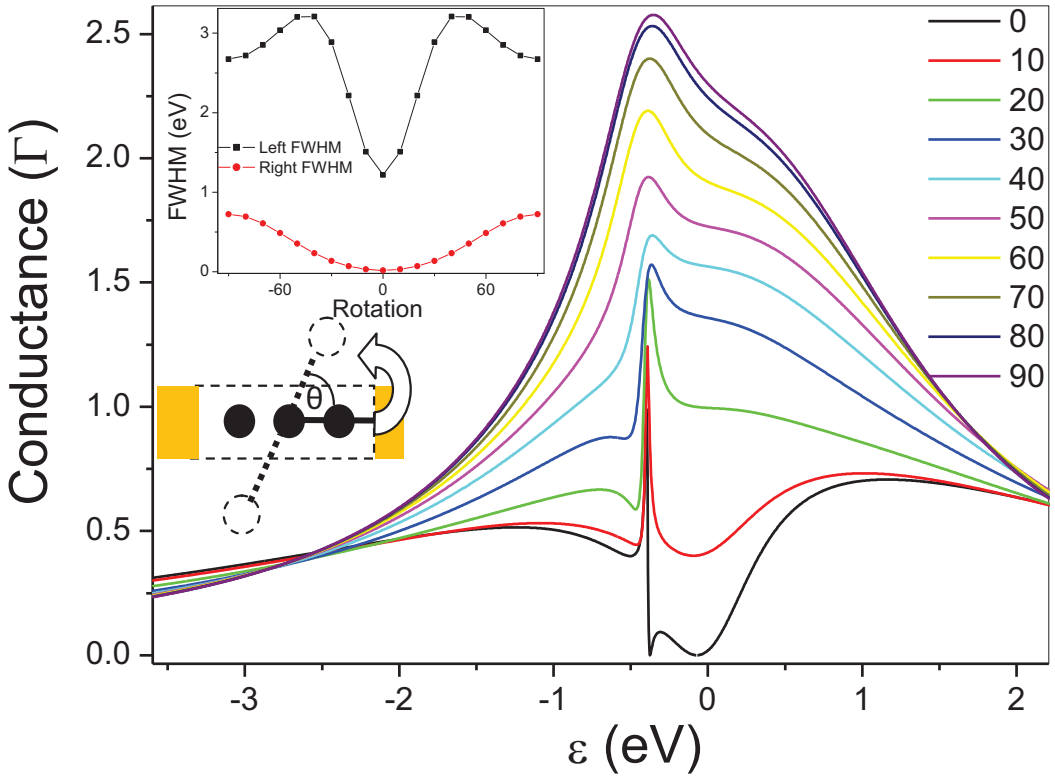


Figure 3.6: Conductance spectra as the horizontal configuration is rotated to the vertical configuration, each curve corresponds to a different angle measured from the horizontal. Inset is the FWHM of the corresponding DOS spectra as a function of the rotation angle from the horizontal.

horizontal to vertical). This changes the degree of constructive or destructive interference and consequently the lifetime of the state. As the separation between the clusters in the vertical direction increases, the DOS peaks merge into a single Lorentzian. The corresponding $I-V$ curves, shown in Figure 3.8, do not show resonant tunnelling features due to the absence of a strongly localized state.

Under increasing cluster size, the FWHM of both of the peaks in the DOS spectra increases monotonically (not shown). The bonding and anti-bonding states are therefore both influenced by the direct overlap in the vertical configuration – with increased coupling the lifetime of both states decreases. As the direct overlap increases, transport via the multiple conduction channels increases therefore the lifetime of the quasi-bound state decreases. However, the matrix elements of the lead-cluster coupling between the first and third clusters are significantly smaller than the matrix elements of adjacent clusters so the direct

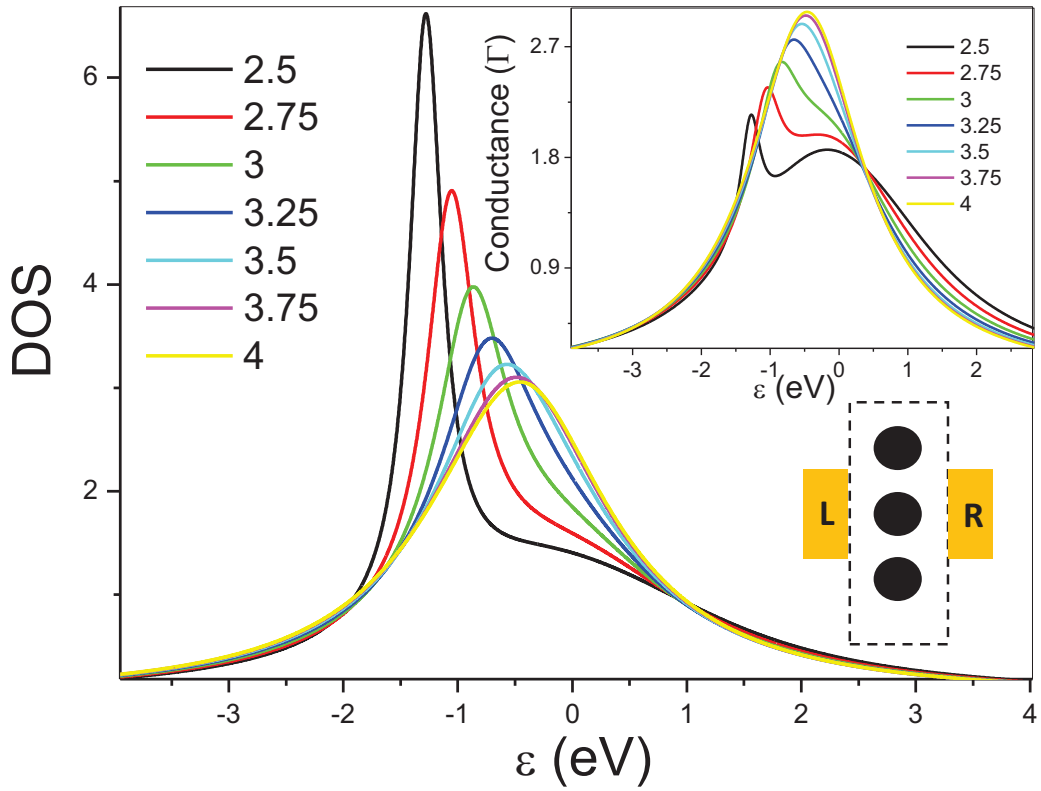


Figure 3.7: DOS spectra in the vertical configuration with changing inter-cluster separation, from 2.5 to 4 nm, as a function of ϵ. Inset are the corresponding conductance spectra as a function of ϵ.

overlap is insignificant. A feature common to the DOS curves in both configurations is that as the inter-cluster separation increases the sharper peak shifts to lower energies while in contrast as the cluster size increases the sharper peak shifts to higher energies. In the triangular configuration, the single DOS peak also migrates to higher energies as the dot size is increased.

Triangular Configuration

Apart from the idealized horizontal configuration arbitrary cluster arrangements were investigated in the form of triangular cluster configurations for implementation in materials where the arrangement of impurity clusters may not be precisely controlled. Initially we consider vertical symmetry-breaking in the horizontal configuration by shifting one of the quantum dots in the vertical direction. We find that the lifetime of both quasi-bound states decreases

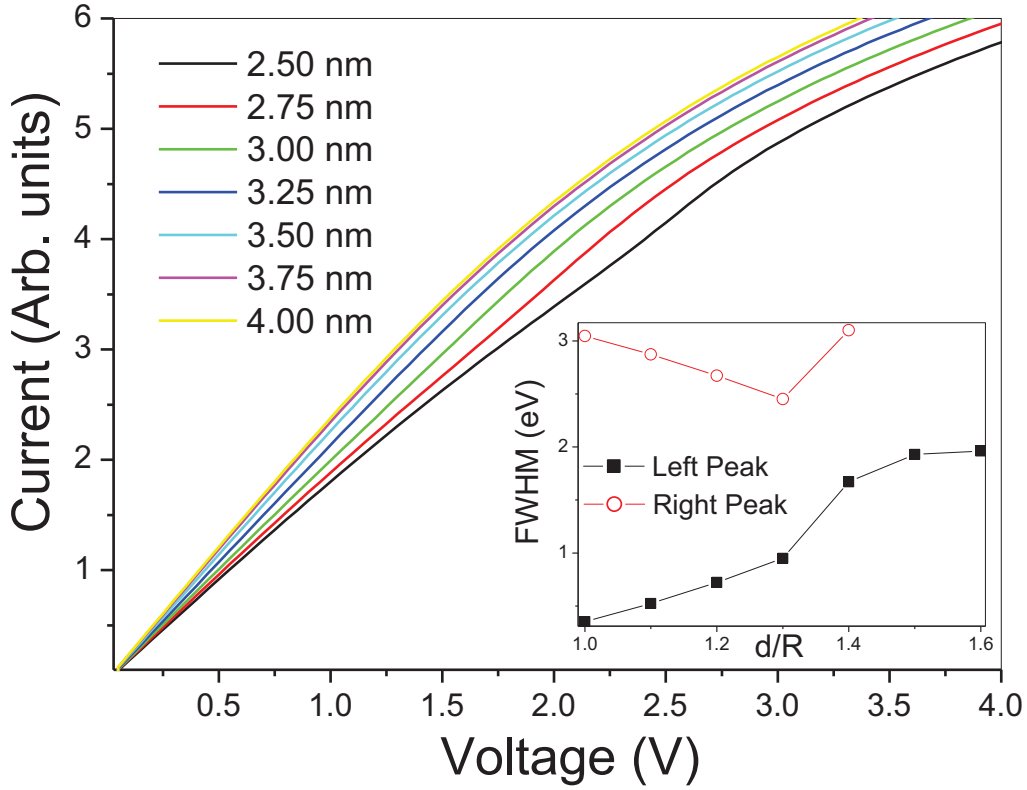


Figure 3.8: $I-V$ curves for the vertical configuration with increasing vertical inter-cluster separation, from 2.5 to 4 nm. The FWHM of the corresponding DOS spectra as a function of the scaling factor d/R is inset.

(Fig. 3.9) as the constructive interference is reduced. The minima in the conductance spectra shift from zero to higher conductance, as shown in Figure 3.9. Furthermore, the inset in Figure 3.9 shows that the lifetime of the bonding and anti-bonding states decreases as the FWHM of both DOS peaks increases. The peak to valley ratio of the resonant peak in the $I-V$ curves correspondingly decreases.

Additionally an equilateral triangular configuration was studied with changes in the inter-cluster distance maintaining an equilateral triangle i.e. the horizontal and vertical components are changed simultaneously when the inter-cluster distance is varied. We find that two relatively short-lived bonding and anti-bonding states are still formed, one with a longer lifetime than the other, while the formation of strongly localized states is prohibited. Using the same wavevector as in the vertical and horizontal configurations, the DOS is a superposition of two Lorentzians although their separation is very small as shown in Figure 3.10. However, changing k has a very small effect in the triangular configuration as there is mini-

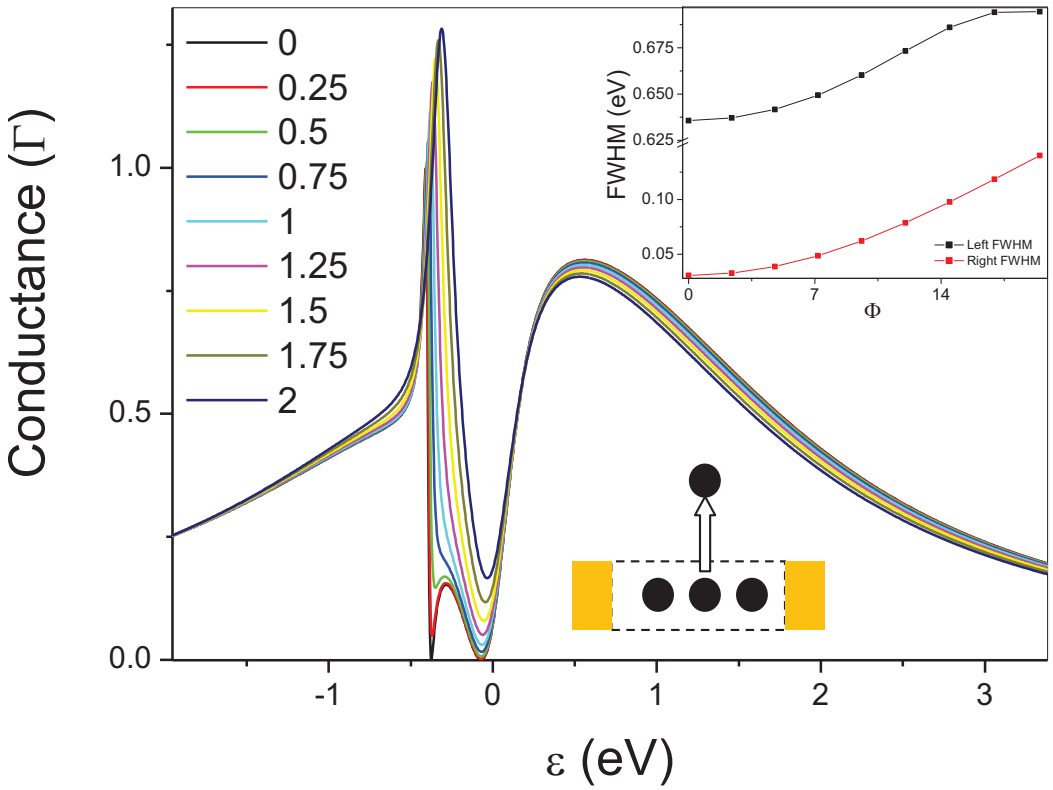


Figure 3.9: Conductance spectra as the central cluster is shifted vertically from the horizontal where each curve corresponds to a different vertical separation of the central cluster measured from the horizontal plane of the outer clusters, ranging from 0 to 2 nm. Inset is the FWHM of the DOS peaks as a function of the angle between the outer clusters and the central cluster.

mal constructive interference. The formation of strongly localized states is inhibited as the inter-cluster distance is the same between all three clusters so electrons can"bypass" confinement as the transition probability from one cluster to the other two clusters is the same. The $I-V$ curves therefore show no resonant tunnelling features as illustrated in Figure 3.11.

Under increasing inter-cluster distance the FWHM of the longer lived state increases (as in the vertical configuration) while the FWHM of the shorted lived state increases initially (as in the horizontal configuration) then decreases abruptly (Fig. 3.11) where the change may be ascribed to the Bessel function dependence in the vertical inter-cluster distance. The FWHM therefore shows trends related to both the horizontal and vertical configurations. When the cluster size is increased, the FWHM of both peaks increases, in agreement with the vertical and horizontal configurations. This reflects the slight increase in the direct overlap between

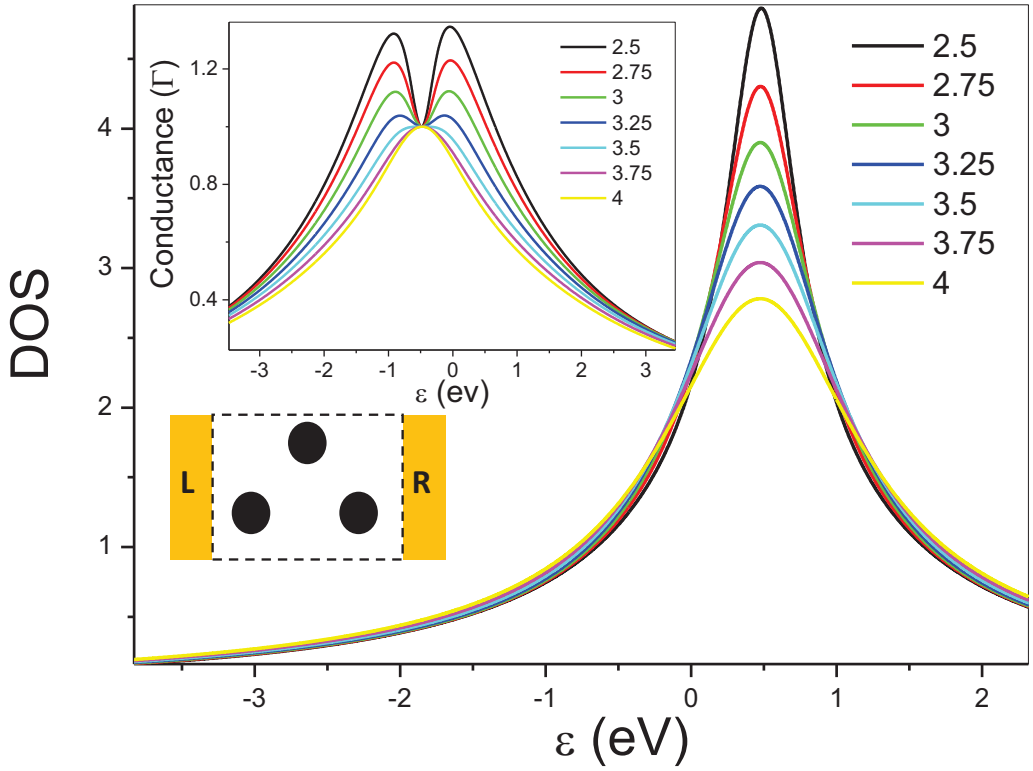


Figure 3.10: DOS spectra in the triangular configuration (equilateral) with increasing uniform inter-cluster separation from 2.5 nm to 4 nm. The corresponding conductance spectra are inset.

the clusters, reducing the lifetime of both states.

It is well known that a random distribution of point defects produces hopping conduction, which is an inherent property of a disordered system [135, 136]. We attempt to extend our analysis to interpret some asymmetric configurations as a study of disordered systems. If the inter-cluster separation is non-uniform, the DOS spectra, showing a single prominent peak, are in fact the superposition of three Lorentzians rather than two (not shown here). We find a longer lived state and two shorter lived states. In symmetric triangular configurations, there is only one short-lived state but when the coupling between all three clusters in different, the quasi-bound states are found at different energies, separating out the short-lived states. Consequently the FWHM of each Lorentzian is different although the two short-lived states are found at almost the same energy with significant overlap. The loss of symmetry, both horizontal and vertical, therefore effectively separates out the conduction channels. This analysis suggests that even in the non-ideal case, useful devices can still be engineered based

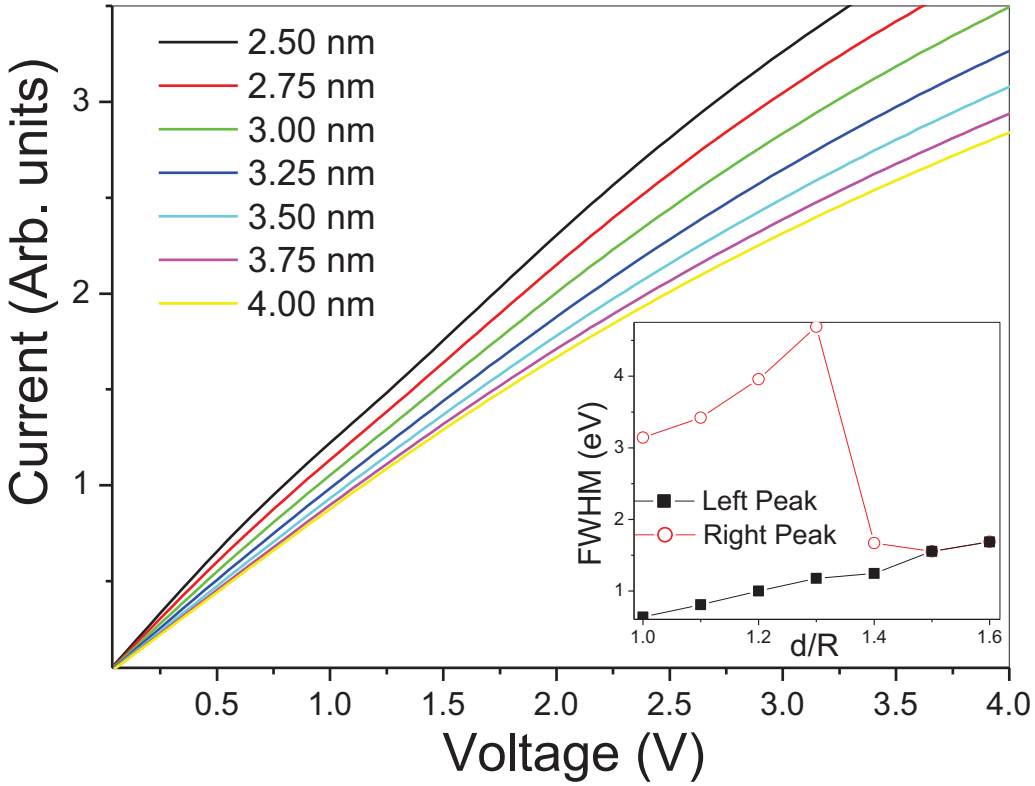


Figure 3.11: I-V curves for the triangular configuration (equilateral) with increasing inter-cluster separation, from 2.5 to 4 nm. The FWHM of the corresponding DOS spectra as a function of the scaling factor d/R is inset.

on the short trapping time of the disordered configuration.

3.4 Conclusion

By employing the Shahbazyan-Raikh model with a modified Gaussian cluster potential strong resonant levels are demonstrated based on the coupling between impurity centres [57]. The Gaussian potential represents weak disorder as would be expected in devices. The effect of geometrical variations on the direct overlap matrix was also investigated, allowing for comparisons between the direct coupling and indirect coupling through the leads. We highlight the horizontal configuration which enhances constructive quantum interference effects and produces the most prominent negative differential conductance in the $I-V$ spectra. However even the vertical and triangular configurations can show step-like features indicating

that the trapping time of the bonding and anti-bonding states can be controlled effectively.

The representation of the potential in a Gaussian form is applicable to weakly disordered systems where sharp discontinuities might not be possible so this study can be extended to disordered systems. The triangular configuration was studied as it represents a disordered system, albeit symmetric. The triangular configuration does not show prominent NDR features, although it can show step-like features when the correct parameters are chosen. The single channel horizontal configuration is conducive to constructive quantum interference and consequently shows a strong NDR peak. The prominent Fano resonance relies on the interference between a bound state formed at energies greater than the trap depth and the continuum. Bound states in the continuum are most easily formed in the horizontal configuration due to Bragg reflection at the interface between the high and low potentials, in spite of the Gaussian profile of the potentials.

Constructive interference can also occur in the vertical configuration although this occurs at smaller wavevectors than in the horizontal configuration i.e. NDR could only be achieved in ordered material or very weakly disordered materials. The potential involved in the direct overlap between the clusters strongly influences the Fano resonance as it decreases, the Fano resonance shifts towards the Fermi energy and the magnitude diminishes. The Fano resonance therefore relies on the direct coupling between the clusters as well as the coupling through the leads. Quantum interference phenomena were found to be strongly influenced by the wavevector k. The wavevector determines the number of peaks in the DOS (and conductance) which can be tuned from one peak to three peaks. As k determines the rate of decay of the evanescent modes it controls the degree of constructive and destructive interference. Furthermore, the formation of bound states in the continuum has been shown to be dependent on the wavevector. We have investigated two different values for the wavevector the first was to compare with the earlier study on a double-dot system by Shahbazyan and Raikh while the second was chosen to maximise the peak to valley ratio in the $I-V$ curves [57]. In addition to the Lorentzian line shapes for (symmetric wave functions) Fano resonance peaks (for anti-symmetric wavefunctions) can be seen in the conductance spectrum. However, Fano resonance peaks can be suppressed by adjusting the coupling between the defect centres for $\alpha \neq 1$.

The triangular configuration disrupts constructive interference preventing NDR. If the triangle is rotated (not shown here), the FWHM of the strongly localized state increases while the FWHM of the weakly localized state decreases. This related to the change in

constructive interference as the triangle rotates. In this configuration the direct overlap between all three clusters is the same, therefore there is no preferred conduction channel so constructive interference cannot be maintained. In the horizontal configuration, breaking the symmetry by shifting one of the quantum clusters in the vertical direction decreases the NDR peak. As the asymmetry of the array increases, the constructive interference decreases so the strongly localized state becomes weakly localized.

Chapter 4

Experimental Procedures

4.1 Sample Preparation

Reduced graphene oxide (RGO) samples were provided by Messai Mamo. Graphite oxide was prepared as in previous studies, beginning with natural graphite powder, using the modified Hummers method [137]. A procedure for the reduction of graphene oxide (GO) was adopted from Fernandez-Merino *et al.* [69]. The critical process was reduction with ascorbic acid as opposed to the conventional hydrazine reduction.

GO has a great deal of epoxy, hydroxyl, carboxyl and carbonyl groups attached to the sheets. Therefore, sheets of GO and RGO can be stably dispersed in water to form colloidal dispersions. GO and RGO devices were manufactured across a pair of rectangular gold micro-electrodes with a gap of approximately 1 μm. Dielectrophoresis (DEP) was used to align GO/RGO sheets by dropping a fraction of a μl of ultrasonicated GO/RGO in suspension in water across the gap in the micro-electrodes using a micro-pipette while an alternating current of 10 V_{p-p} at 2 MHz was applied across the electrodes using a home-made micro-manipulated probe station. DEP is the process whereby a dipole moment is induced materials in suspension using an electromagnetic field. In the present study, DEP induces a dipole moment in GO/RGO so the sheets align with the applied magnetic field. Devices showed no sign of a Schottky barrier and proved to be robust.

4.2 Transport Measurements

To perform transport measurements, a number of different micro-structures were designed within the Nano-scale Transport Physics Laboratory. Devices composed of tungsten overlaid with gold (approximately 100 nm thick) on a quartz substrate were fabricated using standard lithographic techniques at the Carl and Emily Fuchs Institute for Microelectronics (CEFIM). Waveguides designed for high frequency operation in the ground-source-ground configuration (with a gap of approximately 1 μm) were used to perform two-probe DC transport measurements as the electrode structure was well suited to dimensions of the GO/RGO sheets.

Two terminal current-voltage ($I-V$) measurements were performed under high vacuum in a Janis free flow cryogenic micro-manipulated probe station. The system was evacuated using an Edwards turbo-molecular pump down to approximately 10^{-6} $torr$ at room temperature overnight. The sample heater was then set to room temperature while cryogen was circulated through coils (isolated from the vacuum) surrounding the sample stage. This promotes the removal of atmospheric adsorbate from the GO/RGO surface and ensures that any condensation from residual moisture within the chamber does not condense on the GO/RGO surface. The reduction in temperature as the cryogen circulated through coils within the chamber facilitated cryo-pumping down to a base pressure of approximately 10^{-8} $torr$ which was maintained throughout the experiment. The sample mount inside the cryostat is also shielded from radiation with a platinum radiation shield. A thin layer of thermally conductive grease was used to ensure sufficiently rapid transfer of thermal energy applied to the sample mount (chuck). The sample temperature was controlled with a Lakeshore 336 Temperature Controller. The micro-manipulated probes are manufactured from tungsten due to its high electrical conductivity and the probe assembly is engineered for high accuracy low noise measurements. The entire assembly rests on a passive pneumatic vibration isolation table which protects devices and probe tips as the probes are manoeuvred into position to make contact with the micro-structure.

The electrical properties were analysed using an Agilent Semiconductor Device Analyser. The analyser combines source monitor units and allows for the application and measurement of bias and current. The system is designed for low current measurements with a resolution of approximated 1 pA in the two-probe configuration. Current voltage sweeps were programmed within Agilent's custom software. The potential was varied from -2 V to 2

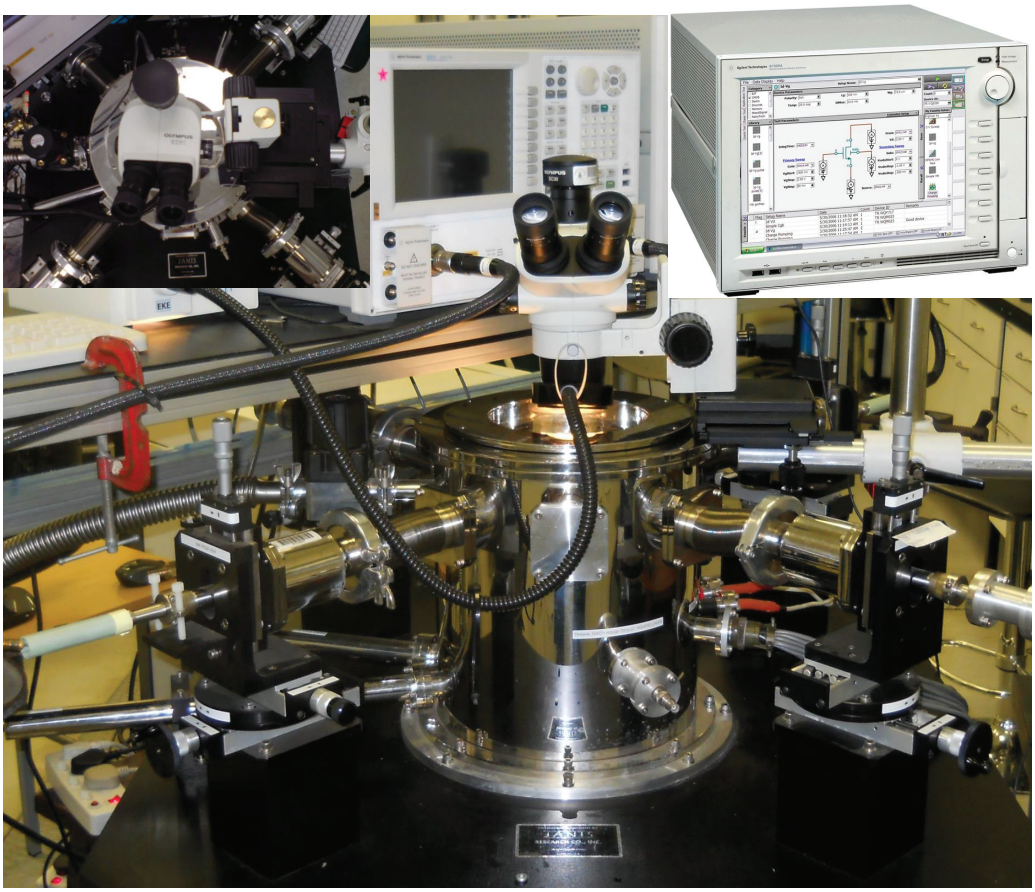


Figure 4.1: Janis micromanipulated probe station. Upper left inset: Viewed from above. Upper right inset: Agilent B1500A Semiconductor Device Analyser.

V while the current was recorded. The semiconductor device analyser has been interfaced with the temperature controller via GPIB so that the temperature can be controlled and recorded while simultaneously recording $I-V$ measurements. A sequence was programmed to automate the reading of $I-V$ measurements with temperature. The resistance is then available over a wide range of potentials which aids in interpretation of the transport properties. Concurrently, the flow of cryogen was carefully controlled by adjusting the pressure of the dewar and the flow valve of the transfer line. Although the temperature controller was programmed for maximum stability within the Agilent software, the temperature stability was constantly monitored and the cryogen flow adjusted accordingly to ensure accuracy during the duration of each $I-V$ measurement.

Four probe transport measurements were performed using a cryogenic free measurement

system of Cryogenic Ltd. design. The system relies on two closed refrigeration cycles. A compressor (cooled by an external chiller) cools helium gas to 40 K in the first stage relying on the rapid expansion of helium gas to reduce thermal energy. In the second stage, helium gas at 40 K is injected into an evacuated cryostat and driven by an external oil-free pump. The helium gas is further cooled to 4 K where is condenses to the liquid phase. In the second stage, excess thermal energy is dissipated in an external helium dump. Inside the cryostat, liquid helium is collected and further cooled to approximately 2 K by decreasing the vapour pressure using a sorption pump while the flow is controlled using a needle valve. This cooled helium is then circulated around the sample chamber, which is referred to as the variable temperature insert (VTI). The VTI is in thermal contact with the circulating cryogen while it is otherwise isolated. A vacuum is therefore created inside the VTI before the sample is lowered into the VTI.

Samples were mounted on probes which were lowered into the VTI. At the top of the VTI, a series of O-rings allows a vacuum to be maintained within the VTI while the probe is lowered into the VTI. The upper section of the VTI (isolated using a gate valve) was flushed with helium gas, then evacuated with a rotary pump and the process was repeated for at least 5 minutes to ensure that any residual gas in the VTI would be a small amount of helium. After the final flush with helium gas, the VTI was evacuated, the gate valve was opened and the probe was lowered while the rotary pump maintained the vacuum.

Transport measurements were performed using a Keithly 2400 to source current and a Keithly 2182A nano-voltmeter to measure voltage in the four probe configuration. The K2400 and K2182A were connected to a Keithly matrix scanner and the scanner was connected to the probe via a 16-pin connector. RGO devices were manufactured across a custom designed gold Hall bar with a gap of approximately 1 μm using dielectrophoresis in the van der Pauw configuration. The micro-electrodes were then connected to the probe using silver conductive paste under an optical microscope. A source current of 10 μA was used after investigating currents from 1 μA to 20 μA as it was low enough to protect the sample from damage while also providing a high enough current to increase the signal to noise ratio.

The sample temperature was controlled using a Lakeshore 336 temperature controller. The cryogenic system is controlled using Labview software which controls the temperature and Hall measurement systems (K2400 and K2182A) simultaneously and measurements were automated by programming sequences to control the virtual instruments within the Labview software. Resistance versus temperature measurements were recorded from 2 K to room

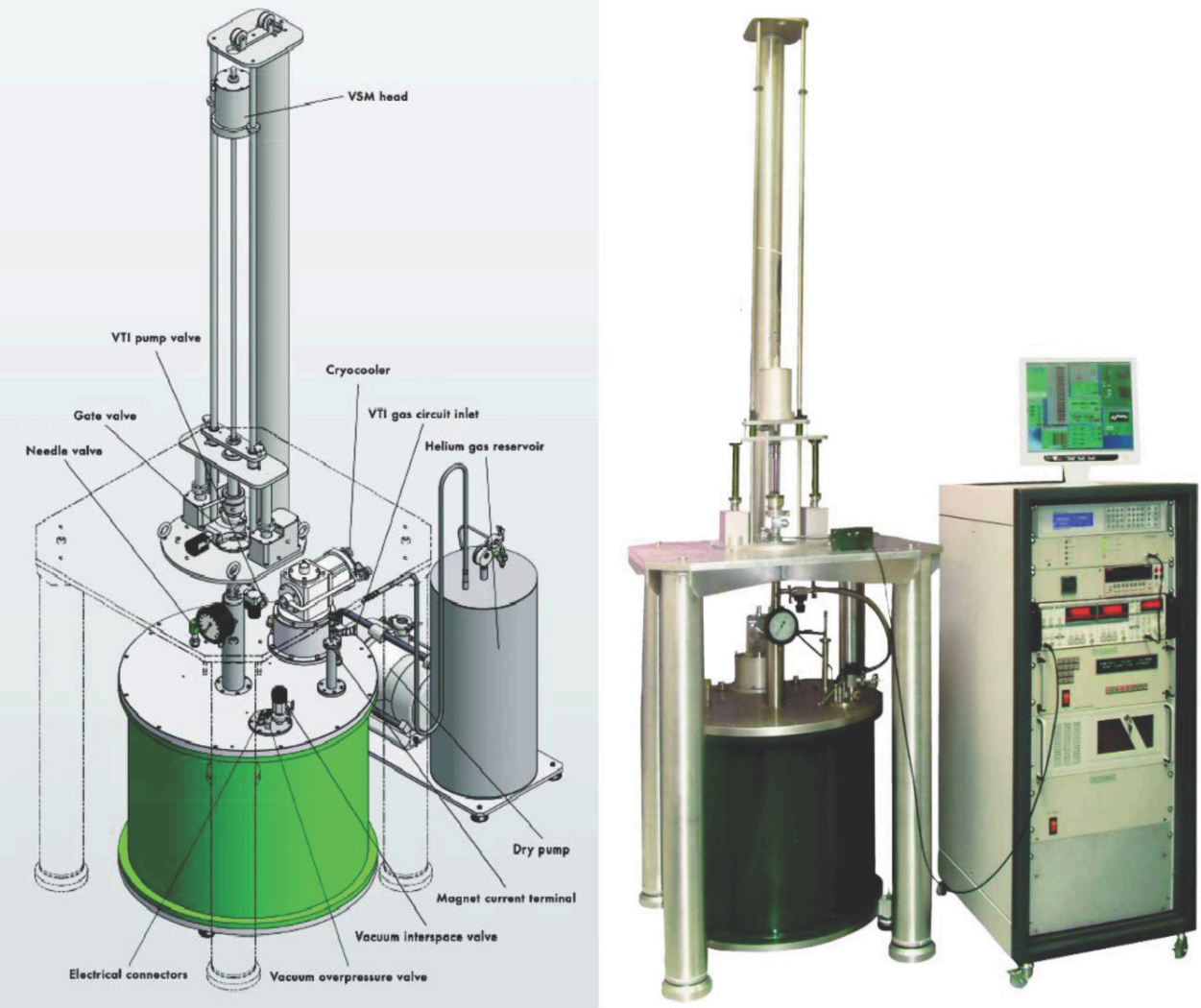


Figure 4.2: Cryogenic free measurement system.

temperature while magneto-resistance measurements were performed up to 12 T using a superconducting magnet (power supply also provided by Lakeshore).

Chapter 5

Electronic and Magnetic Properties of Reduced Graphene Oxide

In Chapter 2 we studied the electronic properties of graphene and bilayer graphene chemically modified through the incorporation nitrogen impurities which do not form clusters as a result of recombination to N_2. Experimentally it is difficult to incorporate nitrogen while impurity clusters have a more significant effect on the transport properties and offer greater control of quantum transport features as demonstrated in Chapter 3. In this chapter we present an experimental study of the electronic transport properties of reduced graphene oxide (RGO) which, as illustrated through previous studies, consists of intact graphene nano-islands embedded within residual functionalized regions. As mentioned in Chapter 3, this is effectively a disordered quantum dot system. The chemical synthesis is well suited to mass production of graphene. We demonstrate semi-metallic transport in graphene oxide layers treated with an organic acid through a nearly linear current vs. voltage relationship and the weak temperature dependence of resistance from high temperatures down to 20 K. Additionally an energy gap was observed below 17 K due to the formation of local barriers by residual oxygen groups and disorder in reduced graphene oxide (RGO) sheets. At higher temperatures resistance shows a negative T^2 temperature dependence. These results show evidence of the decay of the magnitude of mesoscopic resistance fluctuations and well as prominent effects of elastic scattering associated with graphene, as discussed in Chapter 1. Temperature dependent magnetization measurements showed a phase transition from diamagnetic to ferromagnetic at around 10 K, in agreement with the electronic transport properties of the RGO films.

5.1 Introduction

5.1.1 Mesoscopic Resistance Fluctuations and Carrier Scattering in Graphene

Mesoscopic resistance fluctuations (MRF's), closely related to universal conductance fluctuations (UCF's), have been widely studied in graphene. These effects originate with the band structure of graphene [38] which contributes to the prominent role of elastic scattering processes [36] in spite of dephasing due to inelastic scattering. Graphene-specific treatments of UCF's consider a 4 component spinor, indexed not only by the sublattice but also by the two inequivalent points in the Brillouin zone where the conduction and valence bands meet, the K and K' points. This approach highlights the role of inter-valley and intra-valley scattering. A Hamiltonian is developed which has symmetries of chirality and time-reversal symmetry. Disorder, introduced through an additive term to the Hamiltonian, destroys translational and rotational symmetry and may break the chiral and time-reversal symmetries [38].

If long range disorder is considered, with the disorder varying smoothly over a length-scale greater than the lattice constant, then little scattering from the K to the K' points is expected. In addition, the chirality of charge carriers acts to suppress inter-valley scattering. This effect is especially prominent close to the charge neutrality point where impurities result in charge"puddles" [31]. Weak localization is therefore suppressed in favour of UCF's. In the extreme case, this may result in weak anti-localization. Shifts of the Dirac point from E_F can break chiral symmetry. In conjunction with short-range disorder (induced by, for example charge neutral impurities), strong localization effects can occur. Short-range disorder can induce inter-valley scattering while preserving time-reversal symmetry, reducing the variance of the conductance and promoting weak localization.

A number of experimental studies of resistance as a function of gate voltage, magnetic field and temperature have been performed to illuminate the nature of MRF's in graphene. The decay of the amplitude of MRF's with temperature in conventional, disordered metals follows an inverse power law [138]. Such a dependence has been observed in heavily doped graphene [139]. As illustrated in Chapter 2 with N doping, doping of graphene can induce metallicity. However, other studies of undoped graphene have found an anomalous exponential decay with temperature (confirmed by the MRF amplitude as a function of gate voltage at constant temperature) which has not yet been fully understood [30, 31, 140].

In these studies, the behaviour of the resistance as a function of temperature was investigated at different gate voltages, which were used to tune the MRF amplitude from constructive to destructive. It was found that the behaviour of the resistance with temperature is entirely different depending on whether the interference is constructive or destructive. Sample widths between 1.2 μm and 1.5 μm were investigated. It was also noted in these studies that at high temperatures, impurities may become mobile (as discussed in Chapter 2) which also influences MRF's so when the temperature was varied from low to high (above 50 K), measurements of the trend of resistance from high temperature to low temperature were found to be different [30]. In another study, a strong super linear increase was found in the resistance as a function of temperature at high gate voltages which was attributed to phonon scattering with a contribution from the substrate (SiO_2)[31].

Carrier scattering from a wide range of sources has been studied extensively in graphene [141, 142]. Considering graphene as a metal which is to some extent disordered (diffusive rather than ballistic) calculations for the resistivity/conductivity are performed within the Boltzmann theory applied to Dirac fermions. One of the notable results of the treatment is that, for scattering from radially symmetric potentials, backscattering is completely suppressed. It was also demonstrated that scattering from short range potentials has little overall effect as a direct result of the quasi-particle treatment of charge carriers as Dirac fermions. In addition it was predicted that the conductivity of rippled graphene would show a (positive) quadratic temperature dependence. When interpreting the electronic properties of RGO, naturally we found deviations from the expected transport mechanisms of graphene although there is some overlap. We have therefore considered some of the ideas developed in the theory of transport in disordered amorphous metals in order to make progress towards understanding electronic transport in RGO.

The unusual transport properties of high resistivity amorphous metals, in particular Ag-Cu-X metallic glasses with X = Mg, Si, Sn, Sb and $Mg_{1-t}Zn_t$ alloys have been studied extensively primarily to gain insight into the nature of transport in disordered materials [143, 144, 145, 146, 147, 148]. Resistance as a function of temperature showed a dependence following $\rho \propto 1+AT^2$ however it was discovered that the temperature coefficient of resistivity (TCR) A could be positive, negative or change from positive to negative with temperature. A correlation between the resistivity of the material and the TCR was also noted (the Mooij correlation). For relatively low resistivity disordered alloys, the TCR is positive while for relatively high resistivity alloys the TCR is negative. Within some intermediate range of

resistivity, a metal-insulator transition might be expected. The fundamental premise of the Ziman theory is that the scattering term of the Boltzmann Transport Equation is extended to include the structure factor which is invoked to determine the scattering probability [146]. Within the Ziman theory, electron scattering from ions is treated quasi-elastically and is described by the static structure factor. The existing Ziman theory at the time could not account for experimental findings and eventually an explanation was developed with an extension to the Ziman theory which could explain the quadratic term for a positive TCR.

The origin of a negative TCR proved to be more elusive. The eventual explanation relied on a postulate (called the interaction postulate) that phonons with wavelengths greater than the electronic mean free path play little role in carrier scattering [145, 146]. The resistivity of the structure factor was then examined. The interaction postulate restricts the summation over reciprocal lattice vectors and a general expression is obtained for temperatures higher than half of the Debye temperature. This treatment explicitly showed that the TCR depends on the resistivity of the material − the TCR is positive for relatively low resistivity samples while the TCR is negative for high resistivity samples in agreement with the Mooij correlation. This theory is often cited in the explanation of temperature dependent metal insulator transitions in simple metallic glasses. Elastic scattering reduces the resistance with increasing temperature due to the temperature dependence of the Debye-Waller factor [143] while the contribution of inelastic scattering increases the resistance with temperature. In high resistivity alloys, where the mean free path is of the order of the inter-atomic spacing, elastic scattering wields great influence and the TCR is negative.

5.1.2 Electronic Transport in Reduced Graphene Oxide

With the ultimate goal of achieving a chemical route to graphene production, graphene oxides have recently received significant attention [149, 150, 151, 152, 153]. Furthermore the possibility of tuning the energy gap has generated keen interest in the fundamental transport properties of functionalized graphenes [154]. The removal of functional groups in GO has been demonstrated with hydrazine reduction however many topological defects are introduced in the reduction process resulting in highly disordered RGO. This provides strong motivation for the investigation of other reducing agents. A recent study revealed that ascorbic acid, which is environmentally friendly, provides an excellent alternative to hydrazine as a large-scale reducing agent [69]. In this Chapter we therefore study the electrical transport

properties and magnetic properties of GO reduced with ascorbic acid. The resulting RGO shows less pronounced localization induced by disorder than GO reduced with hydrazine.

The relatively low electrical conductivity of RGO in comparison to graphene is due to the presence of residual functional groups and disorder in RGO [155, 66]. RGO sheets are composed of pristine graphene regions (in the range of 3-6 nm) intermittently dispersed within highly oxidized regions with yet other regions dominated by topological defects induced in the oxidation-reduction process [63]. Conduction has consequently been attributed to variable range hopping (VRH) [156, 157] occurring from highly conductive intact graphene nano-islands across disordered regions, which present potential barriers to charge carriers, resulting in localization [156, 67, 157]. Deviation from the VRH regime has been reported with a contribution from thermally activated carriers or a field dependent (and temperature independent) term in the conductivity [67, 156].

Joung *et al.* found the conduction mechanism in RGO to be space charge limited with a transition from trap free space charge limited conduction to exponentially distributed trap space charge limited conduction [155]. Subsequently a schematic model was proposed with graphene regions as quantum dots separated by oxidized regions, which act as tunnel barriers. The transport mechanism was found to be Efros-Shklovskii VRH with localization length comparable to the dimensions of the graphene quantum dots [66].In this study, current suppression was also reported at low temperatures below a threshold voltage, indicating a Coulomb blockade of charges.

5.1.3 Magnetic Properties of Reduced Graphene Oxide

With regard to the magnetic properties, several theoretical and experimental studies have focused on magnetism in graphene and graphite [70, 158, 159, 160, 93, 68]. The observation of ferro magnetism in graphene and graphene based materials has not yet been fully understood [70]. A number of theoretical works have suggested that edge effects play an important role in ferromagnetism, with defects and vacancies also contributing [68, 160, 93]. However the stability of local moment formation of graphene edge states is questionable at higher temperatures. Zhou *et al.* have shown that semi-hydrogenated graphene is a ferromagnetic semiconductor, with the explanation that the introduction of hydrogen destroys the conjugated π bonding network, localizing unpaired p electrons resulting in magnetic moments which can couple ferromagnetically [158]. A DFT study has indicated that graphene func-

tionalized by oxygen and hydrogen on opposite sides of the graphene layer can form a highly polarized, stable ferromagnetic metal [74]. This study also found that OH functionalized graphene has a lone $2p$ electron while extended p-p interactions could facilitate ferromagnetic coupling [74]. In this study, different magnetic and non-magnetic configurations were investigated to determine the lowest overall energy as discussed in Chapter 2.

Ferromagnetism has been recorded in RGO even at room temperature [70, 68]. Strong evidence suggests that defects, vacancies and lattice distortions play a significant role [159, 160, 93, 68]. Furthermore the large π conjugation of residual $C-O-C$, $C-OH$, $COOH$ and $C=O$ groups clinging to the main graphene skeleton provides the stability for localized magnetic moments [68].

Here we demonstrate a magnetic phase transition from diamagnetism at room temperature to ferromagnetism below 10 K due to localized magnetic moments. This is in agreement with the observation of a small energy gap in RGO films. The electrical transport properties and magnetic properties of our RGO samples are not dominated by the effects of disorder induced localization. Thus reduction via ascorbic acid introduces fewer topological defects in the removal of oxygen than hydrazine reduction resulting in RGO with improved qualities. Consequently the electronic and magnetic properties of RGO films are found to be different to previous reports.

5.2 Experimental Procedures

Experimental details are given in Chapter 4. Two-probe $I-V$ measurements were recorded from 4.2 K for RGO and from 77 K for GO to room temperature with an Agilent B1500 Semiconductor Device Analyser in a Janis continuous flow cryogenic micro-manipulated probe station. Measurements were performed under high vacuum (10^{-8} $torr$) to reduce the effect of atmospheric adsorbate on transport.

The magnetic properties were measured by Brice Jamieson at the Tyndall institute. The magnetization of GO and RGO samples was determined using a Quantum Designs MPMS-XL5 SQUID Magnetometer with a measurement accuracy of 1.0×10^{-8} emu, where the magnetic moment, on the order of 10^{-6} emu, was measured under a bias field of 50 Oe through a temperature sweep of 300 K down to 2 K. While subsequently warming the sample, hysteresis curves were taken for each material at set temperature points with an

applied field varied between 10 kOe and -10 kOe. The weights of the samples were then used to determine the magnetization in emu/g. To ensure maximum measurement accuracy, any residual magnetic field present in the system was nullified using Ultra-Low Field techniques. This was achieved by characterizing the residual field profile of the SQUID chamber after a full demagnetization using a high-precision gauss-meter under zero applied field. A low-field coil was then set to cancel out any remaining field resulting in a zero-field point at the centre of the SQUID where the sample was measured.

5.3 Results and Discussion

$I-V$ curves for GO (Fig. 5.1) show pronounced non-linearity and the conduction mechanism of GO was indeed found to be 2D VRH (see Figure 5.2) as reported previously, described by the expression [161]

$$G(T) = Ae^{-B/T^{1/3}} \tag{5.1}$$

where $B = 3/k_B N(E_F) L^2$, k_B is the Boltzmann constant, $N(E_F)$ is the density of states at the Fermi level and L is the localization length of charge carriers. In comparison the logarithmic conductance of RGO is plotted as a function of $T^{-1/3}$, inset in Figure 5.2. The temperature dependence of the current at constant voltage for GO and RGO films, shown in Figure 5.1, is significantly different and can be correlated with the density of defects. Carbon-oxygen bonds are sp^3 hybridized and disrupt the extended sp^2 conjugated network of pure graphene regions in GO sheets resulting in localization of charge carriers and consequently VRH as a result of the high oxygen content.

The $I-V$ curves of RGO show greater linearity (see inset in Fig. 5.3). As functional groups are removed the effects of localization are reduced, although a small concentration of residual functional groups remains. Resistance vs. temperature (R $vs.$ T) measurements of RGO show an exponential dependence in the range 4 K to 17 K (see Fig. 5.3). A small energy gap is opened up in this temperature range as at low temperatures, charge carriers are localized by defects and residual functionalized groups.

The linearity of the $I-V$ measurements further supports a small bandgap. However, resistance then changes little with temperature between 20 K and 35 K where it begins

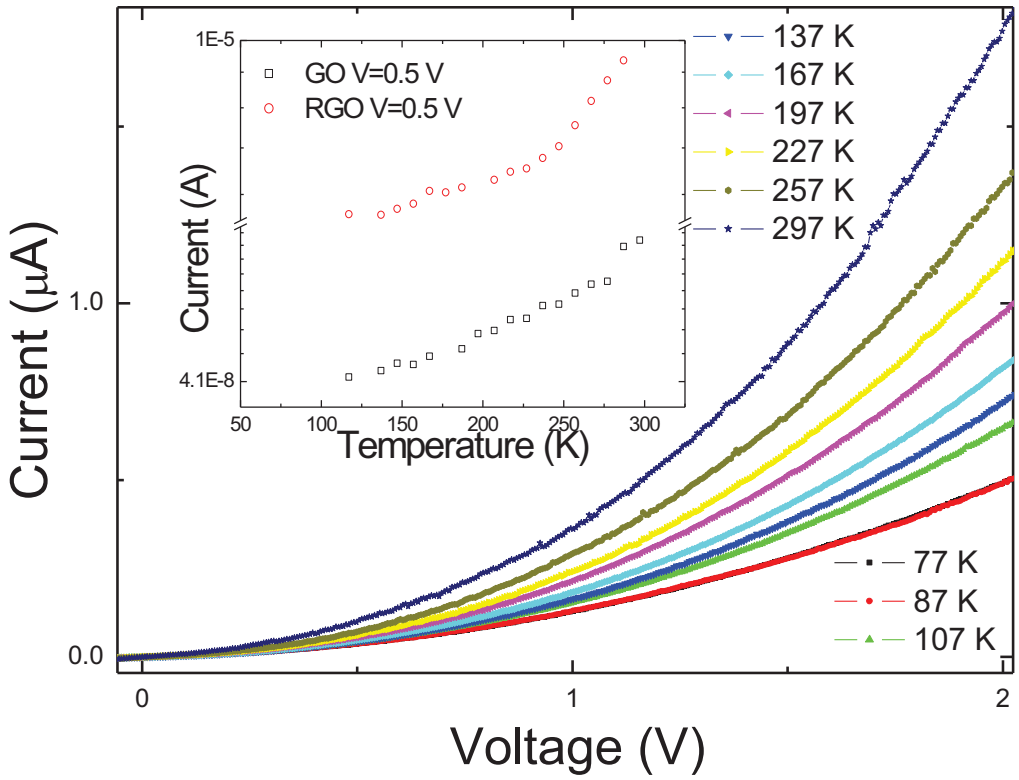


Figure 5.1: $I-V$ measurements for GO. Inset: Current as a function of temperature for GO and RGO.

to decrease steadily with temperature. As the temperature increases thermally activated electrons become delocalized as a result of the relatively low defect density of the RGO samples. The magnetization data also show a magnetic phase change from ferromagnetism to diamagnetism in the same temperature range.

We focus on the origin of the R *vs.* T behaviour of RGO samples which shows a marked similarly in profile to results obtained from monolayer graphene samples [30] although the present samples exhibit reduced conductivity. We have therefore attempted a fit to our data (dashed lines, Fig. 5.3) by implementing the model suggested by Skákalová *et al.* given by

$$R(T) = \frac{R_f \exp(-T/T_f) + R_0 + aT + bT^2}{1 + \exp(-E_c/k_B T)} \tag{5.2}$$

where we have included a (negative) T^2 term. The model suggested by Skákalová *et al.* was implemented without the inclusion of a quadratic term but in our case does not

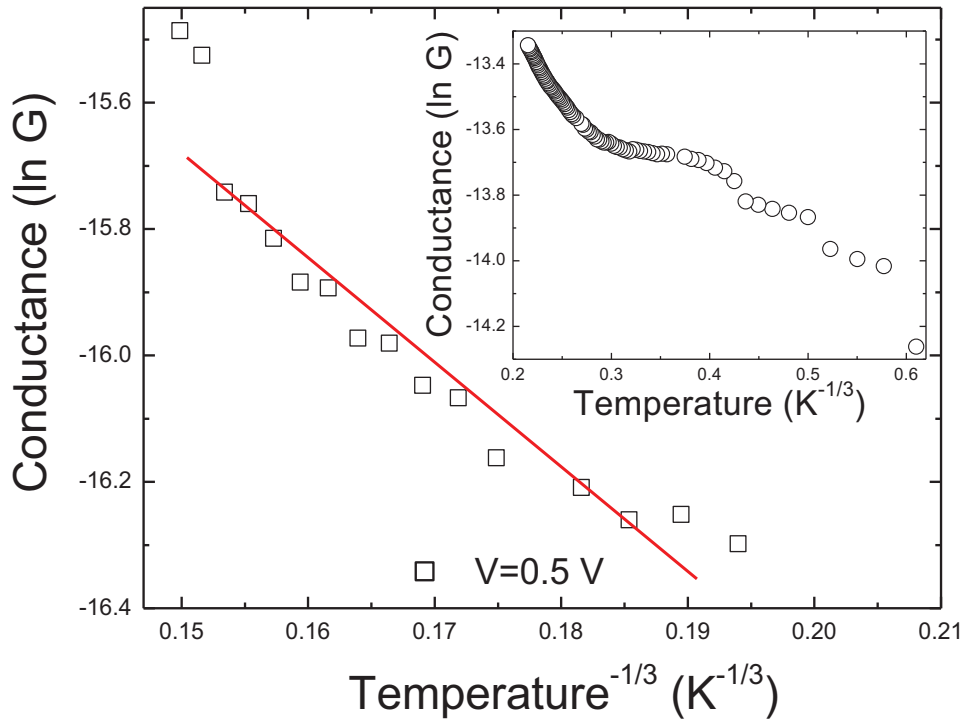


Figure 5.2: Logarithmic conductance of GO as a function of $T^{-1/3}$. Inset: the corresponding plot for RGO.

accurately capture the full data range. The term $R_f \exp(-T/T_f)$ arises from the decay of the amplitude of mesoscopic resistance fluctuations where T_f is a constant which determines the rate of exponential decay. With increasing temperature, the amplitude of MRF's decreases due to progressive dephasing (loss of coherence) of electrons. The term linear in T is due to electron-phonon interactions (acoustic phonons) and resistance R_0 is included as a scaling factor [30]. The denominator accounts for the increase in carrier density with temperature [30] where k_B is the Boltzmann constant. We find good fits to the data are achieved with activation energy $E_c = 11.3\ meV$ and $T_f = 3.3\ K$.

The sign of the coefficient b in Eq. 5.2 carries a very specific physical meaning and we have therefore made a comparative study (Figure 5.3, dashed lines) of the fits using $b = 0$, $b > 0$ and $b < 0$. We confirm that the addition of a negative quadratic term is required to fit the data over the low temperature range ($4\ K$ to $100\ K$) although the origin is subject to further investigation. Similar behaviour has been reported in high resistivity amorphous metals

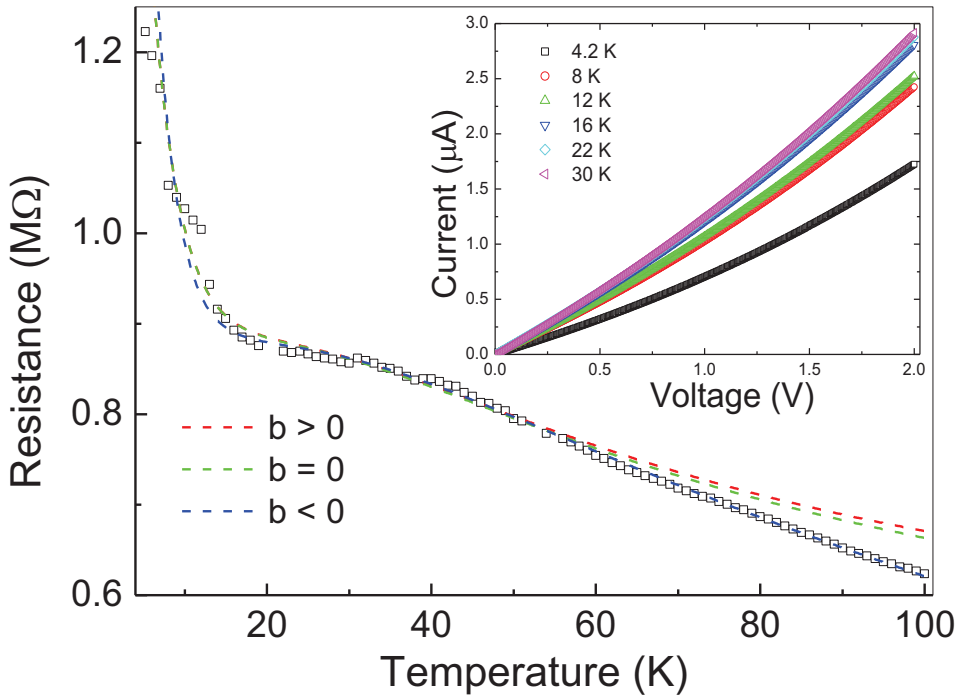


Figure 5.3: Resistance as a function of temperature in RGO. The dashed lines are fits to the data with the suggested model e.g. for $b > 0$, $b = 0$ and $b < 0$. Upper inset: Low temperature $I - V$ measurements of RGO.

as discussed in the introduction. In these alloys the electron-phonon interaction becomes ineffective as saturation effects develop with increasing temperature and the Debye-Waller factor dominates the resistivity [143, 144] resulting in a negative T^2 dependence due to the contribution of elastic scattering [145, 146].

This model for transport in RGO suggests that the decay of mesoscopic resistance fluctuations has a prominent effect on transport in RGO at low temperatures and highlights the role of elastic scattering processes.The band structure of graphene does imply a greater contribution of elastic scattering than in other materials as discussed above. RGO does contain intact graphene nano-islands so it is possible that the importance of elastic scattering arises in these regions however the exact origin of the T^2 term is subject to further investigation. In this regard, Hall measurements of RGO reduced to different degrees (through controlled chemical reduction) would be illuminating as they would highlight the specific role of the intrinsic resistivity of RGO devices. In addition, optical studies of the Tauc gap could pro-

vide information on the role of activated charge carriers and the mobility edge. Mesoscopic resistance fluctuations could be studied as a function of the carrier density although contributions to the resistivity from the substrate would then need to be considered as well. The dephasing induced by the application of an external magnetic field can also be used to study MRF's.

We have also checked the applicability of a model of combined variable range and nearest neighbour hopping (applied to bilayer graphene). In bilayer graphene, a similar R *vs.* T profile to the current measurements has been observed. At very low temperatures, conduction occurred through variable range hopping (less than 5 K) while at higher temperatures conduction occurred through nearest neighbour hopping [162]. At higher temperatures still, conduction was through thermal activation to the mobility edge. Localised states are found in the band tail, separated from delocalized states by the mobility edge. This picture is qualitatively very similar to the analysis of our data with the exception of MRFs. The suggested model has the form

$$R(T)^{-1} = R_1^{-1}\exp(-E_1/kT) + R_2^{-1}\exp(-E_2/kT) + R_3^{-1}\exp(-T_3/kT) \tag{5.3}$$

where $R_{1,2,3}$ are scaling resistances, $E_{1,2}$ are activation energies and T_3 is a hopping energy [162]. Our data can be well fitted by this model although a very small activation energy ($\sim 0.1\ meV$) is required for either of the activated terms [162] which is non-physical for the present system.

Prompted by the unconventional transport properties of RGO we have studied the magnetization and hysteretic behaviour of GO and RGO samples with the goal of investigating localized spins and the possibility of long range interactions. Magnetization as a function of temperature for GO and RGO is presented in Figure 5.4. Ferromagnetism was observed in GO between 2 K and 9 K, indicated by the positive magnitude of the magnetization curve. The ferromagnetic hysteresis curve at 2 K has a saturation magnetization in the order of 0.25 emu/g (see Fig. 5.5).

The origin of the ferromagnetism in GO is ascribed to localized spins formed on stable organic radicals which also provide π conjugation. As the temperature increases phonon scattering destroys the ferromagnetic ordering and a magnetic phase transition occurs at 10 K from the ferromagnetic phase to the diamagnetic phase, which persists to room temperature. Hysteresis curves at 10 K and 300 K showed a significant difference in gradient,

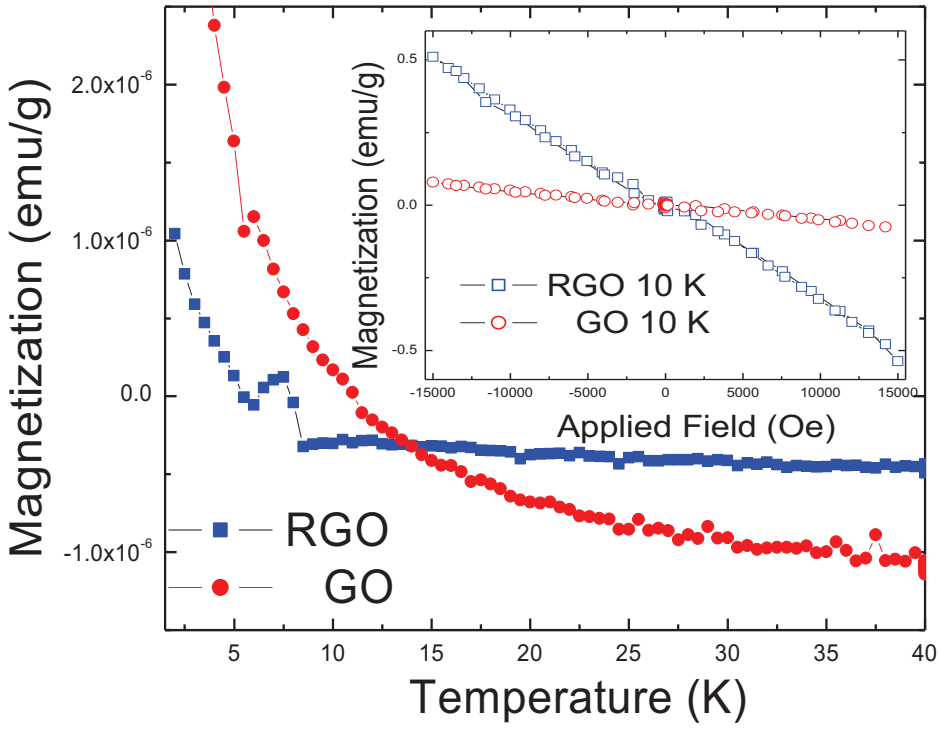


Figure 5.4: Magnetization as a function of temperature for GO and RGO. Inset is the magnetization of GO and RGO as a function of applied field at 10 K.

with a 60 % difference in the diamagnetic response at 10 kOe, as predicted by the negative magnitude of the magnetic moment in Figure 5.4.

When GO is reduced to form RGO free organic radicals are destroyed as oxygen is removed and defects and vacancies are introduced into the RGO lattice although a small concentration of residual free radicals remains. Topographical defects and vacancies play a more prominent role in the ferromagnetism of RGO than residual functionalized groups as the concentration of free radicals is low. Although the mechanism of ferromagnetic ordering is still a topic of some contention, it is believed that long-range coupling of localized spins is responsible [160, 163]. With the results of a recent study of the structure of RGO in mind [63], we believe that ferromagnetic domains are found in disordered and functionalized regions. Ferromagnetic coupling would then occur across intact graphene nano-islands. As such, the ferromagnetic coupling would be weaker for larger intact graphene nano islands. These intact nano-islands would also be expected to respond diamagnetically to an applied field.

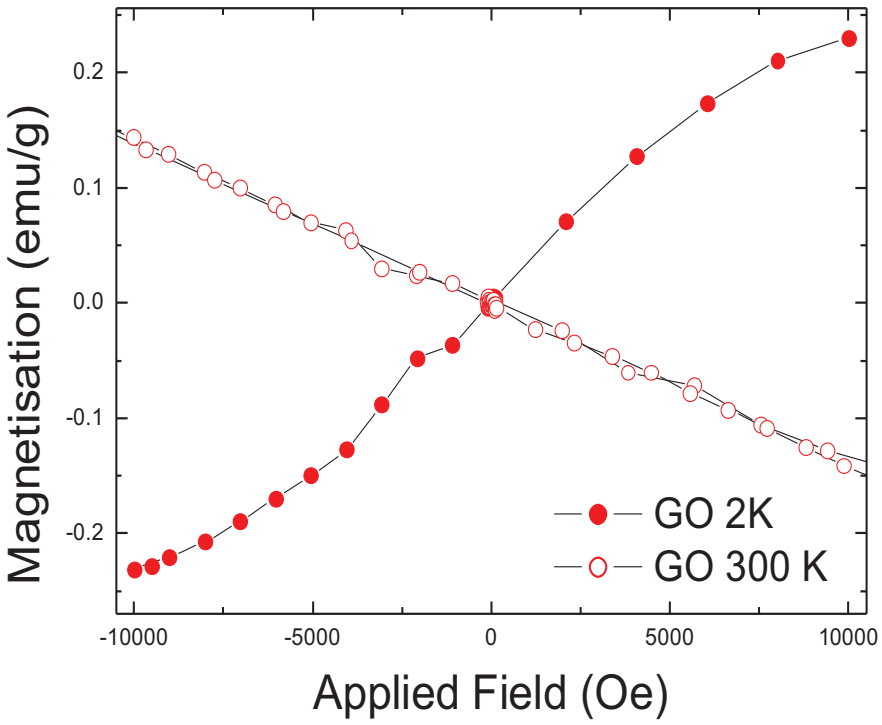


Figure 5.5: Hysteresis curves of GO at 300 K and 2 K indicating diamagnetism and ferromagnetism respectively.

Near the transition between the ferromagnetic and diamagnetic phases the sharp increase in magnetization in the RGO curve with local maximum at 7 K may indicate the competitive coexistence of the ferromagnetic and diamagnetic phases. A similar feature noted in a previous RGO study was attributed to the conflict between anti-ferromagnetic correlations and ferromagnetic order [70]. Figure 5.6 shows hysteresis curves for RGO at 8 K which do not saturate at 10 kOe. With increasing temperature, thermally activated electrons become delocalized, phonon interactions disrupt the ferromagnetic ordering and diamagnetism is therefore observed between 10 K and 300 K. There is little difference between the hysteresis gradients at 10 K and 300 K with only a 25 % difference in the magnetization at 10 kOe, predicted by the relatively flat magnetization profile from 10 K to 300 K. This rapid saturation of the diamagnetic response suggests that the ferromagnetic ordering in RGO is extremely sensitive to temperature changes indicating weak ferromagnetic coupling between ferromagnetic domains. In comparison the diamagnetic response of GO continues to increase due to the larger concentration of localized spins.

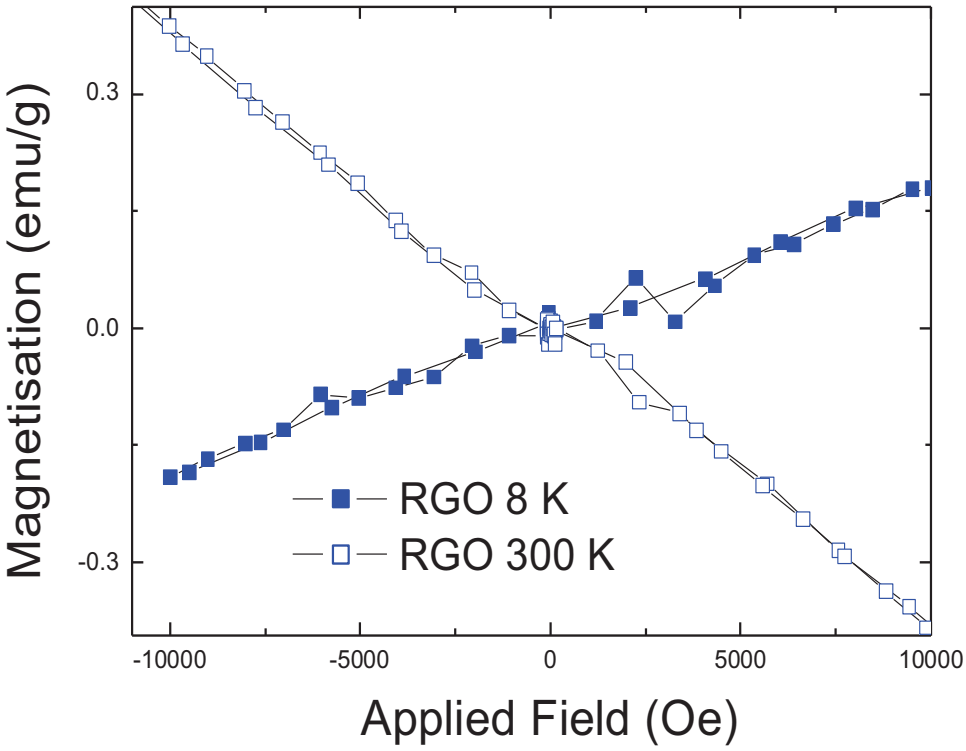


Figure 5.6: Hysteresis curves of RGO at 300 K and 8 K indicating diamagnetism and ferromagnetism respectively.

Below the ferromagnetic transition temperature, both materials exhibit a low coercivity which is unfortunately masked by fluctuations in the magnetisation at low applied fields. This low coercivity may indicate a superparamagnetic behaviour in RGO however a more detailed hysteresis trace at low temperature will be necessary to investigate this possibility.

5.4 Conclusion

We have shown delocalized transport at intermediate temperatures in RGO layers with an energy gap observed at low temperatures. At low temperatures, MRF's are prevalent indicating a low mobility of charge carriers due to successive elastic scattering although weak localization is absent as is the case for pristine graphene. The decay of the amplitude of MRF's also displays the as yet unexplained exponential decay of pristine graphene. At higher temperatures, through activation of charge carriers (with an activation energy of 11 meV),

the effects of elastic scattering again dominate the transport properties. $I-V$ measurements also show evidence of a small band gap. The scaling of the resistance with temperature deviates from the general features associated with graphene and shows a negative quadratic dependence. This is most likely due to residual free radicals attached to RGO sheets. A small contribution to the resistivity from acoustic phonons was also found.

A ferromagnetic to diamagnetic phase transition was observed with increasing temperature in both GO and RGO. The saturation of the magnetization of RGO was more rapid than that of GO. We find evidence of the coexistence of diamagnetic and ferromagnetic phases at low temperatures for RGO. Localized spins are found at defects, vacancies and residual free radicals with long range coupling taking place across intact graphene nano-islands. While GO has an abundance of free radicals, the pristine graphene regions of RGO may promote ferromagnetic ordering.

The reduction of GO with ascorbic acid proved highly effective. We believe that reduction with ascorbic acid introduces fewer defects and vacancies in the process of reduction than conventional hydrazine reduction. Consequently the present transport properties are not dominated by the effects of disorder and the phase change from ferromagnetism to diamagnetism occurs at a lower temperature. However, delocalized states combined with ferromagnetism suggest that correlations between conduction electrons and local magnetic moments could be significant. Further studies on RGO including low temperature magnetoresistance and Hall measurements were therefore carried out in the four probe configuration (see Chapter 6).

Chapter 6

The Kondo Effect in Reduced Graphene Oxide

In Chapter 5 unusual transport features in reduced graphene oxide were demonstrated. Those studies were therefore extended to four probe measurements at low temperatures and high magnetic fields. We find a metal-insulator transition in the resistance as a function of temperature. At very low temperatures, resistance shows a quadratic temperature dependence with a positive temperature coefficient of resistivity. After attaining a maximum, the temperature coefficient of the resistivity then changes as resistance decreases quadratically with temperature followed by a logarithmic dependence. The magneto-resistance, decreasing with the applied field, scales with a characteristic temperature. These novel features in reduced graphene oxide may be a result of the interaction between conduction electrons and localized moments (the Kondo effect) and a schematic model of intact graphene nano-islands embedded within disordered regions is suggested as a possible explanation where the disordered regions form localized moments and extended states form in intact graphene regions. In Chapter 3 the conditions for the existence of Fano resonances close to E_F was discussed. In this chapter, we discuss the formation of the Kondo resonance as a result of the coupling between local moments and delocalized conduction electrons. We begin with a brief introduction to the Kondo effect, focusing on the Fermi liquid description. We then discuss some of the intrinsic properties of Kondo physics in graphene as opposed to conventional materials. We then present transport measurements interpreted within the Fermi liquid description of the Kondo effect.

6.1 Introduction

6.1.1 The Kondo Effect

The term "Kondo effect" has come to be associated with a number of different forms of interaction between localized magnetic moments and conduction electrons. While treatments vary according to the number of conduction channels, the number of impurities, the form of local moments (whether isolated impurities, densely packed impurities or clusters of impurities) and the nature of spin flip scattering (whether only s-wave behaviour or if spins greater than 1/2 are allowed), the underlying Kondo physics is similar in each process [164, 165, 166]. We begin with a discussion of the single impurity Kondo model which reveals some of the elementary physics associated with the correlations between localized magnetic moments and conduction electrons. We then discuss the single impurity Anderson model. The generic physical interpretation of the Kondo effect, stemming from the single impurity Anderson model involves a localized magnetic moment embedded in a sea of delocalized electrons around the Fermi level where there is some hybridization between conduction band states and the local moment. The single impurity Kondo model is in fact a condensed form of the Anderson model which neglects hybridization, focusing only on the exchange interaction [165].

The logarithmic temperature dependence of the low temperature resistivity of certain alloys evaded a satisfactory explanation for over 30 years [164]. While Friedel suggested the notion of virtual bound states as a result of resonant scattering, the problem remained unresolved. Anderson, extending this notion, realized that short range interactions involving localized electrons had to be incorporated with the formation of a narrow resonance [165]. Finally the single impurity Kondo theory was developed which could explain the logarithmic divergences although this theory raised new questions and much of the underlying physics remained unclear [164]. This problem generated great interest due to the wealth of physics surrounding it and became known as the Kondo problem. Jun Kondo's great insight was that the interaction between localized magnetic moments and conduction electrons was related to the logarithmic divergence at low temperatures. Treating the system to second order in perturbation theory, Kondo was able to provide an explanation [165]. However, it was only with the development of Wilson's numerical renormalization group theory that the true nature of Kondo physics was revealed. This regime plays a central role in the physics of heavy

Fermions [167]. However it is still an emerging field in the physics of graphene devices.

The Kondo effect stems principally from the interaction of conduction electrons with local spins. The Kondo effect is infused with the rich physics, complexities and subtleties of the many body problem. In solving the Kondo problem, a wide variety of methods were employed while new theoretical tools were developed. The Kondo effect encompasses a number of related phenomena in different systems but the underlying principles begin with the single impurity Kondo model which is also inherently a many-body problem [168]. Here, we give a brief introduction to the single impurity Kondo model. Consider a local spin within the Fermi "sea" of conduction electrons. Such a situation may arise in the limit of low doping when ferromagnetic impurities are introduced to metals. Naturally, the conduction electrons will interact anti-ferromagnetically with the local spin. We consider initially a localized d electron and an itinerant electron which scatters isotropically from the impurity (s- wave) [168]. The Hamiltonian of interaction between the conduction electron and local spin (s-d exchange interaction) is described by

$$\mathcal{H}_{int} = -2J\mathbf{S}_{imp} \cdot \mathbf{s}_{ce} \tag{6.1}$$

where J characterizes the strength of the interaction, $\mathbf{S}_{imp}$ is the impurity spin and $\mathbf{s}_{ce}$ is the conduction electron spin. The single impurity Kondo Hamiltonian may be written as

$$\mathcal{H}_{int} = \sum_{\mathbf{k},s} \epsilon_k c^{\dagger}_{\mathbf{k}s} c_{\mathbf{k}s} + \frac{J}{2} \sum_{\mathbf{k}\mathbf{k}'} \sum_{ss'} c^{\dagger}_{\mathbf{k}s} \sigma_{ss'} c_{\mathbf{k}'s} \cdot \mathbf{S_{imp}} \tag{6.2}$$

where J is most often negative, indicating an anti-ferromagnetic interaction although in principle it could also be positive. States are labeled by momentum ($\mathbf{k}$) and spin (s). The first term accounts for kinetic energy in the conduction band. The second term accounts for the interaction between the localized magnetic moment of a d electron and an electron in the conduction band where σ represents the conduction electron spin and S_{imp} represents the impurity electron spin. This model assumes implicitly that there is a localized magnetic impurity. In addition only s-wave behavior is assumed. In Kondo's original approach, a small interaction term J was considered and the Hamiltonian was expanded within perturbation theory [164].

After describing the interaction, scattering theory may be applied to the system to determine the temperature dependence of the resistance [166]. Exchange scattering is included

in the total elastic scattering probability as a spin-flip process [168]. Kondo calculated the scattering matrix by expanding the interaction term to second order. The resistivity was found to depend logarithmically on the temperature at low temperatures. This was sufficient to explain the negative logarithmic temperature dependence of the resistivity at low temperatures but the theory predicted divergences as the temperature approached zero. The physical insight that was gained from the Kondo model was that spin-flip scattering due to *s-d* interactions dominates carrier scattering at low temperatures (where the electron-phonon interaction is reduced) but below some temperature known as the Kondo temperature (T_K) spin-flip scattering was suppressed. T_K was found to be a principle scaling factor [164, 167]. Additionally, it was known that the magnetic moment vanished as temperature approached zero.

These unresolved issues became known as the Kondo problem and were finally resolved with the introduction of Wilson's numerical renormalization group theory which is discussed later. Currently, Kondo physics is most often treated within the Anderson impurity model. The Kondo Hamiltonian considers a fixed local moment. The Anderson model on the other hand includes the possibility of tunneling of the localized moment and conduction electrons on and off the impurity site. In this model a finite Coulomb interaction is assumed on the impurity site [169]. The Anderson model is often applied to quantum dot systems where the dots are ferromagnetic or induce ferromagentism. The Anderson Hamiltonian is given by

$$\begin{aligned}\mathcal{H}_{int} = \sum_{\mathbf{k},\sigma} \epsilon_k c^\dagger_{\mathbf{k}\sigma} c_{\mathbf{k}\sigma} + \sum_{\sigma} \epsilon_0 d^\dagger_\sigma d_\sigma + U d^\dagger_\uparrow d_\uparrow d^\dagger_\downarrow d_\downarrow \\ + \sum_{\mathbf{k},\sigma} \left(v_k d^\dagger_\sigma c_{k\sigma} + v^*_{\mathbf{k}} c^\dagger_{\mathbf{k}\sigma} d_\sigma \right)\end{aligned} \tag{6.3}$$

The first term describes the kinetic energy of electrons in the conduction band. The second term describes the quantized electronic energy states of the spin-degenerate state near E_F of the localized impurity (usually a d or f electron). The third term describes the Coulomb interaction energy, which allows the doubly degenerate site to be occupied by a single electron and maintain a net magnetic moment. As $T \rightarrow 0$, the Coulomb repulsion also facilitates the formation of a singlet ground state [165]. The fourth term represents the coupling between the local magnetic moment and the conduction electrons. In this case, coupling is effectively hybridization of s and d (f) electrons. This hybridization allows electrons to tunnel into and out of the localized state while preserving their spin. Through

approximation, this term can be reduced to Eq. 6.1. A schematic diagram of the Anderson model is given in Figure 6.1.

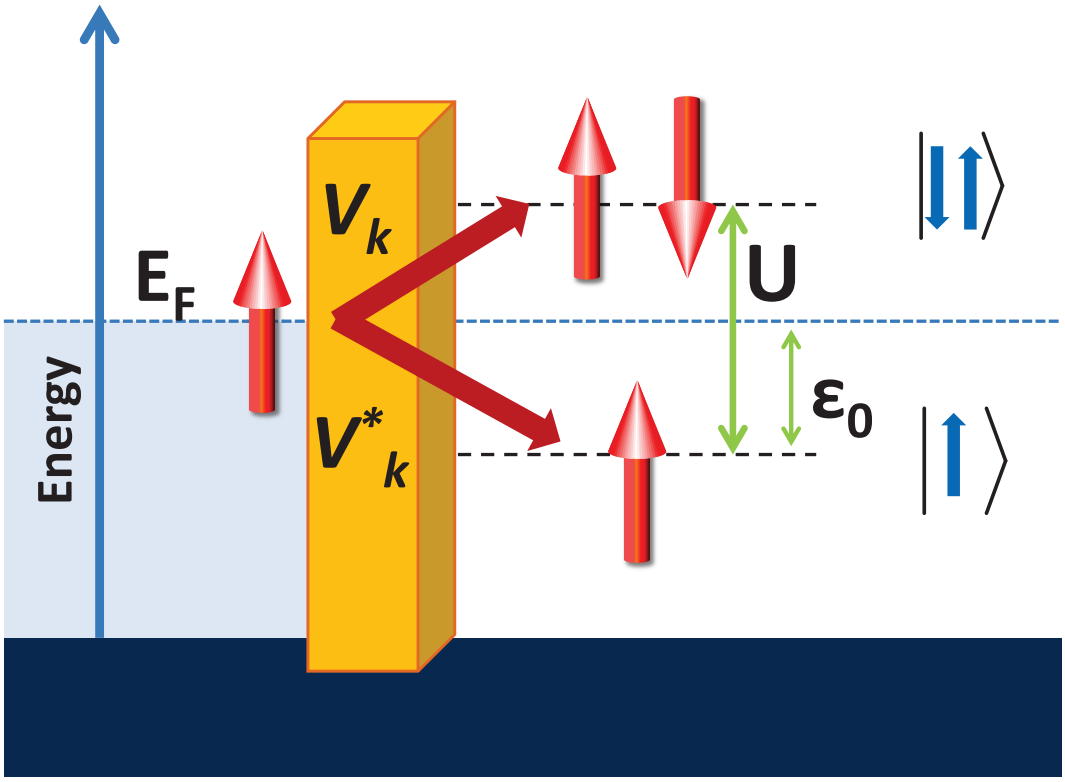


Figure 6.1: Schematic diagram of the Anderson single impurity model.

The Kondo model is in fact a reduced form of the Anderson model [166]. If the coupling (hybridization) between the local moment and the delocalized states of the conduction band is small and the Coulomb repulsion is large then the local moment is effectively localized on the impurity site and a model qualitatively similar to the Kondo model is recovered. The Anderson model is more generally applicable as it incorporates mixed-valence effects [165]. The formation of the Kondo singlet ground state is a continuous phase transition as the temperature decreases where the Kondo temperature (T_k) is the energy scale for the phase transition. The Kondo temperature within the Anderson model can be expressed as

$$T_K \approx \sqrt{\Gamma U}\mathrm{Exp}(\pi\epsilon_0(\epsilon_0 + u)/\Gamma U) \tag{6.4}$$

where Γ is the rate of change of occupation of the dot, U is the Coulomb repulsion of the localized impurity and ϵ_0 is the occupied level of the impurity, as shown in Figure 6.1. The

Kondo temperature increases with increasing Γ and is higher if ϵ_0 is close to E_F.

Due to the Coulomb interaction the degeneracy of the localized moment at energy ϵ_0 is effectively destroyed as the energy of next available localized state (of opposite spin) is the sum of the intrinsic energy and the Coulomb energy, $\epsilon_0 + U$ [169]. This model also incorporates the mixing of the s and d states i.e. the coupling of the conduction band states and the localized moment. In the scattering of conduction electrons with the local moment at temperatures higher than the Kondo temperature, the magnetic quantum number of both states may change i.e. the conduction electron may spin flip the local moment or vice versa or both.

The coupling between the conduction electron and the local spin allows the local moment to tunnel off the impurity site into the conduction band, preserving its spin. With the impurity site vacant, an electron from the conduction band may tunnel onto the impurity site, also preserving its spin. In this process, the spin of the impurity site changes while the Coulomb repulsion prevents double occupation of the impurity site. This process is illustrated in Figure 6.2.

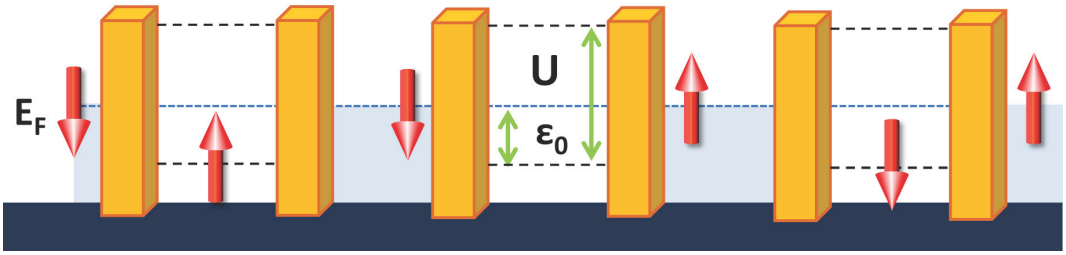


Figure 6.2: Schematic diagram of a conserved tunneling process within the Anderson impurity model.

The influence of the exchange interaction increases with decreasing temperature as phonon interactions disrupt the s-d interaction. Temperature scaling is one of the most critical features of the Kondo effect, not only the scaling of the resistivity with temperature but also the scaling of the magnetization and specific heat. For the time being, we consider the low temperature regime where phonon interactions are insignificant in comparison to the exchange interaction. Conduction electrons within the energy range $E_F \pm k_B T$ shield the local moment due to the anti-ferromagnetic interaction with conduction electrons. The exchange interaction is most prevalent close to the Fermi surface due to the phase constraints (developed by Friedel) [167].

At the Kondo temperature, a quasi-bound singlet state forms [168, 169, 164, 166]. With the singlet state formed, the mixing of the local moment and the conduction electron states forms a sharp resonance at E_F, the width of which is directly related to the strength of the interaction [169]. In this low temperature limit, the coupling is strong, $\rho J \to \infty$ where ρ is the density of states. With the local moment entirely screened, it no longer *directly* influences conduction electrons. Instead, scattering of both the spin up and spin down channels results in a phase shift of $\pi/2$ i.e. $\delta_{\uparrow,\downarrow} = \pi/2$.

Mattiesen's rule states that the total resistivity is comprised of contributions from different interactions [166]. As the temperature increases, phonon interactions interfere with the resonance at the Fermi energy. The formation of the Kondo quasi-bound ground state is prohibited and the contribution to the resistivity from Kondo scattering diminishes with contributions from phonon interactions dominating the resistivity. The opposite natures of the scaling of the interaction term and phonon terms with temperature leads to the notion of the Poor Man's Scaling technique for treating the Kondo problem [168]. In this approach, as the temperature decreases different scattering mechanisms, treated within perturbation theory, are eliminated. However this approach could not account for the interaction close to the Kondo temperature.

Wilson's numerical renormalization group theory (NRG) provided the tools for a complete description of the Kondo effect across the Kondo temperature and provided access to the physics of the spin singlet ground state while perturbative methods break down [168]. In this approach, energy and space are discretized to focus on effects at E_F at ever lower temperatures while the Hamiltonian, which is reformulated into integrals over energy, is updated. New operators are constructed to be spherical waves about the impurity site as s wave states couple. Using the discretized space, a set of complete orthonormal functions is defined to span the energy space in each interval. Finally, integrals over energy are then replaced by summations over intervals. New orthonormal operators can then be defined, the first being localized closest to the impurity, each of which couples to the next operator sequentially. In this way, scaled Hamiltonians are developed which apply to different energy scales. Different variations of the single impurity Kondo model have been developed and applied in various systems where applicable. The Coqblin-Schrieffer model is a variation of the single impurity model which accounts for non s-wave scattering so different angular momentum states are considered in contrast to only spin-flip processes. Multi-channel Kondo models have been developed which find application in certain quantum dot systems while

multi-impurity models have been developed to account for interactions between localized spins. The common denominator is the many-body physics of correlated electrons.

The Kondo effect within the Anderson model has been described in Fermi liquids through WNRG calculations. Doped graphene is expected to be a Fermi liquid so it is possible that RGO could be a Fermi liquid if the concentration of residual free radicals is low [40]. In Fermi liquid theory, the characteristic temperature scale for the thermodynamic properties is the Fermi temperature (T_F) which is defined as

$$T_F = \frac{E_F}{k_B} = \frac{\hbar^2 \left(3\pi^2 n\right)^{2/3}}{2mk_B} \tag{6.5}$$

where n is the density of states and m is the effective mass. As the temperature of a Fermi liquid systems approaches T_F, strong interactions ensue. With decreasing temperature, particle dynamics can no longer be understood in terms of a non-interacting Fermi gas however there is a correspondence between the interacting and non-interacting behavior in that the spin, charge and momentum are the same in both descriptions [166]. In Fermi liquids there is also a sense of renormalization of quasi-particle excitations with temperature, in a similar sense to the Poor Man's Scaling approach outlined earlier. These additional correlations must be accounted for when studying the Kondo effect in Fermi liquid systems. Electrons within the energy range $k_B T_F$ of E_F contribute to the formation of the Kondo resonance.

The Kondo resonance forms a quasi-bound state at E_F which is *occupied* by a single conduction electron (considering a spin 1/2 impurity). This is due to the correlation between conduction electrons at the Fermi level and the energy of the one-level state. This leads to the formation of a peak in the local density of states at the Fermi level. This single conduction electron, effectively removed from the problem, screens the local moment [165, 164, 169]. When $T << T_K$ and the local moment is entirely screened, the resistivity is governed by scattering (at low energies, close to E_F) from the electrons which screen the local moments. At temperatures sufficiently less than the Kondo temperature the resistivity varies as T^2. This may be physically interpreted as electron-electron scattering induced by the accumulation of conduction electrons which screen the localized moments. This electron screening has the additional effect of removing the magnetic moment of the system i.e. the local spin is quenched.The Fermi sea occupies states which prevent conduction electrons (in spin singlet states) from scattering. The Fermi liquid states are characterized by phase

shifts. In Fermi liquids, the number of available scattering states decreases with decreasing temperature along with the resistance. The temperature dependence of the resistivity of a Fermi liquid is, in general, given by

$$\rho(T) \propto \rho_0 + AT^2 \tag{6.6}$$

where A is positive. A similar temperature dependence is discussed in Chapter 5 (in the context of disordered metals) although the mechanism is different. If $T < T_F$ then the DOS is approximately constant and there is an energy relation which characterizes the energy of the Kondo singlet state (E_{ss}), given by

$$E_{ss} = D\text{Exp}(\frac{4}{3J_0 n(0)}) \tag{6.7}$$

where $n(0)$ is the constant density of states, D is the upper energy limit of the conduction band and J_0 is the magnitude of the exchange interaction. The energy E_{ss} can be viewed as the "binding energy" of the Kondo singlet.

The width of the Kondo resonance in the DOS is directly related to the Kondo temperature. The Kondo temperature is also directly related to the rate of transition of electrons on and off the impurity site Γ. In Chapter 3 we discussed how the lifetime of the quasi-bound states formed through constructive quantum interference is inversely related to the width of the quasi-bound state in the DOS. In the case of the Kondo resonance, the greater the transition rate Γ, the greater the width of the Kondo resonance and the higher the Kondo temperature.

In the Fermi liquid theory, which describes the excitations of quasi-particles and hence the thermodynamic properties, the characteristic temperature scale of the susceptibility, specific heat and magneto-resistance is also T_F. Magneto-resistance within the Fermi liquid regime shows the characteristic E^2 scaling with the magnetic field. Kondo scattering is expected to result in negative magnetoresistivity [168, 164, 165]. The application of a magnetic field increases the Zeeman energy with the result that the number of available states for conduction electrons to scatter into decreases, consequently the resistance decreases. At higher temperatures this effect is expected to decrease as the increased thermal energy increases the number of available states.

The mixture of the localized moment and conduction band states has an important effect at low temperatures. A conduction electron scattering from a localized moment (where $T > T_K$) may cause spin-flip of the conduction electron or the localized moment. However, scattering is not limited to only one conduction electron and there are consequently many conduction electrons entangled together with the result that the impurity has a large scattering effect due to correlation. For a local spin up moment, this mixing of states increases the number of correlated spin down states close to the energy of the localized moment. The spin down electrons are therefore quasi-localized. However, the localized moment may lower its kinetic energy by hopping to a virtual state (of the same spin) at around the Fermi energy. The formation of a localized moment in this model therefore relies on the energy of the one level states, the Coulomb energy and the position of the Fermi level in relation to the broadening of the one-electron level.

6.1.2 Kondo Correlations in Graphene

Amid the plethora of studies investigating various aspects of electronic transport in graphene the coupling of conduction electrons to localized magnetic moments is being studied intensely both as a fundamental problem in condensed matter and for the development of novel spintronic devices [170, 171, 172]. The Kondo physics of graphene is expected to be atypical due to the Dirac nature of charge carriers in graphene and the zero density of states at E_F so the phase transition with temperature from Kondo screened to unscreened may be unusual [173]. It is believed that local moments may be stably formed in graphene through the incorporation of magnetic adatoms or induced through the incorporation of non-magnetic impurities which induce a magnetic moment through a non-bonding lone electron. Through tight-binding studies it was shown that single vacancies in graphene can induce localized states close to E_F, their influence stretching over many lattice sites [92]. Coulomb interactions, not included in the previously mentioned study, may induce magnetic moments at the localized states.

The single impurity Kondo model has been applied to graphene where spin 1/2 moments were considered. Equation 6.7 illustrates that T_K depends on the DOS at E_F. In graphene, a pseudo-gap DOS is used which illustrates that Kondo screening is suppressed and for small exchange interaction the Kondo screening is entirely absent and the Kondo temperature in graphene is expected to be very low [173]. This may also have implications for the

Kondo temperature as a universal scaling temperature as the sensitivity of the specific heat and susceptibility to the reduced electron screening may not be the same as that of the resistivity. With regard to the resistivity as well, the scattering properties of graphene (discussed in Chapter 5) may also result in anomalous effects. In addition, the tendency to from electron-hole puddles may also mask Kondo physics in graphene and result in a wide range of local Kondo temperatures due to local differences in the charge distribution [173].

The mass of single layer graphene prevents conventional magnetic studies, such as SQUID studies, on individual layers. On the other hand, local properties can be probed through transport studies. The introduction of ferromagnetic adatoms (such as Co) has been widely studied while in parallel features such as vacancies and topographical distortions as well as non-magnetic adatoms which induce magnetism have also been studied. Kondo physics in graphene is an emerging field with many open questions and apparent contradictions. Ferromagnetism has been recorded in functionalized graphenes as discussed in Chapter 5 [70, 68], and graphite [159] even at room temperature indicating that the Kondo effect may be significant in these materials despite the lack of ferromagnetic impurities. In graphene, ferromagnetism has been attributed to edge states [174] , topographical defects and vacancies where localized moments may form [68, 160, 93]. In reduced graphene oxide ferromagnetism is likely due to the formation of local moments at residual functionalized groups, defects and vacancies [70, 68]. The large π conjugation of free radicals is believed to provide the stability for ferromagnetic ordering although the exact mechanism is as yet unclear [68].

The Kondo effect in graphene has been theoretically investigated extensively, some studies beginning with the Anderson model Hamiltonian for a magnetic impurity adsorbed on a graphene sheet with calculations performed using Wilson's group renormalization method [175]. It has been documented that in graphene the low density of states in the region of the Fermi energy may allow for the formation of sharp resonances in the density of states if covalent molecules are attached to graphene or if there are vacancies in the graphene sheet [172] . It was found that there is no Kondo resonance in the density of states at the Fermi energy for undoped graphene. However in doped graphene (where E_F is shifted away from the Dirac point) a Kondo peak indeed appears at the Fermi energy [175].

Another recent study has focused on the formation and effect of magnetic moments near vacancies in graphene and their potential ferromagnetic coupling to conduction electrons [172] . It should be noted that there are indeed differences between the moments of magnetic impurities conventionally treated in the Kondo effect and the localized moments formed in

graphene. In the case of ferromagnetic coupling, the resonant state is orthogonal to the conduction states and the virtual hopping between the localized state and the conduction electrons no longer occurs. The coupling between the magnetic moment and conduction electrons was found to be ferromagnetic with a magnetic susceptibility proportional to inverse temperature [172]. It has also been pointed out that disorder induced charge puddles may destroy the magnetic moment if the carrier concentration is high enough.

Spin-transport measurements have been used to demonstrate local moment formation in graphene with chemisorbed hydrogen [176]. Spin-currents were generated through cobalt contacts and spin-transport measurements were performed under an applied field as a function of exposure (and consequent chemisorption) of hydrogen. Changes in the non-local spin dependent resistance were induced through hydrogen incorporation and compelling evidence suggests that spin-spin exchange coupling occurs between local moments and conduction electrons [176]. In addition, the experimental demonstration of spin currents bodes well for the realization of graphene spintronic devices which have been widely studied theoretically but have been found to be difficult to achieve experimentally.

An *ab-initio* study indicated that graphene functionalized with fluorine on one side might exhibit giant magneto resistance [74]. Experimentally, dilute fluorine incorporated graphene has also been studied [177]. Colossal negative magnetoresistance as well as unusual steps in the magnetoresistance at low temperatures (which may be due to the filling of quantized energy levels) were reported which cannot be satisfactorily explained by current theories of scattering from impurities in graphene and it was suggested that magnetic interactions may play a role. Inspired by the similarity of their results with studies on magnetites, these authors suggest that local moments form through the incorporation of fluorine. These local moments induce magnetic polarons which in turn delocalize under the application of an external field resulting in large negative magnetoresistance [177].

Further studies on fluorinated graphene found anomalous behavior of the phase coherence length which was found to saturate at temperatures less than 10 K [178]. Magnetic impurities are expected to break the time reversal symmetry and therefore contribute to the loss of phase coherence over and above the usual mechanisms of electron-electron interactions and electron-phonon interactions which have been widely studied in graphene. In graphene, the relationship between the phase coherence length and the magnetoconductance accounts for the conventional weak localization effects as well as weak anti-localization as a result of inter-valley scattering and chirality considerations (as discussed in detail in Chapters 2

and 5). While the phase breaking as a result of phonon interactions and electron-electron interactions was found to be the same as in pristine graphene, both the phase coherence length and the phase breaking rate were found to saturate at low temperatures. These results provide evidence of spin-flip scattering which may account for the anomalous time-reversal symmetry breaking [178]. At low temperatures, the stability of local spin formation is enhanced so the time-reversal symmetry is broken resulting in saturation of the phase coherence length. The spin-flip rate was used to calculate a Kondo temperature of 0.01 mK (dependent upon the carrier density). In both of these studies, a long spin-diffusion length (in the range of a few microns) was demonstrated [178] with significant implications for the viability of graphene spintronic devices, specifically spin-polarized devices. Additionally, it was demonstrated that the spin diffusion length can be controlled with the carrier density.

Although direct evidence of magnetic moment formation has been limited in graphene, the studies previously mentioned confirm some of the prerequisites for graphene spintronics. They illustrate that magnetic moments can be induced in graphene with relatively minor changes to graphene. On the other hand, spintronics in functionalized graphenes, as opposed to modified graphenes, has so far received little attention. In the present study on RGO we begin with a material which is known to form local moments (the exact mechanism is still under debate) however so far transport in RGO has been limited by strong localization effects as a result of the reduction method used.

In addition to local moment formation and retention, sufficiently delocalized conduction electrons are a prerequisite to allow hybridization between the local moment and the conduction electrons. The electrical transport properties in reduced graphene oxide have been attributed to Mott variable range hopping in a number of studies as a result of the disorder induced in the oxidation-reduction process and the small concentration of residual functionalized groups which remains after reduction, as discussed in Chapter 5 . Although other studies have reported space charge limited conduction [155] or a variation from variable range hopping to activated transport [67], these mechanisms are still dominated by the effects of disorder. A recent study has shown activated transport in RGO indicating band-like transport [179].

RGO consists of intact graphene nano-islands interspersed with regions dominated by topographical defects and residual functionalized groups [155, 65, 63]. These structural properties were incorporated successfully into a recent study of the electronic transport properties which showed Efros-Shklovskii variable range hopping and Coulomb blockade

effects [65]. A schematic transport model was consequently developed in which graphene regions are embedded in the disordered matrix like quantum dots . The Coulomb oscillations that were observed indicate single electron tunnelling between the disordered regions [65]. With this picture in mind together with the possibility of band-like transport it would seem likely that the interaction of conduction electrons with localized magnetic moments in disordered regions (both residual free radicals and topographical defects) may play a significant role in the electronic and magnetic properties of RGO.

Recently the Kondo effect has been observed in irradiated graphene [180]. Irradiation creates vacancies and topographical defects where localized magnetic moments may form. The conductivity as a function of gate voltage showed asymmetry which was ascribed to non-zero on-site energy for the defects. The magnetoresistance was found to be negative, the result of the disorder induced through irradiation which causes weak localization effects. While spin-transport has been widely studied theoretically in graphene and modified graphenes with experimental studies being actively pursued, the possibility of spin transport in functionalized graphenes has received little attention despite reports of ferromagnetism. A DFT study has demonstrated that oxygen and hydrogen functionalized graphenes could be exploited in spin filters where the stable ferromagnetic moment was found to be localized on unfunctionalized carbon atoms[74]. With additional motivation provided by the unusual transport properties presented in Chapter 5, we have therefore performed more detailed transport measurements on RGO.

6.2 Experimental Techniques

Four terminal RGO devices were fabricated by dielectrophoresis across a gold Hall bar in the van der Pauw configuration, suspended across a gap of approximately 1 μm. Four probe resistance versus temperature (R *vs.* T) and magneto-resistance (MR) measurements were performed in a cryogen free automated measurement system from 2 K and up to fields of 12 T. A Keithly 2400 was used to source a current of 10 μA and a Keithly 2182A was used to measure voltage.

6.3 Results and Discussion

R *vs.* T measurements of RGO from 2 K to 100 K are shown in Figure 6.3. At low temperatures resistance increases quadratically with temperature. The blue solid line in the inset of Figure 6.3 is a straight line illustrating a quadratic temperature dependence (with a positive TCR) up to around 20 K. After attaining a maximum, resistance then decreases quadratically up to around 50 K before decreasing logarithmically to around 90 K. We employ the Fermi liquid description of the Kondo effect where the temperature dependence of the resistivity depends on the Kondo temperature [181, 180]. In the low temperature region it is expected to behave as

$$\rho(T) = \rho_{c1} + \rho_0 \left(1 - \left(\frac{T}{T_K}\right)^2\right) \tag{6.8}$$

At low temperatures the energy of conduction electrons is close to the energy of localized magnetic moments. The conduction electrons then form quasi-localized states around the local moments through the Kondo resonance resulting in enhanced electron scattering at low temperatures. The resistance shows a negative quadratic temperature dependence (the solid red line in Figure 6.3 is a fit to Equation 6.8). At higher temperatures, the resistance scales according to the logarithmic expression

$$\rho(T) = \rho_{c2} + \frac{\rho_0}{2}\left(1 - 0.470\ln\left(\frac{1.2T}{T_K}\right)\right) \tag{6.9}$$

At higher temperatures, the scattering of conduction electrons may change the magnetic quantum numbers of both conduction electrons and the localized moments (spin-flip scattering) resulting in a negative logarithmic dependence. The solid green line in Figure 6.8 is a fit to Equation 6.9. The constants ρ_{c1} and ρ_{c12} were found to be virtually the same indicating that the Fermi liquid description is valid.

Figure 6.4 shows the MR of RGO, which was found to be negative at low temperatures. As the temperature increases the MR approaches zero, appearing to be slightly positive at 31 K. Kondo scattering is expected to result in negative MR as the application of a magnetic field increases the Zeeman energy with the result that the number of available states for conduction electrons to scatter into decreases, consequently the resistance decreases. At

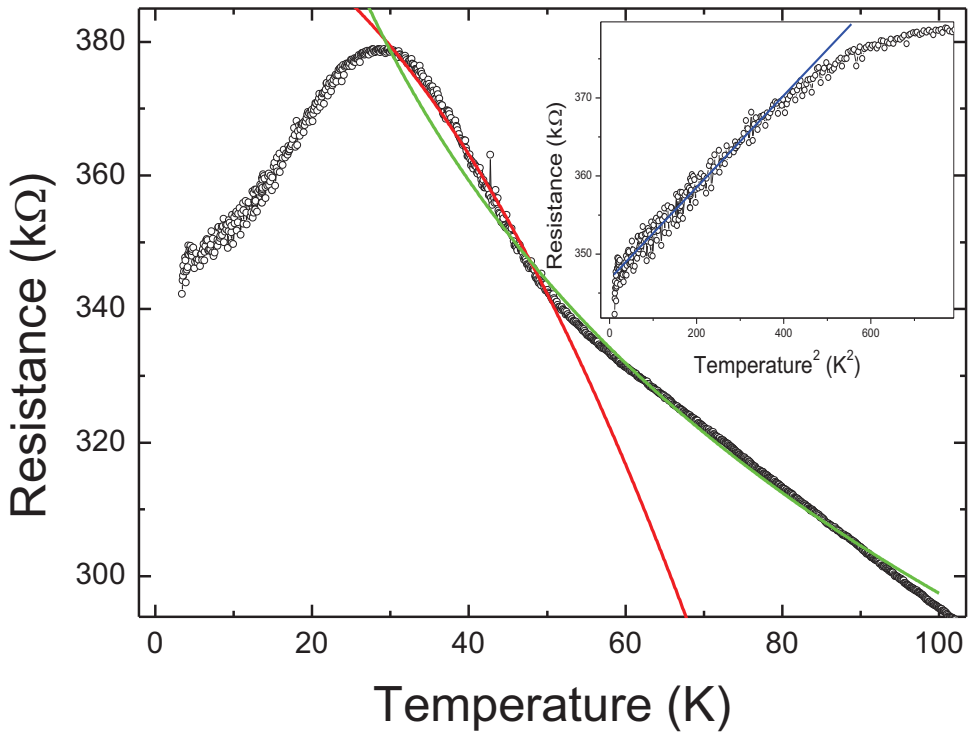


Figure 6.3: Resistance versus temperature of RGO. The solid red line is a fit to a quadratic temperature dependence while the green solid line is a fit to a logarithmic temperature dependence. Inset is the low temperature resistance plotted as a function of the temperature squared.

higher temperatures this effect is expected to decrease as phonon interactions disrupt the Kondo resonance. The MR is therefore scaled by a characteristic temperature (T^*) closely related to the Kondo temperature [182]. The MR has been plotted as a function of the scaled magnetic field within the Schlottmann description [182]

$$\frac{\rho(B) - \rho(0)}{\rho(0)} = f\left[\frac{B}{T + T^*}\right] \tag{6.10}$$

T^* was found to be in the region of 4 K. This is in good agreement with the Kondo temperature of 2.6 K determined from the R $vs.$ T measurements. We found that changing T^* by around 1 K destroyed the scaling. We attempted to interpret the MR measurements within the framework of 2D weak localization but found that the curve fits were not convincing. Furthermore the R $vs.$ T measurements at zero field show no sign of weak localization

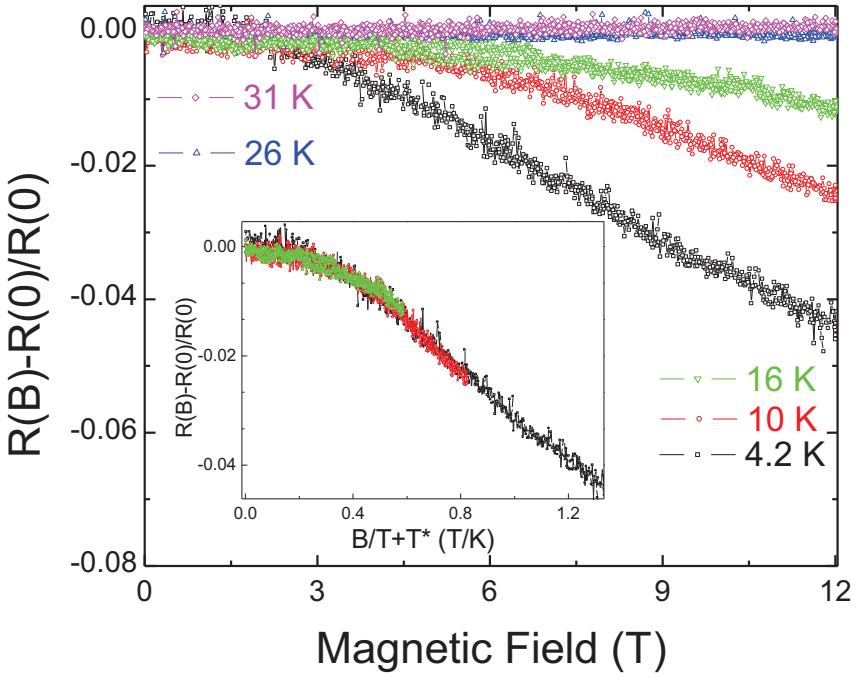


Figure 6.4: Magneto-resistance of RGO. Inset is the MR scaled with the characteristic temperature.

at low temperatures.

Hall measurements were performed to determine the carrier density at low temperatures. The experimental values of the mobile carrier density range from $6.041 \times 10^9\ cm^{-2}$ at 2.6 K to a maximum of $1.524 \times 10^{10}\ cm^{-2}$ at 18 K before levelling out at approximately $9 \times 10^{10}\ cm^{-2}$ at around 22 K. We have included the carrier density as a function of temperature in Figure 6.6. These values are consistent with mobile carrier densities reported in the literature for disordered graphene (for example [183]). The exact relationship between the fluctuations in carrier density and both the R *vs.* T and the MR data is difficult to firmly establish. Further experiments with varying oxygen concentrations could be illuminating in this regard. The experimentally determined defect density (using the same method as [180]) is $1.053 \times 10^{11}\mathrm{cm}^{-2}$, consistent with the value of $3 \times 10^{11}\ cm^{-2}$ determined in that study for irradiated graphene. The mobility of our RGO sample was found to be $3.09 \times 10^3\ cm^2/V.s$ at 2.6 K. We have also shown the Hall coefficient as a function of temperature in Figure 6.5.

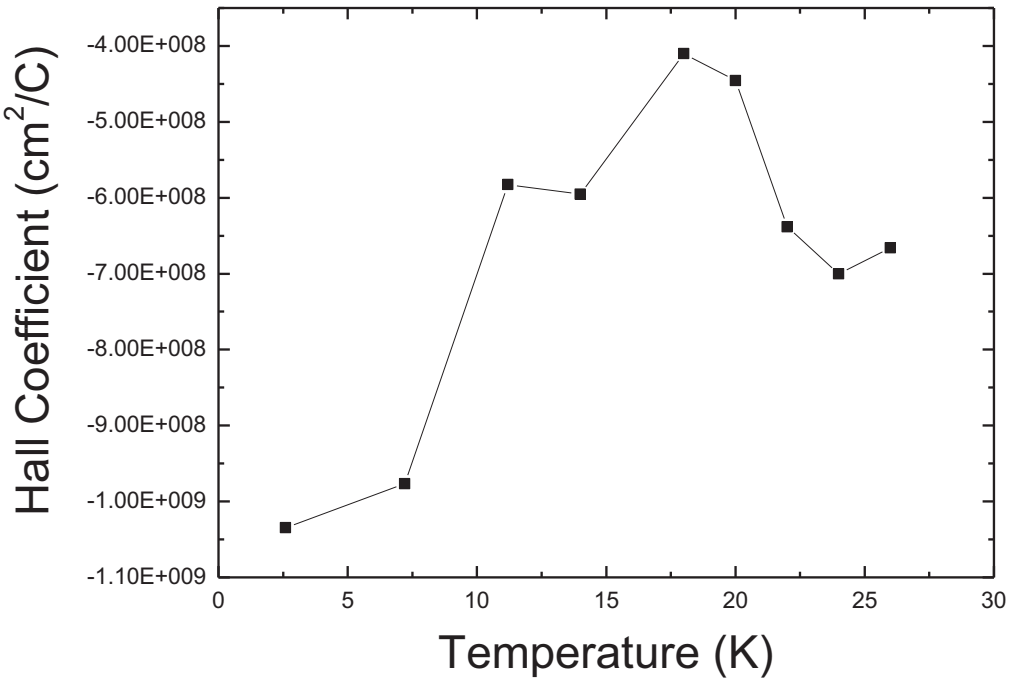


Figure 6.5: Hall Coefficient as a function of temperature

The stability for magnetic moments may be provided by the large π conjugation of certain free radical groups. If the hybridization between these localized moments and conduction electrons is not too small then the local moments and conduction electrons may be treated within the Anderson single impurity model. Topographical defects in the graphene lattice assist in the formation of stable magnetic moments induced by vacancies where the magnetism arises within the same π conjugated network as the conduction electrons (a schematic diagram is presented in Fig. 6.7). The presence of disorder is therefore crucial to the formation of local moments. However if the disorder is too great delocalized transport cannot occur. Delocalized conduction electrons in RGO may interact with both the local moments in functionalized regions and in non-functionalized regions (vacancies). It is difficult to imagine the Kondo effect arising in functionalized regions as charge carriers would not be expected to exist in extended states in these regions as a result of localization and potential barriers formed by sp^3 hybridization.

However in non-functionalized regions (intact graphene nano-islands) extended states may

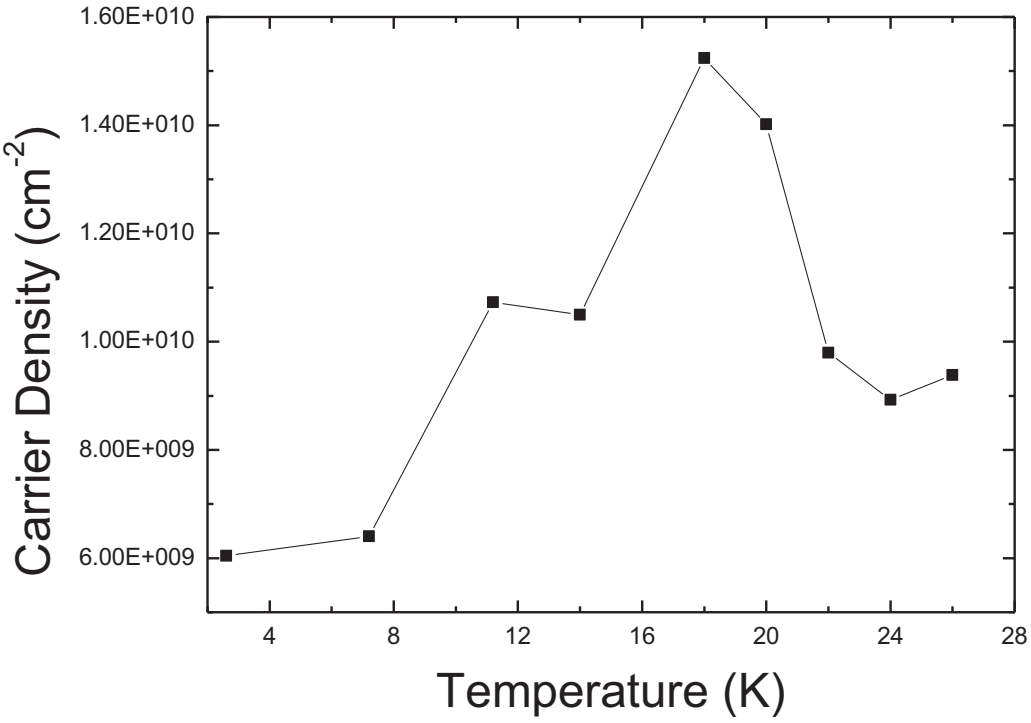


Figure 6.6: Carrier density as a function of temperature

well be found, despite the disorder induced in the reduction process. The antiferromagnetic interaction then between these extended states and local moments on functionalized regions (or at the edges of functionalized regions) and vacancies may then allow for the effective screening of local moments by conduction electrons at low temperatures. The effects of this screening (i.e. the Kondo effect) are seen at higher temperatures than they would otherwise be seen in pristine graphene because delocalized states only occur in the RGO samples when electrons gain enough energy to overcome the potential barriers posed by free radicals and disorder. This results in enhanced electron scattering from the "Kondo cloud" and resistance therefore shows a negative quadratic dependence. At yet higher temperatures phonon interactions interfere with the formation of the Kondo resonance, the interaction between local moments and conduction electrons becomes less prominent and spin-flip scattering may occur, indicated by a negative logarithmic dependence.

At very low temperatures, below 30 K, Fermi liquid behaviour (quadratic temperature dependence of the resistivity) ensues as a result of the onset of coherence effects which are

manifest in increased elastic scattering. This explanation is in agreement with calculations on graphene doped with charged impurities, where charge screening occurs due to interactions between the impurities and conduction electrons, which have shown a metal-insulator transition similar to the present experimental results [184].

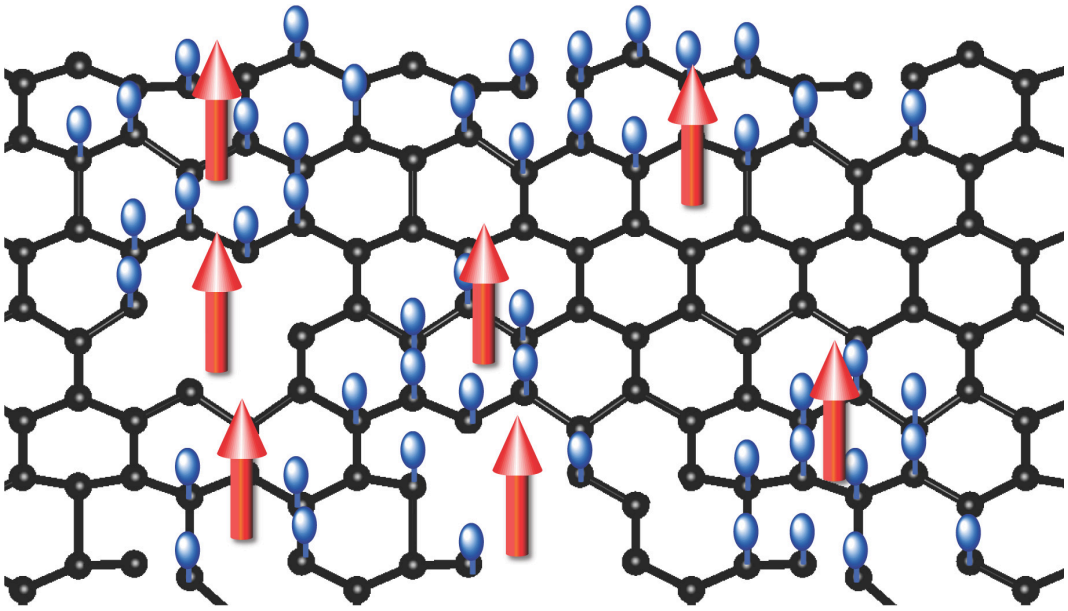


Figure 6.7: Schematic diagram of local moment formation in RGO. Local moments (red arrows) form at residual free radicals (blue spheres) which are attached to the basal graphene plane and vacancies in the lattice. Extended states may form in unfunctionalized graphene regions.

6.4 Conclusion

In summary, we have shown that the interaction between localized magnetic moments and conduction electrons may be of significance in the transport properties of graphene oxide reduced with ascorbic acid. The Fermi liquid description of the Kondo effect has been employed to fit R *vs.* T measurements while MR measurements scale with a characteristic temperature. The Kondo temperature is determined from the R *vs.* T measurements is 2.6 K which is in fair agreement with the characteristic temperature of 4 K determined from the scaling of the MR. This work provides motivation for further studies in RGO for possible spintronic applications. Further studies including gate voltage dependent measurements, which might

allow the occupancy of the local moments to be varied, may reveal more about the nature of the Kondo effect in RGO. Scanning transmission spectroscopy may also yield insight into the Kondo resonance in RGO. In further studies devices could be designed specifically to study the Kondo effect in graphene. With the manipulation of single atoms afforded by scanning transmission microscopes, it may be possible to place individual ferromagnetic adatoms at specific lattice sites (most likely informed by DFT calculations) to induce the Kondo effect. Chemical methods could also be used to deposit ferromagnetic clusters in functionalized graphenes.

Chapter 7

Conclusions

Graphene and chemically modified graphenes have generated great interest in very different facets of science, from molecular cell biology to renewable energy. It is a unifying force in physics, sparking debate across the board. The full potential of modified graphenes will likely not only be realized in the succession of conventional devices but in the development of innovative devices which exploit their unique properties. It has been widely reported that the European Union, in conjunction with universities worldwide and commercial partners (a notable example being Nokia) will invest around 100 million Euro over the next 10 years in taking graphene from a novel research material to the marketplace. However, as the fanfare surrounding pristine graphene begins to wane, focus has turned towards modified graphenes which offer even greater potential. The full potential of graphene lies in graphene-hybrid materials which exploit its fundamental properties with tolerance to the defects and disorder inherent to real systems. With the foundation laid in studies of pristine graphene focus has shifted to modified graphenes.

Future nano-electronic devices will require a wide range of properties and therefore different dopants and doping mechanisms are required to modify the electronic properties. Progress in graphene devices has been rapid especially given the difficulties of working with a material which is only a single atom thick. New processing techniques are actively being pursued to bring graphene and chemically modified graphene devices to the market and with the exponential advance of technology, chemically modified graphenes will undoubtedly contribute to carbon-based devices.

Graphene nano-electronic devices are widely anticipated to surpass current technologies.

In Chapter 2 the electronic properties of N incorporated graphene and bilayer graphene were studied. N incorporation induces metallicity in bilayer graphene while a gap is opened up in the vicinity of the K point. N modification greatly reduces the dependence of the band structure on the stacking configuration. We find that N incorporation is unlikely to induce magnetism in bilayer graphene. A comparison of the total energy of graphene nano-ribbons with N incorporated on the edge and in the bulk of the nano-ribbon indicated that N atoms will tend to diffuse to the edge of the nano-ribbon to decrease the energy of the system. This will likely pose a limitation to the maximum possible atomic doping of N as when nitrogen atoms meet at the edges they are likely to recombine to N_2 and dissociate from the graphene lattice.

In addition to the intrinsic bandgap of graphene nano-ribbons, previous studies have investigated chemical modification of graphene in order to induce a bandgap. On the other hand, carbon nano-tubes and graphene nano-ribbons have been proposed as potential interconnects in nano-electronic integrated circuits. However graphene nano-ribbons have a band gap which scales inversely with the width of the graphene nano-ribbon. Considering the findings of the present study, N incorporation could be employed to reintroduce metallicity to bilayer graphene nano-ribbons. However the diffusion of nitrogen atoms to the edge of graphene nano-ribbons must also be accounted for in future studies. This may well be beneficial as additional edge effects could enhance device applications. The current work may be extended to studies of the transport properties of disordered N incorporated graphene.

In addition to substitutional incorporation, N can form many complexes which can be incorporated into graphene. This allows N complexes to be incorporated with a range of different potentials allowing the band modulation to be tuned provided the gas phase chemistry can be controlled. This is beneficial for large-scale production as various modifications to the electronic properties can be achieved with little change in the processing methods. Device parameters such as resonant energies and carrier lifetimes could then be tuned based on the predominant incorporation of one or another N complex. Further studies may focus on the influence of different N complexes on electronic properties as well as formation energies to inform synthesis techniques.

While N incorporated bilayer graphene is metallic in the in-plane direction, calculations of the dielectric function are required to determine the nature of N doped graphene in the out-of-plane direction. This may be of significance towards the development of meta-materials however is not likely to be of significance for electronic device applications.

After studying the modifications to the electronic properties of graphene and bilayer graphene induced through the incorporation of single N impurities, the electronic transport properties of impurity clusters embedded within a high bandgap material were studied in Chapter 3. It was demonstrated that the device parameters such as the resonant energy and characteristic time can be controlled through the geometric arrangement of impurity clusters based on quantum interference. A distinct Fano resonance forms and the calculated $I-V$ characteristics show negative differential conductance. This study may be extended to the effects of impurity clusters embedded in a carbon matrix on the resonant tunneling features. Regions of predominantly sp^3 hybridized carbon form high potentials while sp^2 hybridized clusters form lower potentials. In reality a competition between two processes i.e. increase of cluster size and separation of clusters can result in conductivity saturation in the regime of large coupling between the impurity clusters [124].

In Chapter 5 we showed that the geometry of the impurity configuration can be tuned to achieve maximum electron transmission. Hence the energy of maximum transmission and also the lifetime of wavefunctions in the respective trapping centres can be tuned. Considering the significant interest in naturally grown systems, for example reduced graphene oxide, this study provides an in depth theoretical investigation of the effect of cluster configuration on the transport properties of disordered graphenes [185, 186]. This study will enable us to interpret the efficiency of doping versus non-doping in unconventional semiconductors such as in diamond-like carbon films, which may find use in the development of new kinds of field effect transistors based on the controlled arrangement of clusters. In addition, the controlled confinement of charge carriers may lead to quantum information devices. We intend to extend this model to include spin to inform the development of spintronic devices.

The experimental methods were presented in Chapter 4. In the present study, dielectrophoresis was used to control the placement of nano-materials by applying an alternating current to micro-electrodes. Low temperature transport measurements were performed in both the two probe and four probe configurations. In future studies nano-scale devices will be manufactured using an in-situ gas injection system and electron beam lithography. Temperature dependent four probe measurements will be performed from low temperatures (80 K) using nano-manipulated probes within a scanning electron microscope providing access to quantum transport properties on the nano-scale. Using nano-manipulators and gas injection, devices can also be manufactured for low temperature, magneto-resistance and gate voltage dependent measurements within the Janis micromanipulated probe station and the

Cryogenic free measurement system. Specifically, high frequency transport measurements will be studied at low temperature and under an applied magnetic field.

In Chapter 5 the transport and magnetic properties of RGO were studied. Through reduction of GO with ascorbic acid, the electrical properties have shown improvement in comparison to GO reduced using hydrazine. This may be of use in large-scale production of graphene devices such as FET's. The transport properties are unusual and show a combination of effects associated with pristine graphene and disordered metals. We suggest a transport model in which MRF's are prominent at low temperatures while at higher temperatures the thermally activated carriers are strongly influenced by elastic scattering. This anomalous scattering, interpreted within an extended Ziman theory of transport, merits further investigation towards a more complete theory of transport in RGO. The magnitude and distribution of the graphene quantum dots within RGO can be tuned to some extent during the chemical reduction. Future studies might determine the relationship between the transport properties and the extent of the graphene nano-islands. Gate voltage dependent measurements may aid in the interpretation of MRF's however the interaction of the substrate may influence the gate voltage dependence.

At low temperatures, RGO shows ferromagnetism undergoing a phase transition to diamagnetism at around 8 K. While ferromagnetism in carbon is an emerging field, it is widely accepted that local magnetic moments form at defects, vacancies and topographical distortions with the large π conjugation of free radicals providing the stability for local moments. Tuning the extent of graphene nano-islands may also shed some light on the nature of ferromagnetic ordering in RGO. Furthermore annealing to reverse some of the damage introduced in the reduction process may also shed light on the role of topographical distortions as opposed to residual free radicals.

With initial studies indicating delocalized states and magnetic moments at low temperatures, more detailed transport studies were performed. In Chapter 6 four probe transport measurements were performed on RGO. We found that the interaction of itinerant conduction electrons and local magnetic moments can be significant in reduced graphene oxide. R $vs.$ T measurements showed a metal-insulator transition which was interpreted within the Fermi liquid description of the Kondo effect. In addition the scaling of magnetoresistance measurements was interpreted within the Schlotmann description of magnetoresistance of the Kondo effect. Hall measurements of RGO samples indicated a high mobility, comparable to that of disordered graphenes. The carrier density was also found to be in agreement with

that found in a previous study which confirmed the Kondo effect in graphene. The field of correlated graphene systems is gaining momentum not only due to the rich physics of these systems but also towards device applications in graphene spintronics. There is great scope for further studies especially with regard to Kondo physics in functionalized graphenes.

In our study of quantum transport through quantum dot systems, we find a Fano resonance close to E_F. With the inclusion of spin in the model it may be possible to induce correlations based not only on constructive interference but also on the interaction of the spin of charge carriers with local moments. This model would not necessarily capture conventional Kondo physics but might aid in addressing the inter-play between quantum interference phenomena and spin dependent correlations. Motivated by the experimental observation of the Kondo effect in RGO, we may study functionalized graphene with clusters of ferromagnetic impurities to develop new spintronic devices. With the inclusion of localized magnetic moments it may be possible to employ a magnetic field to further control the carrier lifetime. Additionally the spin Rashba effect in quantum dot systems would be of interest. In future studies, phonon interactions may also be included.

We have considered some potential outputs of the combined studies of this work. One potential application may lie in dosimetry. Amorphous carbon is currently also being used for medical imaging applications in conjunction with CsI scintillators. With a wide operational range and high frequency capabilities, researchers in medical physics and materials science are working towards further improving amorphous carbon and polycrystalline diamond devices through controlling the device properties, principally through chemical doping in the gas phase reaction [187]. Radiation induces electrons which can be induce conductivity in diamond. One of the primary motivations for the use of diamond is that it has a dosimetry index close to that of human flesh. Another important factor is the robustness of diamond and its resilience to external influences.

By tuning the graphitic concentration in $a-C$ films the dosimetry factor could be further controlled. Graphitic impurity clusters within $a-C$ are effectively quantum dots. Through the controlled arrangement of these dots it may be possible to develop new electronic detectors for a wide range of applications, such as dosimetry and bolometry. As the eigenenergies are well defined, the influence of external radiation could be detected by the change in resonant energy. This may offer greater scope for performing dosimetry in different regions of the spectrum by tuning the eigenenergies of wells in the $a-C$ SL structures through controlling the geometric configuration of the clusters while the eigenenergies of the clusters

can be tuned through the application of a gate voltage.

Bibliography

[1] A. K. Geim and K. S. Novoselov, Nature Mater. **6**, 183 (2007).

[2] A. K. Geim, Science **324**, 1530 (2009).

[3] K. S. Novoselov *et al.*, Science **306**, 666 (2004).

[4] K. S. Novoselov *et al.*, Nature Phys. **2**, 177 (2006).

[5] S. Das Sarma, S. Adam, E. H. Hwang, and E. Rossi, Rev. Mod. Phys. **83**, 407 (2011).

[6] A. H. Castro Neto, F. Guinea, N. M. R. Peres, K. S. Novoselov, and A. K. Geim, Rev. Mod. Phys. **81**, 109 (2009).

[7] G. W. Semenoff, Phys. Rev. Lett. **53**, 2449 (1984).

[8] Y. Wu *et al.*, Nature **472**, 74 (2011).

[9] K. S. Novoselov *et al.*, Nature **438**, 197 (2005).

[10] Y. Zhang, Y.-W. Tan, H. L. Stormer, and P. Kim, Nature **438**, 201 (2005).

[11] V. P. Gusynin and S. G. Sharapov, Phys. Rev. Lett. **95**, 146801 (2005).

[12] K. S. Novoselov *et al.*, Science **315**, 1379 (2007).

[13] R. S. Deacon, K.-C. Chuang, R. J. Nicholas, K. S. Novoselov, and A. K. Geim, Phys. Rev. B **76**, 081406 (2007).

[14] Z. Jiang *et al.*, Phys. Rev. Lett. **98**, 197403 (2007).

[15] C. W. J. Beenakker, Rev. Mod. Phys. **80**, 1337 (2008).

[16] E. Y. Andrei, G. Li, and X. Du, Rep. Prog. Phys. **75**, 056501 (2012).

[17] M. Katsnelson and K. Novoselov, Solid State Commun. **143**, 3 (2007).

[18] K. I. Bolotin, K. J. Sikes, J. Hone, H. L. Stormer, and P. Kim, Phys. Rev. Lett. **101**, 096802 (2008).

[19] C. Bai and X. Zhang, Phys. Rev. B **76**, 075430 (2007).

[20] M. I. Katsnelson, K. S. Novoselov, and A. K. Geim, Nature Phys. **2**, 620 (2006).

[21] E. V. Castro *et al.*, Phys. Rev. Lett. **99**, 216802 (2007).

[22] H. Min, B. Sahu, S. K. Banerjee, and A. H. MacDonald, Phys. Rev. B **75**, 155115 (2007).

[23] Y.-M. Lin and P. Avouris, Nano Lett. **8**, 2119 (2008).

[24] J. Nilsson, A. H. Castro Neto, F. Guinea, and N. M. R. Peres, Phys. Rev. B **78**, 045405 (2008).

[25] E. McCann and V. I. Fal'ko, Phys. Rev. Lett. **96**, 086805 (2006).

[26] T. Ohta, A. Bostwick, T. Seyller, K. Horn, and E. Rotenberg, Science **313**, 951 (2006).

[27] S. Y. Zhou *et al.*, Nature Phys. **2**, 595 (2006).

[28] A. Bostwick, T. Ohta, T. Seyller, K. Horn, and E. Rotenberg, Nature Phys. **3**, 36 (2007).

[29] S. V. Morozov *et al.*, Phys. Rev. Lett. **97**, 016801 (2006).

[30] V. Skákalová, A. B. Kaiser, J. S. Yoo, D. Obergfell, and S. Roth, Phys. Rev. B **80**, 153404 (2009).

[31] K. K. Mahelona, A. B. Kaiser, and V. Skákalová, Phys. Status Solidi (b) **247**, 2983 (2010).

[32] G. Bohra *et al.*, App. Phys. Lett. **101**, 093110 (2012).

[33] A. Rycerz, J. Tworzydo, and C. W. J. Beenakker, Europhys. Lett. **79**, 57003 (2007).

[34] S. V. Morozov *et al.*, Phys. Rev. Lett. **100**, 016602 (2008).

[35] A. N. Pal, V. Kochat, and A. Ghosh, Phys. Rev. Lett. **109**, 196601 (2012).

[36] D. Horsell *et al.*, Solid State Commun. **149**, 1041 (2009).

[37] M. Y. Kharitonov and K. B. Efetov, Phys. Rev. B **78**, 033404 (2008).

[38] E. R. Mucciolo and C. H. Lewenkopf, J. Phys.: Condens. Matter **22**, 273201 (2010).

[39] B. Trauzettel, D. Bulaev, D. Loss, and G. Bukard, Nature Phys. **3**, 192 (2007).

[40] V. N. Kotov, B. Uchoa, V. M. Pereira, F. Guinea, and A. H. Castro Neto, Rev. Mod. Phys. **84**, 1067 (2012).

[41] S. Das Sarma, E. H. Hwang, and W.-K. Tse, Phys. Rev. B **75**, 121406 (2007).

[42] T. Schiros *et al.*, Nano Lett. **12**, 4025 (2012).

[43] D. Usachov *et al.*, Nano Lett. **11**, 5401 (2011).

[44] Y. Fujimoto and S. Saito, Phys. Rev. B **84**, 245446 (2011).

[45] H. Wang, T. Maiyalagan, and X. Wang, ACS Catalysis **2**, 781 (2012).

[46] S.-O. Guillaume, B. Zheng, J.-C. Charlier, and L. Henrard, Phys. Rev. B **85**, 035444 (2012).

[47] D. Wei *et al.*, Nano Lett. **9**, 1752 (2009).

[48] S. Souto, M. Pickholz, M. C. dos Santos, and F. Alvarez, Phys. Rev. B **57**, 2536 (1998).

[49] O. Williams *et al.*, Diam. Relat. Mater. **17**, 1080 (2008).

[50] S. Bhattacharyya *et al.*, Appl. Phys. Lett. **79**, 1441 (2001).

[51] G. Chimowa, D. Churochkin, and S. Bhattacharyya, Europhys. Lett. **99**, 49902 (2012).

[52] A. Quandt, C. Özdogan, J. Kunstmann, and H. Fehske, Nanotechnology **19**, 335707 (2008).

[53] C. O. Girit *et al.*, Science **323**, 1705 (2009).

[54] Y. An and Z. Yang, Appl. Phys. Lett. **99**, 192102 (2011).

[55] P. Hewageegana and V. Apalkov, Phys. Rev. B **79**, 115418 (2009).

[56] E. Vernek, P. A. Orellana, and S. E. Ulloa, Phys. Rev. B **82**, 165304 (2010).

[57] T. V. Shahbazyan and M. E. Raikh, Phys. Rev. B **49**, 17123 (1994).

[58] M. L. Ladrón de Guevara and P. A. Orellana, Phys. Rev. B **73**, 205303 (2006).

[59] S. Kawaguchi, Journal of the Physical Society of Japan **76**, 104704 (2007).

[60] Y. S. Joe, E. R. Hedin, and A. M. Satanin, Phys. Rev. B **76**, 085419 (2007).

[61] T. Kubo, Y. Tokura, T. Hatano, and S. Tarucha, Phys. Rev. B **74**, 205310 (2006).

[62] F. Delgado, Y.-P. Shim, M. Korkusinski, and P. Hawrylak, Phys. Rev. B **76**, 115332 (2007).

[63] C. Gómez-Navarro *et al.*, Nano Lett. **10**, 1144 (2010).

[64] S. Wang *et al.*, Adv. Mater. **20**, 3440 (2008).

[65] D. Joung and S. I. Khondaker, Phys. Rev. B **86**, 235423 (2012).

[66] D. Joung, L. Zhai, and S. I. Khondaker, Phys. Rev. B **83**, 115323 (2011).

[67] G. Eda, C. Mattevi, H. Yamaguchi, H. Kim, and M. Chhowalla, J. Phys. Chem. C **113**, 15768 (2009).

[68] Y. Wang *et al.*, Nano Lett. **9**, 220 (2009).

[69] M. J. Fernandez-Merino *et al.*, J. Phys. Chem. C **114**, 6426 (2010).

[70] H. S. S. R. Matte, K. S. Subrahmanyam, and C. N. R. Rao, J. Phys. Chem. C **113**, 9982 (2009).

[71] N. Tombros, C. Jozsa, M. Popinciuc, H. Jonkman, and B. van Wees, Nature **448**, 571 (2007).

[72] D. Pesin and A. H. MacDonald, Nature Mater. **11**, 409 (2007).

[73] W. Han and R. K. Kawakami, Phys. Rev. Lett. **107**, 047207 (2011).

[74] L. Li *et al.*, ACS Nano **5**, 2601 (2011).

[75] J. Kohanoff, *Electronic Structure Calculations For Solids and Molecules*, Cambridge, 2006.

[76] D. S. Sholl and J. A. Steckel, *Density Functional Theory: A Practical Introduction*, John Wiley and Sons Inc., Connecticut, USA, 2009.

[77] R. M. Martin, *Electronic Structure: Basic Theory and Practical Methods*, Cambridge, 2010.

[78] R. G. Parr and W. Yang, *Density-Functional Theory of Atoms and Molecules*, Oxford Scientific Publications, 1994.

[79] P. Hohenberg and W. Kohn, Physical Review **136**, 864 (1964).

[80] K. Capelle, arXiv preprint condmat/0211443 .

[81] M. Levy, Proc. Natl. Acad. Sci. USA **76**, 6062 (1979).

[82] W. Kohn and L. J. Sham, Phys. Rev. **140**, A1133 (1965).

[83] M. Payne, M. Teter, M. Ailan, T. Arias, and J. Joannopouios, Rev. Mod. Phys. **64**, 1045 (1992).

[84] J. P. Perdew, K. Burke, and M. Ernzerhof, Phys. Rev. Lett. **77**, 3865 (1996).

[85] G. Kresse and D. Joubert, Phys. Rev. B **59**, 1758 (1999).

[86] P. E. Blöchl, Phys. Rev. B **50**, 17953 (1994).

[87] G. Kresse and J. Furthmüller, Phys. Rev. B **54**, 11169 (1996).

[88] G. Kresse and J. Furthmller, Comput. Mater. Sci. **6**, 15 (1996).

[89] G. Fanchini and A. Tagliaferro, Appl. Phys. Lett. **85**, 730 (2004).

[90] D. McCulloch and A. Merchant, Thin Solid Films **290**, 99 (1996).

[91] A. Cresti *et al.*, Nano Research **1**, 361 (2008).

[92] V. M. Pereira, F. Guinea, J. M. B. Lopes dos Santos, N. M. R. Peres, and A. H. Castro-Neto, Phys. Rev. Lett. **96**, 036801 (2006).

[93] L. Pisani, B. Montanari, and N. M. Harrison, New J. Phys. **10**, 033002 (2008).

[94] F. Joucken *et al.*, Phys. Rev. B **85**, 161408 (2012).

[95] S. Latil and L. Henrard, Phys. Rev. Lett. **97**, 036803 (2006).

[96] M. G. Menezes, R. B. Capaz, and J. L. B. Faria, Phys. Rev. B **82**, 245414 (2010).

[97] V. Timoshevskii, W. Ji, H. Abou-Rachid, L.-S. Lussier, and H. Guo, Phys. Rev. B **80**, 115409 (2009).

[98] X. Zhong, R. Pandey, and S. P. Karna, Carbon **50**, 784 (2012).

[99] M. Barbier, *Transport properties of nanostructures and superlattices on single-layer and bilayer graphene*, PhD thesis, Universiteit Antwerpen, 2012.

[100] C. W. Chiu, S. H. Lee, S. C. Chen, F. L. Shyu, and M. F. Lin, New J. Phys. **12**, 083060 (2010).

[101] A. L. Rakhmanov, A. V. Rozhkov, A. O. Sboychakov, and F. Nori, Phys. Rev. Lett. **109**, 206801 (2012).

[102] J. H. Ho, C. L. Lu, C. C. Hwang, C. P. Chang, and M. F. Lin, Phys. Rev. B **74**, 085406 (2006).

[103] M. Mucha-Kruczyński, E. McCann, and V. I. Fal'ko, Semicond. Sci. Technol. **25**, 033001 (2010).

[104] E. McCann, D. S. Abergel, and V. I. Fal'ko, The European Physical Journal Special Topics **148**, 91 (2007).

[105] E. McCann and M. Koshino, arXiv:1205.6953 (2012).

[106] D. Boukhvalov, M. Katsnelson, and A. Lichtenstein, Phys. Rev. B **77**, 035427 (2008).

[107] C. J. Tabert and E. J. Nicol, Phys. Rev. B **86**, 075439 (2012).

[108] K. Lee, E. D. Murray, L. Kong, B. I. Lundqvist, and D. C. Langreth, Phys. Rev. B **82**, 081101 (2010).

[109] M. Hasegawa, K. Nishidate, and H. Iyetomi, Phys. Rev. B **76**, 115424 (2007).

[110] X. Wu, M. C. Vargas, S. Nayak, V. Lotrich, and G. Scoles, J. Chem. Phys. **115**, 8748 (2001).

[111] M. P. Lima, A. Fazzio, and A. J. R. da Silva, Phys. Rev. B **79**, 153401 (2009).

[112] H. Santos, A. Ayuela, L. Chico, and E. Artacho, Phys. Rev. B **85**, 245430 (2012).

[113] K. Lee, E. D. Murray, L. Kong, B. I. Lundqvist, and D. C. Langreth, Phys. Rev. B **82**, 081101 (2010).

[114] P. L. de Andres, R. Ramírez, and J. A. Vergés, Phys. Rev. B **77**, 045403 (2008).

[115] S. Jalili and R. Vaziri, Mole. Phys. **109**, 687 (2011).

[116] B. Guo *et al.*, Nano Lett. **10**, 4975 (2010).

[117] P. R. C. Kent and A. Zunger, Appl. Phys. Lett. **79**, 2339 (2001).

[118] I. A. Buyanova, M. Izadifard, W. M. Chen, H. P. Xin, and C. W. Tu, Phys. Rev. B **69**, 201303 (2004).

[119] S. Bhattacharyya, M. Lubbe, P. R. Bressler, D. R. T. Zahn, and F. Richter, Diam. Relat. Mater. **11**, 8 (2002).

[120] R. Gago *et al.*, Phys. Rev. B **72**, 014120 (2005).

[121] A. A. Valladares and F. Álvarez-Ramírez, Phys. Rev. B **73**, 024206 (2006).

[122] C. H. Lee *et al.*, Phys. Rev. B **49**, 11448 (1994).

[123] S. Bhattacharyya and S. R. P. Silva, Appl. Phys. Lett. **90**, 082105 (2007).

[124] S. Bhattacharyya and S. R. P. Silva, Thin Solid Films **482**, 94 (2005).

[125] M. V. Katkov and S. Bhattacharyya, J. Appl. Phys. **111**, 123711 (2012).

[126] F. Mohammed and S. Bhattacharyya, Europhys. Lett. **100**, 26009 (2012).

[127] K. A. Matveev and A. I. Larkin, Phys. Rev. B **46**, 15337 (1992).

[128] L. I. Glazman and K. A. Matveev, Zh. Eksp. Teor. Fiz. **94**, 332 (1988).

[129] A. K. Savchenko *et al.*, Phys. Rev. B **52**, R17021 (1995).

[130] V. V. Kuznetsov, A. K. Savchenko, D. R. Mace, E. H. Linfield, and D. A. Ritchie, Phys. Rev. B **56**, R15533 (1997).

[131] P. Trocha and J. Barnaś, Phys. Rev. B **78**, 075424 (2008).

[132] Z.-T. Jiang, Q.-F. Sun, and Y. Wang, Phys. Rev. B **72**, 045332 (2005).

[133] R. H. Dicke, Phys. Rev. **93**, 99 (1954).

[134] H. Lee, H. Hsu, and L. E. Reichl, Phys. Rev. B **71**, 045307 (2005).

[135] Y. Xu, A. Matsuda, and M. R. Beasley, Phys. Rev. B **42**, 1492 (1990).

[136] A. Rakitin, M. Y. Valakh, N. I. Klyui, V. G. Visotski, and A. P. Litvinchuk, Phys. Rev. B **58**, 3526 (1998).

[137] D. C. Marcano *et al.*, ACS Nano **4**, 4806 (2010).

[138] P. A. Lee, A. D. Stone, and H. Fukuyama, Phys. Rev. B **35**, 1039 (1987).

[139] D. Horsell *et al.*, arXiv:0902.0904 (2009).

[140] S. Branchaud, A. Kam, P. Zawadzki, F. M. Peeters, and A. S. Sachrajda, Phys. Rev. B **81**, 121406 (2010).

[141] M. Katsnelson and A. Geim, Phil. Trans. R. Soc. A **366**, 195 (2008).

[142] S. Adam and S. Das Sarma, Phys. Rev. B **77**, 115436 (2008).

[143] U. Mizutani and K. Yoshino, Journal of Physics F: Metal Physics **14**, 1179 (1984).

[144] T. Matsuda and U. Mizutani, Journal of Physics F: Metal Physics **12**, 1877 (1982).

[145] P. J. Cote and L. V. Meisel, Phys. Rev. Lett. **40**, 1586 (1978).

[146] K. Frobose and J. Jackle, Journal of Physics F: Metal Physics **7**, 2331 (1977).

[147] T. Matsuda, N. Shiotani, and U. Mizutani, Journal of Physics F: Metal Physics **14**, 1193 (1984).

[148] T. Matsuda and U. Mizutani, Solid State Commun. **44**, 145 (1982).

[149] M. J. Allen, V. C. Tung, and R. B. Kaner, Chemical Reviews **110**, 132 (2010).

[150] D. R. Dreyer, S. Park, C. W. Bielawski, and R. S. Ruoff, Chem. Soc. Rev. **39**, 228 (2010).

[151] N. Liu *et al.*, Adv. Funct. Mater. **18**, 1518 (2008).

[152] S. Park and R. S. Ruoff, Nat. Nanotechnol. **4**, 217 (2009).

[153] K. P. Loh, Q. Bao, P. K. Ang, and J. Yang, J. Mater. Chem. **20**, 2277 (2010).

[154] D. A. Abanin, A. V. Shytov, and L. S. Levitov, Phys. Rev. Lett. **105**, 086802 (2010).

[155] D. Joung, A. Chunder, L. Zhai, and S. I. Khondaker, Appl. Phys. Lett. **97**, 093105 (2010).

[156] A. B. Kaiser, C. Gómez-Navarro, R. S. Sundaram, M. Burghard, and K. Kern, Nano Lett. **9**, 1787 (2009).

[157] C. Gómez-Navarro *et al.*, Nano Lett. **7**, 3499 (2007).

[158] J. Zhou *et al.*, Nano Lett. **9**, 3867 (2009).

[159] J. Cervenka, M. Katsnelson, and C. Flipse, Nature Phys. **5**, 840 (2009).

[160] W. L. Wang, S. Meng, and E. Kaxiras, Nano Lett. **8**, 241 (2008).

[161] N. F. Mott and E. A. Davis, *Electronic Processes in Non-crystalline Materials*, Oxford University Press, 1979.

[162] K. Zou and J. Zhu, Phys. Rev. B **82**, 081407 (2010).

[163] C. N. R. Rao, H. S. S. R. Matte, K. S. Subrahmanyam, and U. Maitra, Chem. Sci. **3**, 45 (2012).

[164] A. C. Hewson, *The Kondo Problem to Heavy Fermions*, Cambridge University Press, 1997.

[165] P. Phillips, *Advanced Solid State Physics*, Westview Press, 2003.

[166] K. Yosida, *Theory of Magnetism*, Springer, 1996.

[167] A. Strydom, *Electronic and magnetic properties in f-electron magnetic, Kondo, heavy-fermion and non-Fermi liquid systems*, PhD thesis, University of the Witwatersrand, 1998.

[168] B. A. Jones, *Handbook of Magnetism and Advanced Magnetic Materials, Volume 1: Fundamentals and Theory*, John Wiley Sons, Ltd, 2007.

[169] R. M. P. Michael Grobis, Ileana G. Rau and D. Goldhaber-Gordon, *Handbook of Magnetism and Advanced Magnetic Materials, Volume 1: Fundamentals and Theory*, John Wiley Sons, Ltd, 2007.

[170] S.-P. Chao and V. Aji, Phys. Rev. B **83**, 165449 (2011).

[171] K. Sengupta and G. Baskaran, Phys. Rev. B **77**, 045417 (2008).

[172] P. Haase, S. Fuchs, T. Pruschke, H. Ochoa, and F. Guinea, Phys. Rev. B **83**, 241408 (2011).

[173] L. Fritz and M. Vojta, arXiv:1208.3113v1.

[174] O. V. Yazyev and M. I. Katsnelson, Phys. Rev. Lett. **100**, 047209 (2008).

[175] P. S. Cornaglia, G. Usaj, and C. A. Balseiro, Phys. Rev. Lett. **102**, 046801 (2009).

[176] K. M. McCreary, A. G. Swartz, W. Han, J. Fabian, and R. K. Kawakami, Phys. Rev. Lett. **109**, 186604 (2012).

[177] X. Hong, S.-H. Cheng, C. Herding, and J. Zhu, Phys. Rev. B **83**, 085410 (2011).

[178] X. Hong, K. Zou, B. Wang, S.-H. Cheng, and J. Zhu, Phys. Rev. Lett. **108**, 226602 (2012).

[179] S.-W. Wang *et al.*, Nanotechnology **22**, 335701 (2011).

[180] J. H. Chen, L. Li, W. G. Cullen, E. D. Williams, and M. S. Fuhrer, Nature Phys. **7**, 535 (2011).

[181] P. Nozières, Journal of Low Temperature Physics **17**, 31 (1974).

[182] T. A. Costi, Phys. Rev. Lett. **85**, 1504 (2000).

[183] X. Du, A. Barker, I. Skachko, and Y. Andrei, Eva, Nat. Nanotechnology **3**, 491 (2008).

[184] E. H. Hwang and S. Das Sarma, Phys. Rev. B **79**, 165404 (2009).

[185] R. McIntosh, M. A. Mamo, B. Jamieson, S. Roy, and S. Bhattacharyya, Europhys. Lett. **97**, 38001 (2012).

[186] R. McIntosh and S. Bhattacharyya, Phys. Status Solidi (RRL) Rapid Research Letters **6**, 56 (2012).

[187] M. A. Abdel-Rahman, A. Lohstroh, I. Jayawardena, and S. J. Henley, Diam. and Relat. Mater. **22**, 70 (2012).